The Dissertation Committee for Marc-Andre Schaeuble
certifies that this is the approved version of the following dissertation:

The Behavior of Hydrogen and Helium at White Dwarf Photosphere Conditions

Committee:

D. E. Winget, Supervisor

M. H. Montgomery, Co-Supervisor

Christopher Sneden

Edward L. Robinson

J. Craig Wheeler

J. E. Bailey

T. Nagayama

The Behavior of Hydrogen and Helium at White Dwarf Photosphere Conditions

by

Marc-Andre Schaeuble

DISSERTATION

Presented to the Faculty of the Graduate School of

The University of Texas at Austin

in Partial Fulfillment

of the Requirements

for the Degree of

DOCTOR OF PHILOSOPHY

THE UNIVERSITY OF TEXAS AT AUSTIN

December 2018

Dedicated to my parents, Jörg and Brigitta.

Acknowledgments

Everyone knows that it takes a village to do anything of significance in life. This dissertation is no different. Many people contributed to this thesis, and I will attempt to thank them here. If I have forgotten anyone, please forgive me.

First and foremost, I have to thank my parents, Jörg and Brigitta. Every graduate student goes through many highs and lows during their career and my parents were with me every step of the way. Their unending support is a large part of the reason why this thesis saw the light of day. Thank you. I also thank my brother, Jan-Eric, for his willingness to always listen to my complaints about everything and everyone. Our co-op gaming sessions during my visits to South Carolina will never be forgotten. Thank you.

This list of personal acknowledgements list would not be complete without a mention of Sarah Minor. Her contributions to my thesis are intangible but their worth is almost immeasurable. She showed me that life is beautiful and worth living. She provided me with something to look forward to after the PhD. For that, I will forever be indebted to her.

From an academic standpoint, it all began with the administrative staff at my high school, Zinzendorfschule Königsfeld. I thank you for helping me apply to Clemson University - twice. Jeremy King took me under his wing as

an undergraduate and taught me the basics of spectroscopy. The fact that I still perform spectroscopy today is a testament to his teaching and mentorship skills. Thank you. Chris Sneden, who served as my advisor during my first two years at UT, helped facilitate my transition to the Sandia project and was always willing to put up with my pessimism and self-doubt. Thank you. And of course, my current advisors, Don Winget and Mike Montgomery deserve credit. They recruited me to work at Sandia and ultimately made this thesis happen. Thank you.

The staff at Sandia, as well as my fellow graduate students also played a large role in this dissertation. Jason Jaacks, the only graduate student who could match my cynicism, sarcasm, and pessimism during the first two years at UT should not go unmentioned. Thank you. Thomas Gomez, the resident theorist of our Sandia team, provided me with much support during my initial time at the labs. Interacting with him has made me a better consumer of theory and I have tremendous respect for his love and understanding of the subject. Thank you. Ross Falcon, my main mentor at Sandia, always was the picture of optimism and a 'can-do' attitude. Thank you. Jim Bailey, and Taisuke Nagayama, and Guillaume Loisel, the Sandia staff members who were always willing to criticize my work and help me improve as a scientist. They inspired me to work harder and become better at what I do. Thank you. I express additional gratitude to Guillaume Loisel for providing me with the Z-machine flux values needed for the simulations presented in Chs. 3 and 7. Thank you. Greg Rochau, the man behind the scenes, always fought for

our project and ensured its continued existence. Thank you. The seemingly endless list Sandia technicians and staff members who also worked on this project deserve credit: Dan Scoglietti, Keven MacRunnels, Ricardo Medina, Dave Bliss, Sonal Patel, Adam York, Keegan Sheldon, Joseph Hanson, Linda Nielsen-Weber, Pat Lake, and the entire center section team. Thank you.

Finally, I'd like to thank the people who have no idea they contributed to my thesis. The makers of many YouTube channels that kept me entertained and sane throughout the years - The Switcher, Lord Vega, Achievement Hunters, and many more. The producers and actors of many shows on Netflix - The Office, Friends, Scrubs, The Simpsons, Seinfeld and others. Your contribution has been invaluable.

The Behavior of Hydrogen and Helium at White Dwarf Photosphere Conditions

Publication No. _____

Marc-Andre Schaeuble, Ph.D.
The University of Texas at Austin, 2018

Supervisor: D. E. Winget
Co-Supervisor: M. H. Montgomery

White Dwarfs (WDs) represent the evolutionary endpoint for nearly all stars in the universe. Their atmospheres are usually dominated by either hydrogen, helium, or carbon. In astrophysics, WDs are used to determine the age of the universe, to test current stellar evolutionary models, and to constrain the physics of Type Ia supernovae as well as dark energy. Accurate WD masses are needed for all of these applications. In this thesis, I review the weaknesses of the currently available WD mass determination methods and show that for hydrogen-dominated WDs, such deficiencies can be traced to an incomplete understanding of H line shapes at the atmospheric temperatures and densities ($T_{\rm e} \sim 1$ eV, $n_{\rm e} \sim 1{\times}10^{17}$ cm^{-3}) of those stars. I further demonstrate that helium WD mass derivation techniques suffer from uncertain Stark shift and neutral broadening models, while C WD masses are suspect due to unverified electron broadening parameters. Addressing each of these

atomic physics limitations requires both experimental data and theoretical developments. The White Dwarf Photosphere Experiment (WDPE) at Sandia National Laboratories Z-machine delivers laboratory data directed at solving the mass determination problems for WDs. For hydrogen line shapes, I find that fundamental assumptions regarding emission and absorption processes may not be valid. Helium WD mass derivations are hampered by the inability of current models to reproduce my experimental He shift and neutral broadening measurements. Since C WDs are at higher temperatures than H or He WDs, these investigations are limited to proof-of-concept experiments. All my WDPE results have led to additional questions about fundamental physical assumptions that are relevant not only to stellar atmospheres and the experimental platform, but all of plasma physics. I discuss each of these aspects in the context of atomic, plasma, and WD physics.

Table of Contents

List of Tables

List of Figures

Chapter 1

Introduction

To understand the scientific and astronomical significance of White Dwarf stars, a fundamental knowledge of stellar evolution is required. In this chapter, I describe the birth, life, and 'death' of a garden variety low-mass star which is not part of a binary or multiple system. The sun falls into this category of stellar objects. As will become apparent, the final evolutionary stage of such stars is not a 'death' at all, but a simple remnant called a White Dwarf (WD) star. Before a star develops into a WD, it has to be born first. This marks the beginning of several physical processes that can contribute to the final chemical makeup of a WD.

The astrophysical community currently believes that most stars begin their lives as a cold, dense (T ∼10–50 K, $n_H \sim 10^3 - 10^6$ cm^{-3}, e.g. Draine 2011) H_2 gas cloud. Initially, the densities and temperatures in this H_2 cloud are not sufficient to ignite nuclear fusion, the process which allows stars to produce energy in great quantities. Upon the gravitational collapse of this cloud, which could be caused by a shock or the high mass of the system (see Shu et al. 1987, and references therein), the density and temperature at the center of this dense H_2 region will slowly begin to increase. Eventually, the

following hydrogen fusion reactions (called the $p-p$ chain) can commence (Bethe 1939; Schwarzschild 1958, and references therein):

$$\mathrm{H}^1 + \mathrm{H}^1 \longrightarrow \mathrm{D}^2 + e^+ + \nu + 1.44 \text{ MeV}$$

$$\mathrm{D}^2 + \mathrm{H}^1 \longrightarrow \mathrm{He}^3 + \gamma + 5.49 \text{ MeV}$$

$$\mathrm{He}^3 + \mathrm{He}^3 \longrightarrow \mathrm{He}^4 + \mathrm{H}^1 + \mathrm{H}^1 + 12.85 \text{ MeV}$$

The occurrence of the above nuclear reactions mark the beginning the newly-born star's main sequence evolution (see '1' in Fig. 1.1). Since most stars, including the sun, consist mostly of hydrogen (Payne 1925; Lodders 2003), this evolutionary stage is by far the longest in a star's nuclear fusing lifetime. It is estimated that the sun and stars with comparable masses will burn hydrogen for $\sim 12 \times 10^9$ years, while the total fusion lifetime is currently calculated to be $\sim 12.13 \times 10^9$ years (Schröder & Connon Smith 2008).

The main byproduct of hydrogen fusion is He^4 (see above equations). Evolution of a star along the main sequence results in a slow build-up of helium in its core. Temperatures and densities required to ignite this helium are not reached during a low-mass star's main sequence lifetime. Consequently, the helium in the star's center will become inert and displace any hydrogen fusion to a shell around the stellar core. This signals the beginning of a new stellar evolutionary phase (see '2' in Fig. 1.1).

The star is now on the so-called red giant branch of stellar evolution. Changes to its physical appearance, surface temperature (T_{eff}), and surface

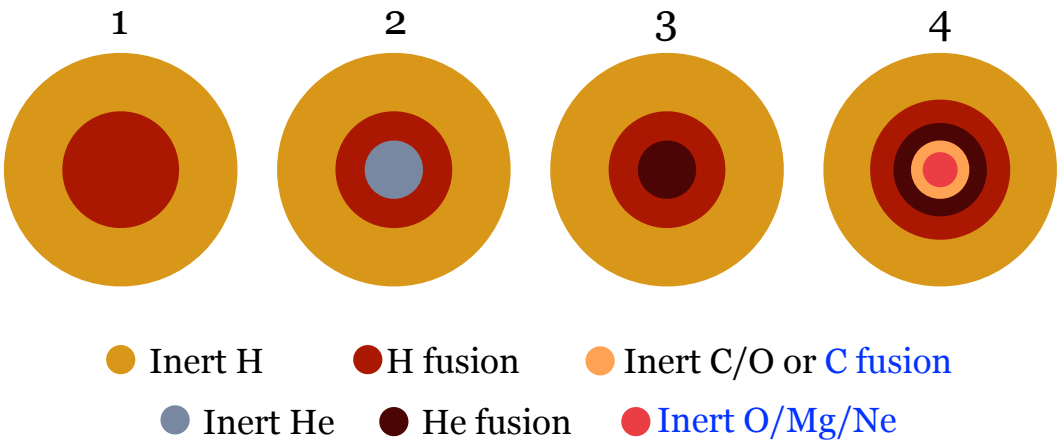

Figure 1.1: Demonstrative stages of stellar evolution. Numbers 1—4 represent different stages discussed in text. Please note that the relative sizes of different regions are not drawn to scale. Blue font is reserved for high-mass evolution.

gravity (log g) are evident. The stellar radius increases, leading to a lower $T_{\rm eff}$, decreased log g, and thus a redder color. Further evolution of the star along the red giant branch results in more He being added to the core, making it denser and hotter. The star will continue to evolve towards the so-called red giant tip where it will reach the lowest $T_{\rm eff}$ and log g values throughout its entire fusion lifetime. At this red giant tip, the star suddenly ignites its inert helium core leaving it with two sources of energy: a helium-burning center and a hydrogen-fusing shell (see '3' in Fig. 1.1). This additional fusion causes a sudden increase in temperature, which results in an almost instantaneous increase in stellar $T_{\rm eff}$ and log g. The star has now arrived on the horizontal branch, the last evolutionary stage shared by all stars similar to the sun ($0.5\ {\rm M}_{\odot} < {\rm M}_{\star} < 8.0\ {\rm M}_{\odot}$). I remind the reader that I am glossing over many

interesting phenomena in this description. Part of my Master's thesis dealt with this exciting evolutionary stage, and I encourage any interested party to consult Schaeuble et al. (2015).

Further evolution of the star, while short compared to what has happened so far, is crucial for the final product of stellar evolution and is strongly dependent on its initial mass. It is generally divided into low-mass ($0.5\ M_\odot < M_\star < 8.0\ M_\odot$), and high-mass ($8.0\ M_\odot < M_\star < 10.0\ M_\odot$) evolution. Helium fusion in low-mass stars will produce a C/O core through the triple-alpha process (Salpeter 1952; Schwarzschild 1958):

$$\mathrm{He}^4 + \mathrm{He}^4 \longrightarrow \mathrm{Be}^8 - 91.8\ \mathrm{keV}$$

$$\mathrm{Be}^8 + \mathrm{He}^4 \longrightarrow \mathrm{C}^{12} + 7.37\ \mathrm{MeV}$$

$$\mathrm{C}^{12} + \mathrm{He}^4 \longrightarrow \mathrm{O}^{16} + \gamma + 7.16\ \mathrm{MeV}$$

These nuclear reactions eventually lead to a quadruple layered star: an inert hydrogen layer on the very outside, followed by a hydrogen-burning layer, a helium-burning layer, and finally an inert C/O core (see '4' in Fig. 1.1). This is called an asymptotic giant branch (AGB) star, since its evolution now resembles that of a red giant, which was discussed above. The details of AGB evolution are poorly understood, yet significant for the subsequent WD (see Herwig 2005, and references therein). In a scenario proposed by Werner & Herwig (2006), the continued H fusion will produce more He, which could potentially ignite. If this process, called the 'helium shell flash', occurs, a

WD with a helium-dominated photosphere could result. Otherwise, the ABG phase may produce a WD with a hydrogen-dominated photosphere. It should be noted that no consensus regarding the veracity of this scenario with respect to the origin of hydrogen and helium WDs exists within the astrophysical community. More details about these processes are given in Chs. 2 and 5.

The AGB phase for high-mass stars begins with the fusion of C and O to produce Mg and Ne. The nuclear reactions are as follows (Salpeter 1952; Hoyle 1954; De Loore & Doom 1992):

$$\mathrm{C}^{12} + \mathrm{C}^{12} \longrightarrow \mathrm{Ne}^{20} + \mathrm{He}^{4} + 4.617 \text{ MeV}$$

$$\mathrm{C}^{12} + \mathrm{C}^{12} \longrightarrow \mathrm{Mg}^{23} + \mathrm{n}^{1} - 2.599 \text{ MeV}$$

Theoretically, the main effect of this additional fusion episode is the creation of a WD with a O/Mg/Ne core (see blue font '4' of Fig. 1.1). Such cores lead to an increased stellar mass and therefore also a massive WD as the end product. Due to higher stellar mass required to commence the above nuclear reactions, it is believed that WDs with O/Mg/Ne cores can provide insight into the evolution of high-mass stars (Dufour et al. 2011).

Towards the end of the AGB phase, it is thought that the evolution of low- and high-mass stars becomes similar again. The nuclear fuel depletes resulting in severe changes to the stellar hydrodynamic and thermodynamic equilibrium. The stars begin to pulsate. Theoretical models predict that these instabilities cause the star to lose a significant amount of mass and leave it

with only the inert core (made up of either C/O or O/Ne/Mg) and a thin layer of gas surrounding it. Unfortunately, many details of this final AGB phase are poorly constrained both observationally and theoretically (e.g., Iben 1967; Iben & Renzini 1983; Habing 1996; Wood et al. 2004, and references therein). Once the AGB phase is complete, the stellar object is called a 'planetary nebula', which is nothing more than a WD surrounded by the remnants of its previous life.

The evolutionary stages I describe above lead to a variety of WDs. Those with hydrogen-dominated atmospheres, which are termed 'DA' (Sion et al. 1983), make up about 80% of all known WDs (Koester et al. 1981). So-called DB WDs have helium-dominated atmospheres and make up $\sim 20\%$ of all WDs (Koester & Kepler 2015). Both DAs and DBs are thought to have C/O cores and could therefore be remnants of lower mass stars like the sun. More exotic WDs contain carbon in their atmospheres, and are named DQs. They are believed to have O/Ne/Mg cores and could thus evolve from higher mass stars. All three WD types will be discussed in this thesis. Since DA WDs are present in such great numbers, they have been the focus of many astronomical inquiries (e.g., Liebert 1980; Winget & Kepler 2008; Hansen & Liebert 2003, and references therein). It is consequently believed that the evolutionary history of single (i.e., not members of a binary or multiple system) DAs as well as fundamental aspects about their atmospheric structure are reasonably well understood.

The same cannot be said for other types of WDs. The evolutionary

history for DBs (e.g., Fontaine & Wesemael 1987; Eisenstein et al. 2006; Voss et al. 2007; Bergeron et al. 2011; Koester & Kepler 2015), and DQs (e.g., Althaus et al. 2009; Córsico et al. 2009; Dufour et al. 2011; Schwab et al. 2016) is still being researched. Several problems plague these investigations: first, the fundamental evolutionary difference between DAs and all other WDs is presently unknown. Second, the astrophysical community's primary means of solving this issue relies on their ability to precisely determine atmospheric parameters of these stellar objects. Such a determination is currently difficult due to weaknesses in the atomic models used for these purposes.

Accurate stellar parameters are not only needed to understand the evolutionary history of WDs, but they also allow for the application of these stellar remnants to study a wide variety of astronomical and physical problems. The hottest currently known WDs have temperatures of ∼200,000 K (Werner & Rauch 2015). The coolest ones exhibit $T_{\rm eff}<$ 3,000 K (Kaplan et al. 2014). In mass space, WDs range from ∼1.35 $M_{\odot}$ (Burleigh et al. 1999) to ∼0.14 $M_{\odot}$ (Brown et al. 2016). It is precisely this large parameter space that leads to the versatility of WDs.

An important application of WDs is their use as galactic chronometers (e.g., Winget et al. 1987; Gianninas et al. 2015). The logic behind this approach is simple. WDs are, by definition, the most evolved stellar objects in any astrophysical system. Therefore, if the oldest WD in a system such as the Milky Way is found, a lower age limit of the Galaxy can be derived. Extracting the needed WD ages requires accurate stellar mass measurements. The

results of the currently most popular mass extraction method, which consists of fitting model atmosphere calculations to observed WD spectra, rely almost exclusively on atomic input data. As I demonstrate in Ch. 5, this so-called spectroscopic approach does not produce internally consistent WD masses. My experimental investigations into this problem reveal that this issue is significant and must be resolved if WDs are to be used as accurate chronometers. Please see Chs. 2 and 5 for more information.

WDs can also be used to derive initial-final stellar mass relations (IFMR, Sweeney 1974; Weidemann 2000, and references therein). These IFMRs constrain the formation mechanisms of WDs and give insight into the poorly understood stellar mass loss between the birth of a star and the WD stage (e.g., Auer & Woolf 1965; Cummings et al. 2015, 2016, and references therein). WDs in stellar clusters are generally used to derive the IFMR since two age indicators are needed for these investigations. The first indicator is the cluster age, which gives the point in time at which star formation began in the cluster. The second indicator is the WD cooling age, which gives the length of time a star has spent in the WD evolutionary stage. Since the cluster WDs are most likely remnants of the first stars formed in the cluster, subtracting their cooling age from the total cluster age results in the WD progenitor evolutionary time until the end of the AGB phase. In combination with stellar evolutionary models, this progenitor evolutionary time can then be used to derive the initial WD progenitor mass. Comparing the measured WD mass to that of the progenitor leads to the IFMR. Just like with the application of WDs to derive the Milky

Way age, these IFMR investigations suffer from uncertain stellar masses and ages.

Further applications of WDs include the direct observation of extrasolar planet compositions (e.g., Alcock et al. 1986; Zuckerman & Becklin 1987; Debes & Sigurdsson 2002; Zuckerman et al. 2007; Farihi et al. 2014). Due to the large gravitational field of WDs, any rocky body in their vicinity will be disrupted and eventually accrete onto the star. Spectral lines of the elements contained in the rocky body will then appear in the WD atmosphere. In combination with accurate WD $T_{\rm eff}$ and log g values, a careful analysis of these spectral features reveals the chemical composition of the circumstellar object. However, significant challenges in the derivation of the needed atmospheric parameters for all major types of WDs exist, severely limiting the application of these stars to the study of exoplanet compositions.

Outside the realm of astronomy, WDs can also be used to directly test several physics models. Onofrio & Wegner (2014) present evidence that DQ WDs might be used to constrain our understanding of general relativity. Specifically, they show that in the vicinity of a strong gravitational source (such as a WD), current Higgs field theory predicts a change in electron mass, while leaving the nuclei of atoms unaffected. If these predictions are correct, a wavelength shift should be observed in spectral lines of atomic electronic transitions (which are dominated by electron masses) emanating from a WD atmosphere. The wavelengths of molecular transitions (which are dominated by nuclei masses), however, should remain unchanged. DQ WDs, which may

contain both molecular and electronic transitions, are candidate astrophysical objects available to test these predictions.

Neutrino cooling and crystallization in dense Coulomb plasmas are additional physics effects that can be studied using WDs. Winget et al. (2004) show that the weak interaction between electrons and neutrinos can be tested using variable DBs. The cooling in the cores of these stars is dominated by neutrinos. Since their cores are dense, the probability of a weak interaction between an escaping neutrino and another particle increases. According to Winget et al. (2004), these interactions are so significant in DB WDs that they change the observed variability of these stars, thereby providing a test for the electroweak theory. Crystallization in dense Coulomb plasmas releases additional energy (or latent heat). This will manifest itself in changes to the observed WD luminosity distribution since it alters the cooling of these stars (Salpeter 1961; van Horn 1968). Winget et al. (2009) demonstrate that WD measurements can be used to gain insight into this important plasma effect.

WDs clearly have many applications in astrophysics, most of which require either accurate atmospheric parameters or masses as input. The methods used to extract the needed values are flawed for all WDs. For DA WDs, the generally applied method suffers from internal inconsistency issues that most likely stem from inaccurate atomic data. The Galactic age measurements derived from these stars are therefore currently questionable. The situation is worse for DBs since multiple atmospheric parameter determination methods are deficient. An equivalent argument can be made for DQ WDs. All these

issues share a common root cause: inaccurate atomic input data. In Ch. 5, I show that inconsistencies observed in DAs are also found in my experimental spectra. I further demonstrate that these irregularities may arise due to *flaws in commonly applied fundamental assumptions* made about *basic atomic processes* in plasmas. The research I present in Ch. 6 is directly aimed at atmospheric parameter determination weaknesses in DBs. My experimental data indicates that several different basic physical effects, such as spectral line shift and broadening, are improperly modeled in helium atmospheres. DQ WDs, which were only discovered about a decade ago, also suffer from mass determination uncertainties, which can be traced to uncertainties in atomic carbon models. In Ch. 7, I present an updated WDPE platform designed to reach DQ atmospheric conditions.

Despite the fact that this introductory chapter primarily gives astrophysical motivations for my work, the main body of my thesis examines the constitutive physics of astronomical models using at-parameter laboratory astrophysics experiments. This research field has many advantages over traditional observational astronomy. First, laboratory astrophysics is an *active* science in which the researcher directly contributes to the design and execution of an experiment. Traditional astronomy is *passive* and an experiment consists of a non-interactive observation. Second, important plasma effects such as gradients, which may influence the behaviors of atoms in these systems, can be directly investigated in experiments (see Ch. 5). Third, single effects that are to be studied can be much more easily isolated (see Ch. 6). Extracting

fundamental parameters like temperature and density is generally also much more straightforward in laboratory plasmas as compared to astrophysical objects. For all these reasons, I chose to dedicate my PhD research to this field. I hope you, the reader, are just as excited about this thesis as I am.

Chapter 2

Masses of WD Stars

Atmospheric parameters and masses of WD stars are crucial to understanding their evolution. These parameters also allow the application of WDs to other areas of astronomy and physics (see Ch. 1 for more details). I describe in this chapter the methods that can be used to derive these parameters and how the results compare with each other. The most common method to extract the mass is through the derivation of atmospheric parameters ($T_{\rm eff}$, log g) and subsequent application of evolutionary models to those values (e.g., Bergeron et al. 1992; Fontaine et al. 2001, and references therein). See Sec. 2.1.1 for more details about this approach. I discuss two common direct WD mass measurement methods in Secs. 2.1.2 and 2.1.3.

2.1 WD mass determination methods

2.1.1 The spectroscopic method

The most popular WD mass determination technique is called the spectroscopic method. This approach relies on fitting model atmosphere calculations to observed WD spectra. It was pioneered by Bergeron et al. (1992) and has been used to infer the parameters of tens of thousands of WDs (e.g., Hu

et al. 2007; Gianninas et al. 2011; Kleinman et al. 2013; Kepler et al. 2016). The advantages of this method are obvious. First, it is a straightforward and easy procedure for observers to extract atmospheric parameters from only the stellar spectrum. This is not true of the other mass determination methods discussed in Sec. 2.1.2 and 2.1.3. Second, the *individual* mass of nearly any WD can be derived using this method. Flux, distance, and binary membership restrictions of other mass determination techniques do not apply. However, the convenience of this method comes at a cost: the resulting WD atmospheric parameters and masses rely heavily on the atomic data used in the model atmosphere calculation. And there's the rub (Shakespeare 1602).

2.1.2 The gravitational redshift method

Another powerful approach for extracting WD masses is called the gravitational redshift (GR) method. This technique relies on the principles of general relativity. Due to the large gravitational field of a WD, any photon leaving its surface will lose energy. For an average-mass WD, this energy loss manifests itself in a $\sim$1 Å shift of spectral lines (e.g., Adams 1925; Greenstein & Trimble 1967; Falcon et al. 2010, 2012; Barstow et al. 2005). The following equation relates this shift to the WD mass:

$$v_g = \frac{c\Delta\lambda}{\lambda} = \frac{GM}{Rc} \tag{2.1}$$

Unfortunately, other effects such as the Doppler shift dominate the GR. In the case of a very select group of stars (e.g., 40 Eri, and Sirius B) the velocity

shift can be accounted for through astrometric measurements (Popper 1954; Barstow et al. 2005, 2017). A different approach to must be employed account for the Doppler shift of spectral lines observed in all other WDs.

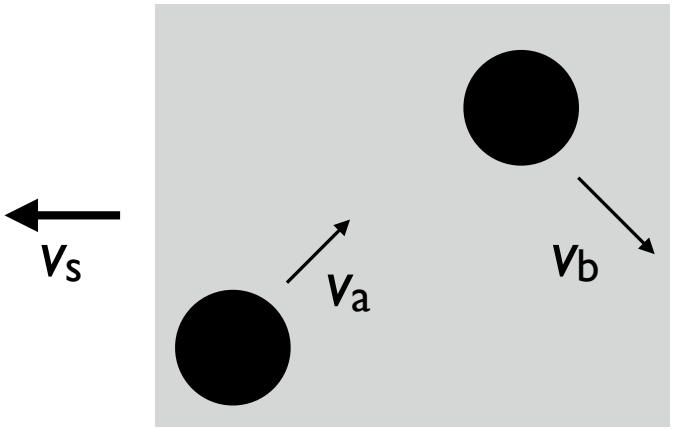

Figure 2.1: A sample of two WDs moving with individual velocities v_a and v_b. These stars have a bulk velocity of v_s, meaning that they are part of the same co-moving sample.

To correct for spectral line velocity shifts in WDs for which astrometric measurements are not possible, a simple approach is to only consider WDs that are part of the local, co-moving sample of stars (Falcon et al. 2010). Fig. 2.1 shows just two stars of this sample. Their velocity contributions can be separated into two components: individual random motions (v_a and v_b in Fig. 2.1) and the bulk motion of the sample (v_s in Fig. 2.1). If the number of individual WDs in the considered co-moving is large enough, the mean of their individual random motions (v_a and v_b) is zero. Averaging thus removes the individual velocity contributions from the stellar spectra. The local standard

of rest, which defines the velocity of all stars that are part of the local, co-moving sample (v_s in Fig. 2.1) is well known (Kerr & Lynden-Bell 1986) and can therefore also be accounted for. Once both of these corrections have been applied to the observations, the WD spectra will only suffer from one more shift: the gravitational redshift. With the help of Eq. 2.1, this final shift is translated to the mean mass of the considered WDs. Due to the required velocity averaging, individual stellar masses generally cannot be derived using the GR approach.

2.1.3 The astrometric method

Among the first WDs to be discovered and studied are 40 Eri and Sirius B. Both of these objects are part of multi-body systems (e.g., Heintz 1974; Gatewood & Gatewood 1978; Shipman et al. 1997; Bond et al. 2017). A therefore obvious method for obtaining the masses of the constituent members of the stellar systems is to measure their motion and solve the associated Newtonian equations. While this is a relatively simple and powerful approach, it suffers from several weaknesses. The WD under consideration needs to be part of a multi-body system. According to Holberg (2009), only ∼32% of all WDs fulfill that requirement. Of these 32%, only very few are close enough to earth to be observed in detail. There are additional limitations concerning the motion of the WDs. The interstellar distance in an ideal system has to be sufficiently large so that mass transfer is not an issue but also small enough for the change in position to be measured in a reasonable amount of time. This last

requirement is certainly not the case for Stein 2051B, although that star was recently used in gravitational bending measurement of its mass (Sahu et al. 2017). The astrometric method has only been successfully applied to three WDs (Sirius B, Procyon B, and 40 Eri B, Provencal et al. 1998). It is thus clear that the other mass determination methods outlined in Sec. 2.1.1 and 2.1.2 are needed to derive WD masses and therefore apply these stellar objects to astrophysical problems.

2.2 The application of WD masses to astrophysical problems

2.2.1 DA WDs and the age of the Galaxy

In Ch. 1, I mentioned that DAs can be used to determine the age of the Milky Way. I present a more complete picture of this assertion here. Before describing the details of this method, the correlation between the stellar luminosity and its temperature has to be established. These two parameters are connected through the following equation:

$$L_\star = 4\pi\sigma R_\star^2 T_\star^4 \tag{2.2}$$

where $L_\star$, $R_\star$, and $T_\star$ reference the stellar luminosity, radius, and surface (or effective) temperature. The effective temperature is defined to be the temperature at which the star and a blackbody emit the same integrated flux. The constant σ in Eq. 2.2 represents the Stefan-Boltzmann constant.

WDs do not create significant amounts of energy through fusion processes. Their temperatures and luminosities are therefore constantly *decreas-*

ing as a function of time. Consequently, the luminosity of a WD is directly related to its age. A theoretical description of this connection was first provided by Mestel (1952). I will use the relationship presented in that paper to demonstrate the fundamental approach to using WDs as chronometers. I remind the reader that much work has been done on this subject since (e.g., van Horn 1971; Winget et al. 1987; Fontaine et al. 2001; Hansen & Liebert 2003; Camisassa et al. 2017). Nonetheless, Mestel's theory allows for unique insight into the link between the age of a WD and its luminosity.

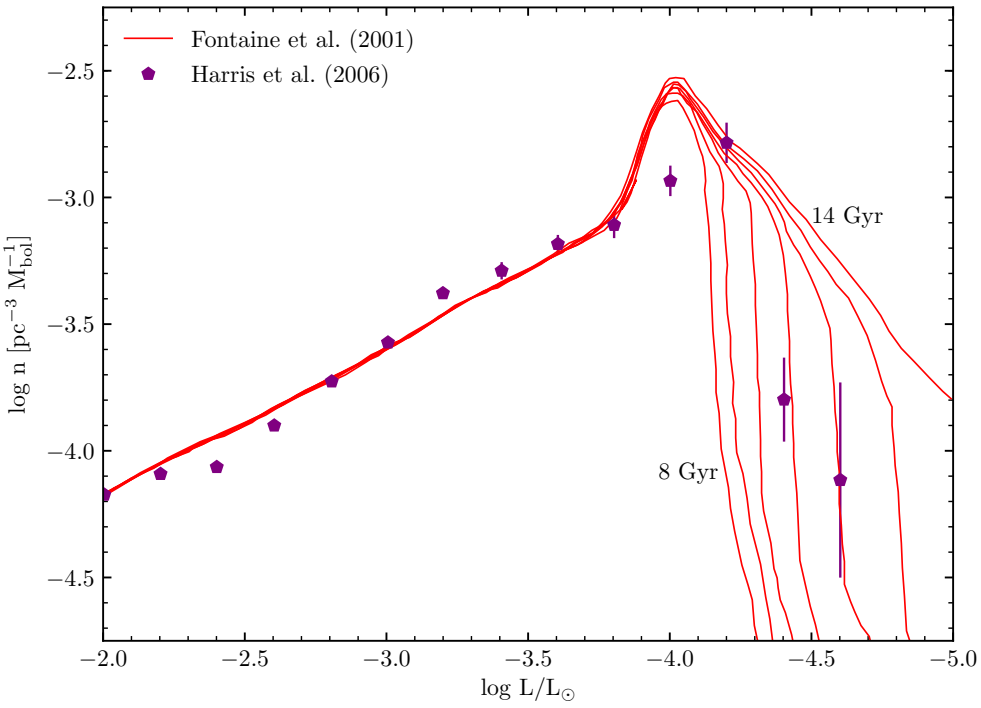

Figure 2.2: Comparison of theoretical (Fontaine et al. 2001) and observed (Harris et al. 2006) WD luminosity functions. Challenges for this method of determining ages of stellar systems are obvious.

The main result of Mestel's cooling theory can be summarized as follows:

$$\tau_{\rm cool}^{\rm Mestel} \propto M^{5/7} L^{-5/7} \ \ {\rm yrs} \tag{2.3}$$

While several physical effects have been ignored in the derivation of this equation (see van Horn 1971 for more details), Eq. 2.3 clearly relates the WD age to its mass and luminosity. Fig. 2.2 demonstrates the application of Eq. 2.3 to the WD galactic age determination method. In that plot, I show evolutionary calculations that estimate the number of WDs at a given luminosity (Fontaine et al. 2001, red lines) for different Milky Way ages. I also plot the Harris et al. (2006) observational results for the Galaxy (purple pentagons). A clear drop-off in the number of WDs at log $L/L_{\odot}$ $\sim$ -4.2 can be seen for both the theoretical calculations and the observations. Such a decline is expected because the luminosity of WDs always decreases as a function of time (see above). Therefore, WDs will reach some lower luminosity limit in a stellar population with a finite age (i.e. the Galaxy). The location of this drop-off in luminosity space allows an observer to determine the population age. This is evident from the red curves labeled '8 Gyr' and '14 Gyr' in Fig. 2.2. Based on the Fontaine et al. (2001) models, the Harris et al. (2006) data can be used to derive a Galactic age of 11.5$\pm$0.7 Gyrs.

The preceding discussion highlights the dependency of the inferred galactic age on the WD luminosity. According to Eq. 2.3, however, this age also depends on the assumed WD mass. The Fontaine et al. (2001) calculations shown in Fig. 2.2 assume a mean mass for the DA population of 0.585 $M_{\odot}$. This

mean mass is derived using the spectroscopic method I describe in Sec. 2.1. How does the spectroscopic mean mass of the DA population compare to that derived using the gravitational redshift? If they are significantly different, how does that influence the derived galactic age? Answering these questions requires a more detailed description of both the spectroscopic and gravitational redshift methods for DAs. I will begin with the spectroscopic method.

Detailed Balmer line shape calculations are the basic ingredient to any DA WD atmosphere model used in the spectroscopic atmospheric parameter extraction approach for those stars (Bergeron et al. 1992). Hydrogen line shapes are of great interest to both the physics and astronomy community. Vidal et al. (1970) made the first significant forays into the subject by calculating the Balmer line series at temperatures and densities found in WD atmospheres. These calculations served as the standard in WD astronomy until the introduction of the Tremblay & Bergeron (2009, hereafter TB09) hydrogen lines profiles. With the introduction of the TB09 line profiles, the mean mass of the DAs was raised from the 0.585 $M_{\odot}$ adopted by Fontaine et al. (2001) to $\sim$0.61 $M_{\odot}$. However, the standard deviation amongst different studies measuring the mean mass of the DAs also increased significantly. In Fig. 2.3, I show the results of major studies trying to determine the mean DA mass before and after the publication of the TB09 line profiles.

From Fig. 2.3, several weaknesses of the spectroscopic method are evident. First, the derived DA mean mass since the introduction of the TB09 has increased, but few studies have been able to recreate those results (see

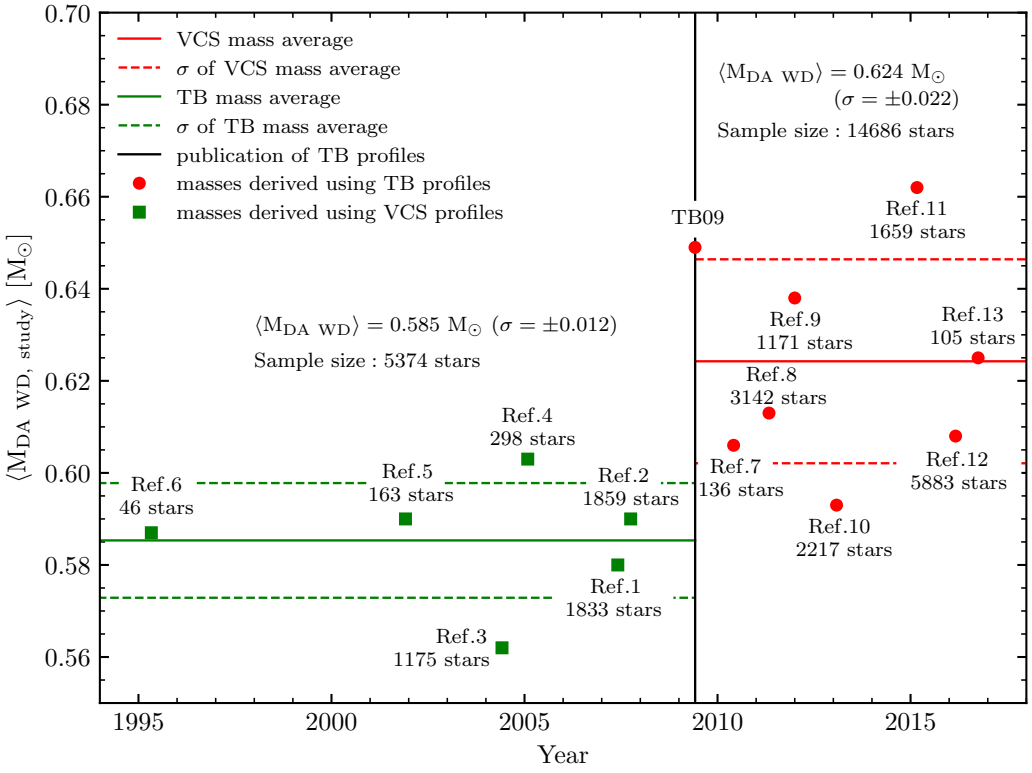

Figure 2.3: Comparison of mean mass of DA WDs derived from different studies. The mean mass derived before and after the release of the TB09 hydrogen line profiles differs by about 0.04 $M_\odot$, which is not enough to account for the GR-spectroscopic difference. Additionally, the standard deviation of the observed mean mass increased by a factor of 2 after the introduction of TB09 profiles. Questions about the spectroscopic thus remain. Ref. 1: Hu et al. (2007), Ref. 2: Kepler et al. (2007), Ref. 3: Liebert et al. (2005), Ref. 4: Madej et al. (2004), Ref. 5: Koester et al. (2001), Ref. 6: Bragaglia et al. (1995), Ref. 7: Limoges & Bergeron (2010), Ref. 8: Tremblay et al. (2011), Ref. 9: Gianninas et al. (2011), Ref. 10: Kleinman et al. (2013), Ref. 11: Kepler et al. (2015), Ref. 12: Kepler et al. (2016), Ref. 13: Tremblay et al. (2016).

black vertical line and TB09 identifier in Fig. 2.3). Second, the DA mean mass of all post-2009 studies is 0.624±0.022 $M_{\odot}$. Stated mass errors on the spectroscopic method are at the 1% level, making the scatter in the different studies significant. A third weakness of the spectroscopic method, which is not evident from Fig. 2.3, is its inability to produce internally consistent atmospheric parameters. Please see Ch. 5 for more information on this issue. Given that the line profiles across all studies are the same, the difference in derived masses can stem only from two other components of the parameter derivation methodology: the input atmospheres and the fitting approach. The calculation of WD atmospheres is well outside the scope of this thesis and I will therefore guide the interested reader to the following two papers for reviews of the two models most commonly used in WD astronomy: Liebert et al. (2005) and Koester (2010). Possible effects of the fitting procedure on derived $T_{\rm eff}$ and log g values were explored by me using TLUSTY (Hubeny & Lanz 1995) and the XENO (Ferri et al. 2014; Gomez et al. 2016, 2017) line profiles. The results of my investigation can be found in App. A. Despite all these problems, the spectroscopic technique is the only broadly-applicable method that results in individual stellar masses, which are needed for IFMR studies (see Ch. 1), globular cluster age determinations (e.g., Richer et al. 1997), and investigations of other, less numerous WD types such as DQs (see Ch. 7).

The above discussion and Fig. 2.3 highlight inherent issues with the spectroscopic method. Due to the increased uncertainty in DA mean mass after the publication of the TB09 calculations, it is unclear how much the

inclusion of those line profiles shifted this measurement. I therefore adopt a value of 0.608±0.012 $M_{\odot}$(average of all studies shown in Fig. 2.3) for the following analysis. Using the gravitational redshift method (see Sec. 2.1.2), Falcon et al. (2010) derive 0.650±0.020 $M_{\odot}$ for the DA mean mass in the SPY sample (Napiwotzki et al. 2001). The spectroscopic and GR masses for this population therefore disagree by ∼7%. The galactic age increases by ∼0.5 Gyrs with the application of the DA GR mean mass to Eq. 2.3. As stated above, the errors on the age measurement are ∼0.7 Gyrs, making such an increase seem inconsequential. These errors, however, are mainly dominated by the fact that only very few WD observations at low luminosities are possible. Bigger telescopes and more large-scale surveys should help alleviate such problems.

Without context, a difference in Galactic age of 0.5 Gyrs will stump the non-expert reader. In simulations exploring the the chemical evolution of our Galaxy (e.g., Rocca-Volmerange & Schaeffer 1990; van den Bergh 1991), as well as calculations seeking to constrain the star formation rate and initial mass function of the Milky Way (e.g., Tremblay et al. 2014; Kilic et al. 2017), accurate galactic ages serve as a crucial observational input. A 0.5 Gyr age increase could have significant effects on such investigations. As pointed out by Winget et al. (1987), WDs can also be used to constrain the age of the universe. A change in that parameter due to uncertain WD masses has significant implications for the understanding of large-scale cosmological evolution of the universe (see Bennett et al. 2003, and references to that article).

It is now obvious that the DA WD mean mass is a crucial parame-

ter that has far-reaching astrophysical consequences. The remaining question that has to be answered is this: is the spectroscopic or gravitational redshift mean DA mass more accurate? The GR mass determination method is more straightforward from a physics standpoint. It does not rely on complicated atomic models. Masses inferred from that technique should thus be more representative of reality. Discrepancies between the GR and spectroscopic DA masses therefore imply weaknesses in the hydrogen line profiles used in the spectroscopic method. A thorough experimental and theoretical investigation into hydrogen line formation physics applicable to DA atmospheres is presented in Ch. 5.

2.2.2 The evolutionary origin of DB stars

The basic structure of DA WDs is described by current stellar evolution models. The existence of DBs, however, cannot be explained without invoking an additional mechanism that rids almost the entire stellar atmosphere of hydrogen. These mechanisms usually operate under one of two assumptions: (i) DAs and DBs share the same evolutionary origin or (ii) DAs and DBs are fundamentally different. Starting with Fontaine & Wesemael (1987), the prevailing view of the community has been that option (i) is the correct explanation for these objects. The proponents of this theory invoke atmospheric convection arguments to account for the presence of DB WDs (e.g. Bergeron et al. 2011). If this theory were true, the mean mass of the DA and DB populations should be equal.

Another process through which a DB WD can be created is outlined in (Werner & Herwig 2006). In this theory, the DB progenitor star experiences a particularly violent fusion episode during the asymptotic giant branch of stellar evolution that mixes the inert hydrogen layer into the helium burning shell, thereby destroying almost all H in the atmosphere and creating a DB WD. The DB mass signatures resulting from this model are unclear, but the resulting mean DB mass would most likely differ from that of DA WDs.

Nather et al. (1981) present an additional DB creation mechanism. They describe the evolution of G61-29, an interacting binary system that, through an eventual merger, could produce a single DB star . Further evidence presented in that paper suggests that *all* DBs may have developed through this evolutionary channel. The Nather et al. (1981) model is expected to result in DBs whose mean mass matches that of the DAs. However, the distributions of the two WD populations would most likely disagree. I summarize all potential DB evolutionary channels and their associated mass prediction signatures in Table 2.1.

The preceding discussion demonstrates the need for an accurate DB population mass measurement. No known non-interacting DB binary systems exist, leaving only the spectroscopic and GR mass determination methods. Since the numbers of DBs compared to DAs are much smaller, there have been far fewer spectroscopic studies of these objects. The to-date largest investigations are Eisenstein et al. (2006); Voss et al. (2007); Bergeron et al. (2011) and Koester & Kepler (2015), with only this last study delivering sig-

Table 2.1: Possible DB evolutionary channels and their likely mass signatures

DB evolutionary channel	**Predicted mass signatures**
atmospheric convection/diffusion	$\langle M_{DB} \rangle = \langle M_{DA} \rangle$
additional progenitor fusion	$\langle M_{DB} \rangle \neq \langle M_{DA} \rangle$ $\sigma(M_{DB}\rangle) = \sigma(\langle M_{DA}\rangle)$
binary evolution	$\langle M_{DB} \rangle = \langle M_{DA} \rangle$ $\sigma(\langle M_{DB}\rangle) \neq \sigma(\langle M_{DA}\rangle)$
combination of progenitor fusion and binary evolution	$\langle M_{DB} \rangle \neq \langle M_{DA} \rangle$ $\sigma(\langle M_{DB}\rangle) \neq \sigma(\langle M_{DA}\rangle)$

nificant statistics on DB WDs. I summarize the results of Bergeron et al. (2011) and Koester & Kepler (2015) in Fig. 2.4

The atmospheric parameters shown in Fig. 2.4 were extracted using the spectroscopic fitting method described in Sec. 2.1.1. The needed line profiles are those published by Beauchamp et al. (1997). Atmospheric models and the fitting methods are similar to those for DA WDs. An unexpected increase in the spectroscopic DB log g values at low $T_{\rm eff}$ is clearly visible in Fig. 2.4. Koester & Kepler (2015) explain the sudden log g upturn by invoking atomic physics arguments. They claim that at $T_{\rm eff} \lesssim 16{,}000$ K, the broadening of He lines is dominated by neutrals in the plasma. This broadening mechanism, also called van der Waals broadening, may not be properly accounted for in models and could therefore causes this increase in log g. Bergeron et al. (2011) also observe this trend and make the same argument. However, they acknowledge that these increased surface gravity values may be real since they derive both 'reasonable' and very high log g values at these lower temperatures.

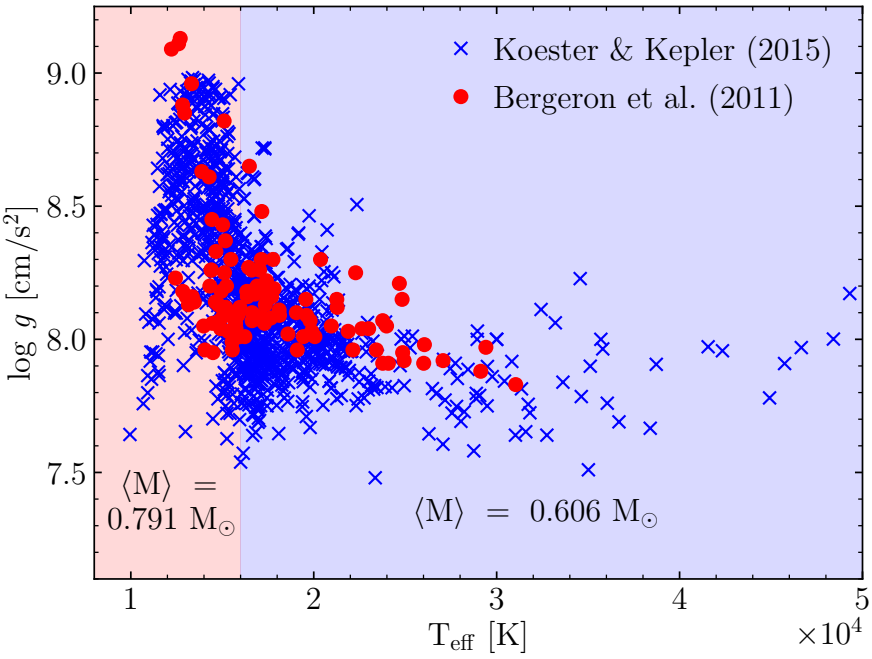

Figure 2.4: Comparison of spectroscopic DB results from Bergeron et al. (2011) and Koester & Kepler (2015). A sharp upturn in log g (mass) below $T_{\rm eff} \sim 16{,}000$ K is obvious.

Deridder & van Renspergen (1976) is the current neutral broadening theory used in DB atmospheres. Unfortunately, their calculations have *never been tested experimentally*, as all helium experiments have mostly focused on pure electron broadening (e.g. Gauthier et al. 1981; Heading et al. 1992; Büscher et al. 1995). My platform is in the unique position to perform a test of these neutral broadening calculations and therefore shed some light on the issues presented in Fig. 2.4. See Ch. 6 for more details.

DB GR mass measurements could provide valuable insight into the

spectroscopic log g upturn in Fig. 2.4. However, GR measurements for these stars need to be approached with more care than those of the DAs. Greenstein & Trimble (1967) first realized that due to the severe and line-dependent pressure shifts of helium, DB GR measurements are much more difficult. Two decades later, Koester (1987) demonstrated that these concerns had not been sufficiently addressed by experiment or theory. For the strongest He I line in the optical spectra of DBs, located at 5876 Å, the theoretical and experimental shifts never agreed (e.g., Griem et al. 1962; Cooper & Oertel 1969; Gigosos et al. 2014; Büscher et al. 1995, and references therein). Such shortcomings severely hinder GR mass measurements of DB WDs. One of the fundamental aims of this thesis is to address precisely this problem with experimental measurements. More details are given in Ch. 6. For an attempt at GR measurements of DBs, see Falcon et al. (2012). The mean mass for DBs obtained in this study ($\langle M_{DB} \rangle = 0.74\ M_{\odot}$) should be treated with caution, especially given the considerations above. A recent study by Halenka et al. (2015) demonstrated that pressure shifts are of no concern to DA WDs.

The preceding discussion demonstrates that the *DB mean mass is still an unsettled question.* All available DB mass determination methods suffer from some significant shortcoming. The spectroscopic method suffers from uncertain treatment of neutral broadening in WD atmospheres, while the GR method lacks due to poorly constrained He pressure (Stark) shifts. Hence, both mass determination methods suffer from atomic physics problems. A detailed and thorough experimental exploration of the atomic physics issues

afflicting DB mass determination methods is essential. I present the first steps in this direction in Ch. 6.

2.2.3 Exploring the origins of Type Ia supernovae with hot DQs

As a final point in this chapter, I will discuss the spectroscopic mass determination of hot DQ WDs. The objects were first described in Dufour et al. (2007) and Dufour et al. (2008). Just like with the DBs, the current standard stellar evolution model cannot explain their existence. Again, obtaining accurate masses of these DQs will constrain their evolutionary history. DQ WDs could be failed Type Ia supernovae (Schwab et al. 2016). The origin of these supernovae have been the holy grail of astrophysics for decades.

Before any astrophysical inferences using these stars can be made, masses of these objects have to be determined. Dufour et al. (2007) show that carbon atomic models at the time were not sophisticated enough to allow for an accurate spectroscopic DQ mass measurement. A re-calculation of C Stark widths and subsequent application of this data to DQ spectra revealed that these objects are significantly more massive than either DA or DB WDs (Dufour et al. 2011). Unfortunately, the updated carbon Stark widths have *never* been experimentally verified, preventing any serious investigations into the origins and scientific potential of these stars. I will give a description of my efforts to design an experimental platform to achieve this in Ch. 7.

2.3 Final thoughts on WD masses

During the discussion above, I neglected to perform a comparison between the spectroscopic, GR, and astrometric mass determination methods. The attentive reader will immediately notice that the number of WDs for which a mass can be derived using these three mass derivation techniques will be extremely small. In fact, this feat has only been attempted once by Barstow et al. (2017). The results in that paper indicate that a lot more work on all the WD mass determination is needed to unlock the true potential of WDs.

Chapter 3

Fundamentals of the White Dwarf Photosphere Experiment

In Ch. 2, I summarize the current atomic physics problems afflicting the spectroscopic and GR WD mass determination methods. These issues require both theoretical and experimental investigations. This thesis is dedicated to the experimental study of these effects. To reach the needed plasma conditions, I make use of the Z-machine at Sandia National Laboratories (SNL). I give a thorough description of this facility below. A description of the hardware design and plasma creation mechanism of the White Dwarf Photosphere Experiment (WDPE) conclude this chapter.

3.1 The *Z*-machine at Sandia National Laboratories

A significant advantage of the WDPE is its ability to perform experiments at the plasma conditions found in White Dwarf atmospheres, the outer regions of these stars that are observable with telescopes. The structure of a garden variety WD atmosphere in both electron density ($n_{\rm e}$) and electron temperature ($T_{\rm e}$) is shown in Fig. 3.1. Line formation physics are most uncertain towards the bottom of a WD atmosphere, or at $n_{\rm e} \gtrsim 3{\times}10^{17}{\rm cm}^{-3}$

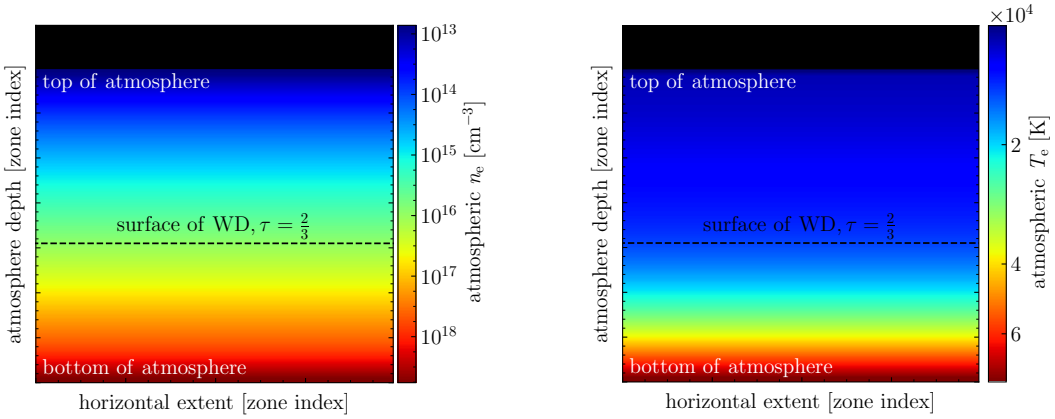

Figure 3.1: The n_e (left) and T_e (right) structure of a garden-variety WD. I also indicate the location of the 'surface' of a WD. The WDPE samples the bottom regions of a White Dwarf atmosphere, where the line-formation physics are most uncertain.

(Falcon et al. 2017). The target experimental conditions for the WDPE are thus $\sim$1–10$\times 10^{17}$ cm^{-3} in n_e and $\sim$1–1.5 eV (1 eV $\approx$ 11,604 K) in T_e. Such plasma conditions can be achieved by using a powerful X-ray source like the Z-machine at SNL.

The physics of the Z-machine have been expertly described in many publications (e.g., McDaniel et al. 2002; Bailey et al. 2006; Rose et al. 2010; Jones et al. 2014; Rochau et al. 2014). I will therefore only review the basics here. The Z facility at SNL is currently the largest pulsed power generator in the world. It can produce electrical powers in excess of 80 TW and electrical currents greater than 26 MA. This results in a total emitted X-ray energy of $\sim$2 MJ. To turn all the electrical power into an X-ray energy source for astrophysical experiments such as the WDPE, Z uses a so-called 'z-pinch

dynamic hohlraum' (ZPDH) (e.g., Bailey et al. 2006; Rochau et al. 2007; Nash et al. 2010). This device is located at the center of the Z vacuum chamber. It is comparable to a hockey puck in size and shape. I show very simplified cross-sectioned face-on view of the ZPDH in Fig. 3.2.

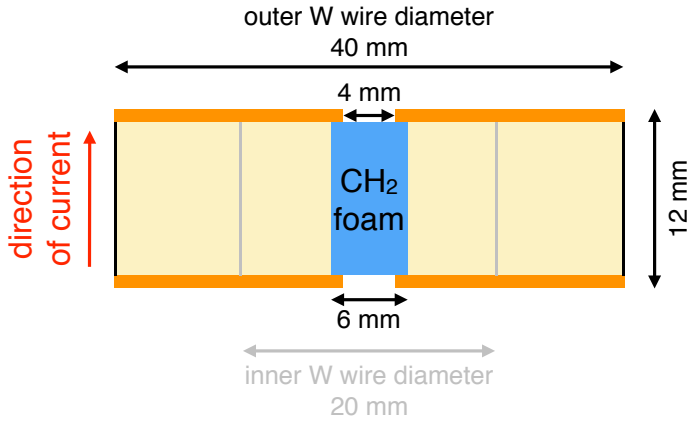

Figure 3.2: Simplified cross-sectioned face-on view of the ZPHD. All major dimensions are identified.

At its ∼40 mm (black in Fig. 3.2) and ∼20 mm diameters (grey in Fig. 3.2), the ZPHD is equipped with 240 and 120 11.4 μm diameter tungsten (W, $Z = 74$) wires respectively. For clarity, I only show a single wire pair in Fig. 3.2. A 14.5 mg/cm^3, 6 mm diameter CH_2 foam cylinder is located at the center of the ZPDH (blue in Fig. 3.2). During an experiment, the current applied to the tungsten wires turn them into plasmas. The 26 MA current also produces a large magnetic force which pushes the tungsten plasma towards the CH_2 foam cylinder at the center of the ZPDH. This process is depicted in Fig. 3.3. A radiating shock is launched into the CH_2 by the tungsten. Due to

the optical thickness of the tungsten plasma, the resulting radiation is trapped. The implosion process then increases the radiation temperature and density in the stagnation plasma (see center of Fig. 3.3). This radiation then gets passed back to the tungsten, which re-radiates it in the form of a 200 eV Planckian (Sanford et al. 2002; Foord et al. 2004). The ZPDH is designed in such a way that this X-ray energy can radiate out the top and the side of the current return can (Rochau et al. 2014, purple arrows in Fig. 3.3).

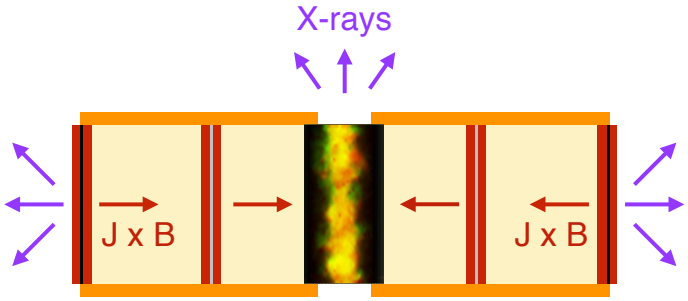

Figure 3.3: Basic demonstration of the x-ray creation mechanism in the ZPDH. The large magnetic force (J×B, maroon arrows) pushes the tungsten plasma towards the CH_2 foam. The resulting implosion (central plasma column) launches X-rays out the top and side (purple arrows).

The X-ray power as a function of time resulting from the above described process is shown in Fig. 3.4. These data were taken from Rochau et al. (2014). They represent the measured mean power averaged over 20 shots conducted between February 2012 and September 2013. The X-ray power is very reproducible, with a ∼10% deviation in the peak. Zero time in Fig. 3.4 is defined as the point when peak current has passed through the ZPDH (see Fig. 3.3). About 70% of the total X-ray power is contained in the peak (left

of blue dashed line in Fig. 3.3) with the remaining 30% being delivered by the tail to the right of the blue dashed line in Fig. 3.3). I make use of the radiation drive shown in Fig. 3.4 by placing a gas cell in the path of the resulting X-rays. The design of the experimental platform is discussed in the next section.

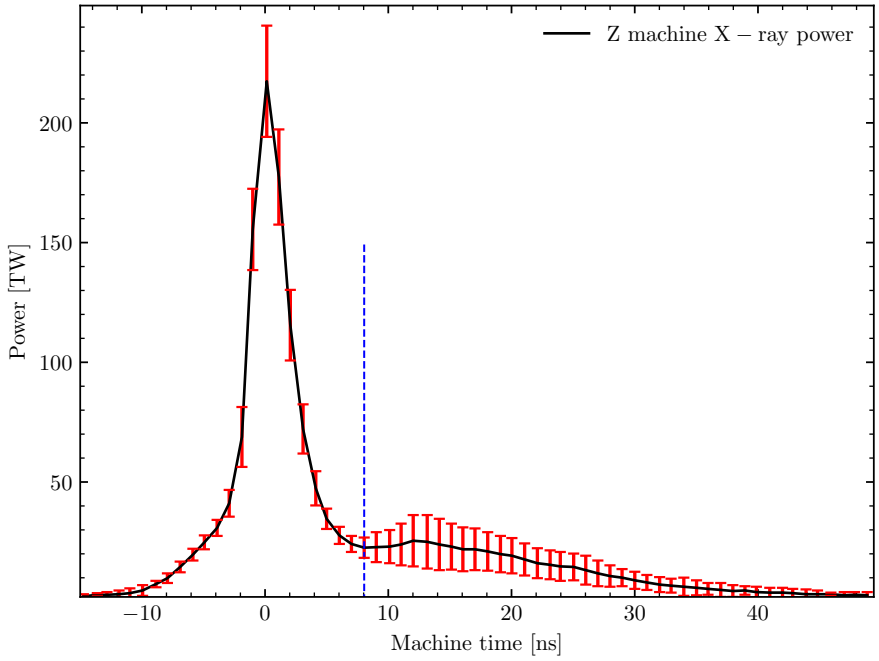

Figure 3.4: Measured x-ray power time history averaged over 20 shots. These data were taken from Rochau et al. (2014). The peak x-ray power has a standard deviation of ∼15%. The vertical blue dashed line indicates the cutoff between peak and tail X-ray power.

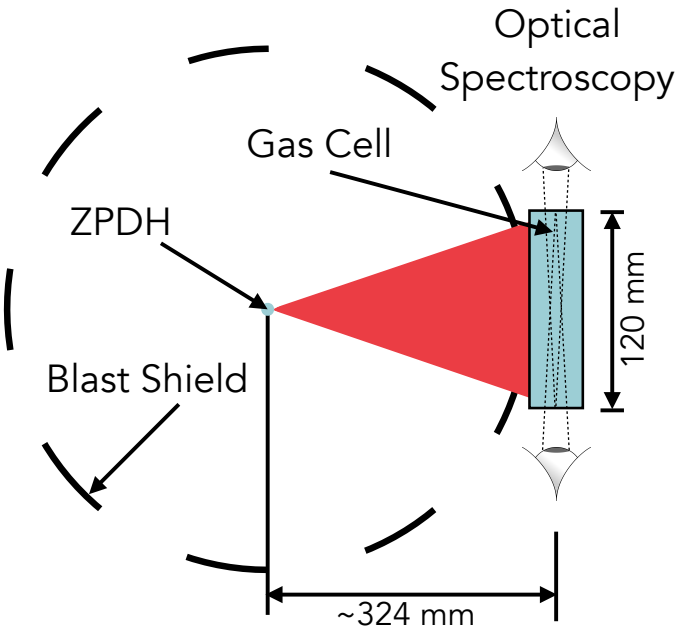

Figure 3.5: The location of the WDPE with respect to the ZPDH. Due to the large distance between the x-ray source and my experimental hardware, I can create a plasma with a length of 120 mm.

3.2 The White Dwarf Photosphere Experiment platform on *Z*

The standard WDPE gas cell is mounted ∼324 mm away from the center of the ZPDH (see Fig. 3.5 and Falcon et al. 2013, 2015b; Montgomery et al. 2015). All data discussed in Chs. 5 and 6 were collected using this mounting position. The overall basic WDPE design is shown in Fig. 3.6. In this figure, the *Z*-pinch X-rays are traveling into the plane of the page and are therefore perpendicular to the gas cell body as well as the Mylar window. Each of the identified lines-of-sight (LOS) in Fig. 3.6 is discussed below. The

buffers, which are used to protect the data collection optics from the plasma in the gas cell body (see Fig. 3.6) are discussed in Ch. 5.

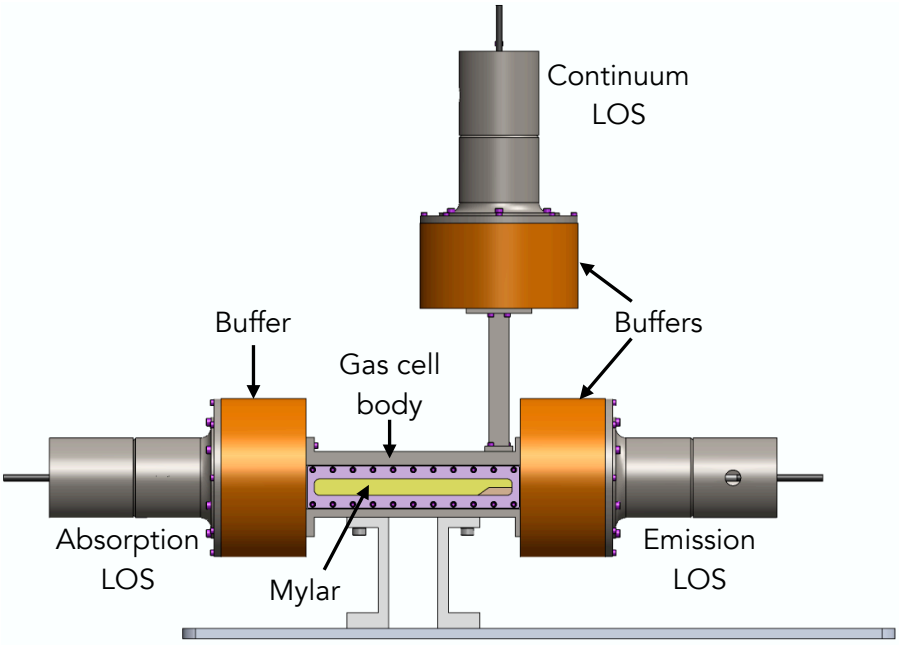

Figure 3.6: Front view of the standard WDPE gas cell used at the Z-machine, I identify major hardware components in this figure, including the Mylar window, the gas cell body, as well as all lines-of-sight. Further descriptions of these pieces of hardware are given in the text.

The interaction of the gas cell with the Z-pinch X-rays and the associated plasma formation mechanism is depicted in Fig. 3.7, which shows a side-on cross-section of the gas cell. High-energy photons (0.1 - 3 keV, blue solid in Fig. 3.7, Rochau et al. 2014) travel from the Z-pinch to the front of the WDPE gas cell, where they first traverse the Mylar window. This process removes all lower energy photons in the radiation drive. The reason

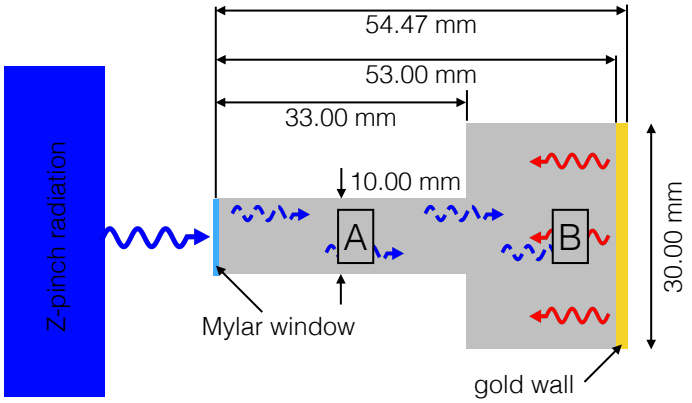

Figure 3.7: Side view of the WDPE gas cell. The shown dimensions do not vary between the inside and outside blast shield location of the WDPE. *Z*-pinch X-rays are shown as solid blue arrows, while the Mylar-filtered ones are given as dashed blue arrows. The energy re-radiated by the gold wall is shown as red arrows.

for this behavior is simple: the full IUPAC [1] name for Mylar is polyethylene terephthalate. The associated chemical chemical formula is $(C_{10}H_8O_4)_n$. Such a chemical makeup guarantees that low-energy photons whose energies correspond to maxima in the photo-excitation cross-sections of H, C, and/or O (e.g., Beswick & Glass-Maujean 1987; Lin & Ho 2010) will be filtered out. The remaining high-energy photons (dashed blue arrows in Fig. 3.7) traverse the gas almost unimpeded and deposit all of their energy into the gold back wall at the end of the cell. This energy is then re-radiated in the form of a $\sim$5 eV Planckian (red wavy arrows Fig. 3.7), which heats the gas for $\sim$200 ns (Falcon 2014). Clearly, the temperature of the gas will be determined by the amount

[1] International Union of Pure and Applied Chemistry

of energy deposited into the gold back wall, which, in turn, depends on the total Z-pinch flux arriving at the Mylar window. With the help of the view factor code VisRad (MacFarlane 2003), I can estimate the flux arriving at the gas cell. The results are shown in Fig. 3.8.

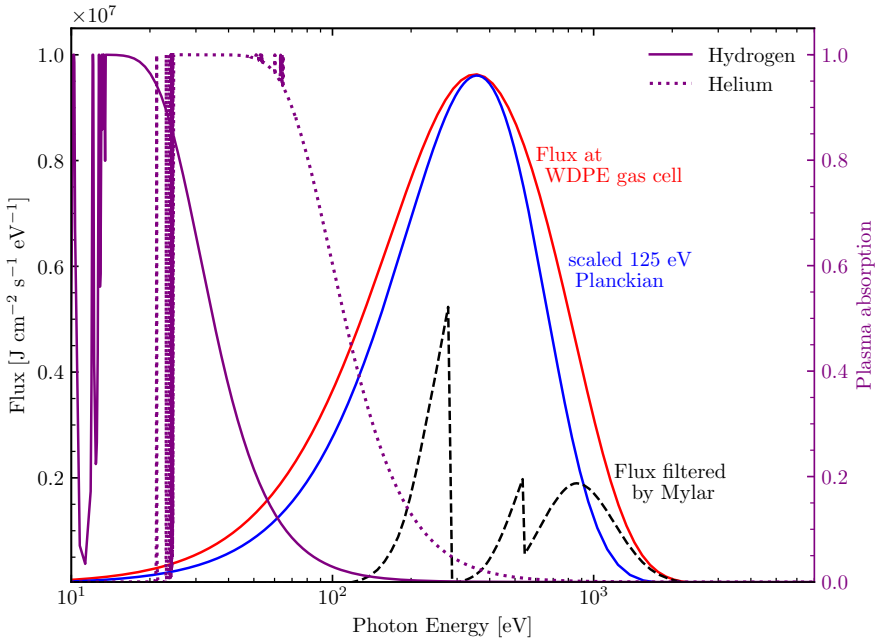

Figure 3.8: Time-averaged flux arriving at the Mylar window as a function of photon energy. I plot a 125 eV Planckian for comparison purposes. The Mylar transmitted flux is shown as a black dotted line. I also show the mean absorption of a pure hydrogen (purple) and pure helium (dashed purple) plasma.

Fig. 3.8 depicts evidence for the assertion made above that the main heating element in the WDPE gas cell is most likely the gold wall. The flux arriving at the gas cell is shown as a red curve in that figure. A 125 eV scaled Planckian is plotted in blue for comparison purposes. The Mylar filtered Z-

pinch flux is depicted as a black dotted line. This line was calculated using the cold Mylar transmission data provided by the Henke Filter transmission website[2]. The solid purple and dashed lines in that figure give the absorption of a hydrogen and helium plasma as a function of photon energy. The overlap between the Mylar curve (black dotted), which represents the flux entering the gas cell, and the two purple lines is minimal. This indicates that the heating of the plasma in my gas cell is *not* directly driven by the Z-pinch, but by the gold wall. While such an effect may seem like a disadvantage, it it allows me to precisely control the electron density (n_{e}) and electron temperature (T_{e}) of my observed plasma by varying the the distance of the data collection optics from the gold wall. The path of each LOS through the WDPE gas cell is shown in Fig. 3.9. The discussion presented in this paragraph ignores several details of the plasma formation mechanism in the WDPE gas cell. First, the Mylar window will not stay at room temperature upon interacting with the Z-pinch, making the black dotted line in Fig. 3.8 a simplified approximation. However, detailed simulations modeling the interaction of the Mylar window with the Z-pinch show that this detail does not significantly influence the plasma formation mechanism. Second, the potential plasma heating contribution of the gas cell floor/ceiling has been ignored completely. Experimental data indicates that n_{e} and T_{e} rise with decreasing distance to the gold wall (Falcon 2014), indicating that the gold wall is the dominant heating element in the WDPE gas cell.

[2]http://henke.lbl.gov/optical_constants/filter.html

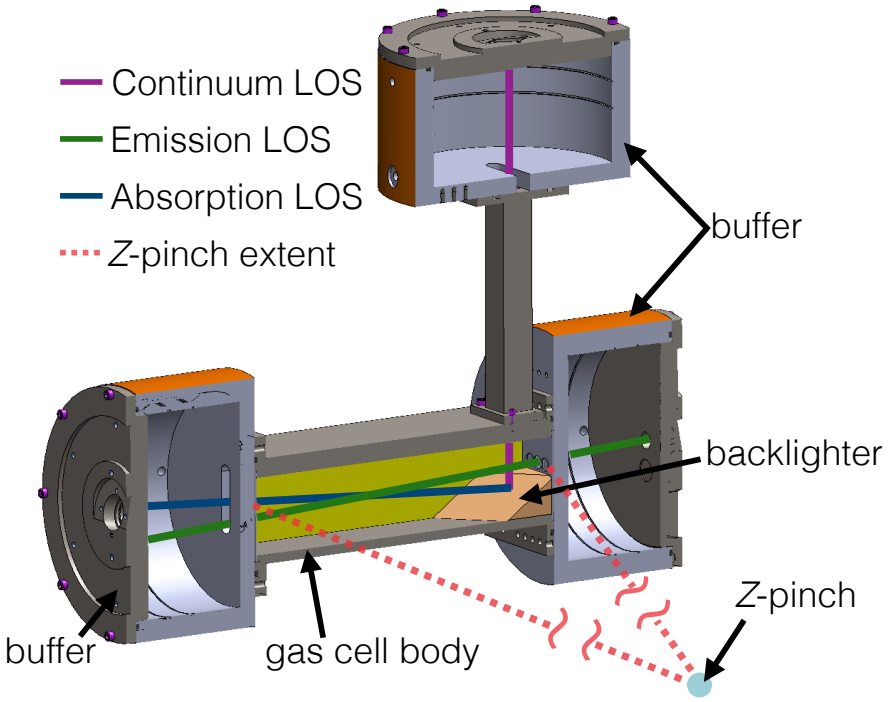

Figure 3.9: Cross-sectional view of the WDPE gas cell. I identify the location of the Z-pinch with respect to the gas cell as well as all LOS. Major components of the gas cell are identified.

As already alluded to in Fig. 3.6 and the associated discussion, the WDPE contains three lines of sight (LOS): absorption, continuum, and emission (see Fig. 3.9). Each of these LOS can be placed either 5, 10, or 15 mm away from the gold back wall. Since this piece of hardware is the dominant heating mechanism in the gas cell, the distance from the gold wall controls the observed plasma T_e and n_e. The closer the data collection optics are placed to the gold wall, the higher those two parameters will be. The absorption LOS is parallel to the gold back wall (see Fig. 3.9) and ends on the back-

lighting surface, which is also heated to ∼5 eV (Falcon 2014) by the Z-pinch. Since the maximum measured plasma temperature is ∼1.5 eV (see Ch. 6), the backlighter spectral radiance is therefore higher than the self-emission of the WDPE hydrogen plasma, resulting in an absorption spectrum recorded from this LOS. The backlighting surface gets its name from the radiation needed to produce an absorption spectrum. The continuum LOS fiber is also pointed at the backlighter but at a 90° angle to the absorption LOS. The continuum data therefore also contains absorption features. However, since this optical path integrates over a much smaller region of plasma heated by the gold wall (see Fig. 3.9), I expect the absorption features to be much weaker than those of the absorption LOS. The emission optical fiber is not pointing at any hot surface, so only photons emitted by the hydrogen plasma will be captured in this optical path. The data collected using each of these optical paths are recorded on time-resolved spectrometers. I will discuss the details of the collected absorption, continuum, and emission data in the next chapter.

Chapter 4

Reducing and Calibrating WDPE Data

In Ch. 3, I describe the fundamental aspects of the WDPE platform and how it creates plasmas through its interaction with the Z-pinch. The WDPE has the ability to collect three different datasets - absorption, continuum, and emission, all of which are collected on streaked (i.e. time-resolved) visible spectrometer (SVS) systems. The pure hydrogen data (see Ch. 5) were recorded on film only, while the hydrogen-helium datasets (see Ch. 6) were acquired on both film and CCD. This chapter discusses how I transform the raw film and CCD images to spectra that can then be used to extract scientifically meaningful data.

4.1 The WDPE data acquisition process

Before any data can be reduced, calibrated, and analyzed, it needs to be acquired first. The data collection begins at the WDPE optics assembly I show in Fig. 4.1. Photons produced by the plasma in the gas cell body traverse the buffer (see Fig. 4.1) to then enter the in-chamber fiber. The silica window in front of the collection optics serves as a hermetic seal for the gas cell while still allowing me to observe the gas cell body plasma. Ch. 6 reveals the

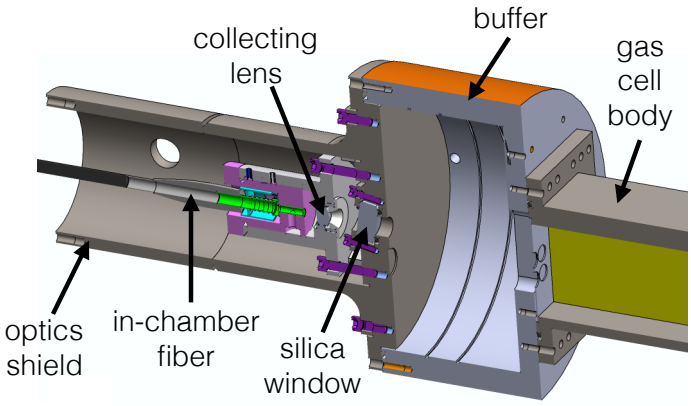

Figure 4.1: The optics assembly of the WDPE gas cell. Major hardware components are identified. This optics assembly is mounted on the buffers identified in Fig. 3.9

purpose of the collecting lens. Once at the in-chamber fiber, the photons then travel from the gas cell to the so-called feedthrough fiber. The feedthrough fiber carries the signal from the inside to the outside of the Z-machine vacuum chamber. Outside this chamber, the feedthrough fiber connects to the transit fiber, which transports the photons directly to the SVS systems. The total length of all fibers involved in delivering the photons from the gas cell to the SVS systems is ∼71.8 m (in-chamber: ∼2.1 m, feedthrough: ∼3.7 m, transit: ∼66.0 m). The current WDPE design can accommodate three different in-chamber fiber types - single 100 μm core, single 200 μm core, and a bundle consisting of a 105 μm and a 200 μm core. More details about these fibers are given later in this chapter.

Once the light has arrived at the SVS systems, the first optical apparatus encountered by the photons are the spectrometers. The entrance collection

optics at these spectrometers maximize the photon flux entering the system, while the entrance slits are set to match the core diameter of the input fibers. The film data is fed through a McPherson Model 2061 1-m $f/7$ Czerny-Turner spectrometer with a 150 g/mm (grooves per mm) McPherson grating. The dispersed light is then passed to a EG&G model L-CA-24 streak camera. Within the streak camera, the dispersed photons first interact with a photocathode, which converts the photons into electrons. These electrons are then accelerated and finally pass through a set of deflection plates. The varying voltage applied to these plates deflects the electrons as a function of time. After having been deflected by the plates, the electrons strike a piece of phosphor, which lights up as a result of its interaction with the deflected electrons. The now time-resolved phosphor photons are then captured by a Kodak T-MAX 400 film. The film-based streak cameras are also equipped with a micro-channel plate intensifier, which is usually set to 700 V for the emission data, and 400 V for the absorption data. I chose the maximum streak window for each camera: 480 ns for the emission data, and 400 ns for absorption. Finally, a comb generator, which calibrates the time resolution of the data, set at an interval of 20-ns is also exposed onto the film. The film data covers 2,000 Å in wavelength and has a resolution ($\lambda/\Delta\lambda$) of $\sim$3,000 in the vicinity of Hβ.

In the case of the CCD data, the light is first passed through a McPherson Model 207 0.67-m $f/4.7$ Czerny-Turner spectrometer with either a 300 or 600 g/mm McPherson grating. The difference between these gratings is discussed below. The CCD streak camera systems are Sydor Instruments ROSS

5100. Their temporal resolution is claimed to be 1 ps and they contain a Spectral Instruments Series 800 TE cooled CCD camera. These systems have internal comb generators that are set to 28.5 ns impulse spacing for the purposes of the WDPE data collection. The path of the photons in these CCD systems is the same as the one described above for the film systems. I collect 500 ns of data with these CCD systems for the WDPE. Depending on the grating, the CCD data can cover 800 Å with a resolution of ∼9,000 in the vicinity of Hβ (300 g/mm) or 400 Å with a resolution of ∼18,000 in the vicinity of Hβ (600 g/mm).

Now that I've given a detailed overview of how the WDPE photons travel from the gas cell to the film or CCD, I will proceed to describe how the resulting data are extracted and calibrated.

4.2 Processing the WDPE film data

4.2.1 Basic features of the film data

The vast majority of WDPE data is collected on film. As mentioned above, these spectra are collected with a 150 g/mm grating. False color raw film data for emission (usually collected on a system called SVS1) and absorption (usually collected on a system called SVS2) are shown in Fig. 4.2. The data reduction and calibration methods presented in this section will detail how I convert the data depicted in this figure to scientifically useable spectra such as the ones plotted in Fig. 4.3.

Aside from the obvious differences in captured data (emission and ab-

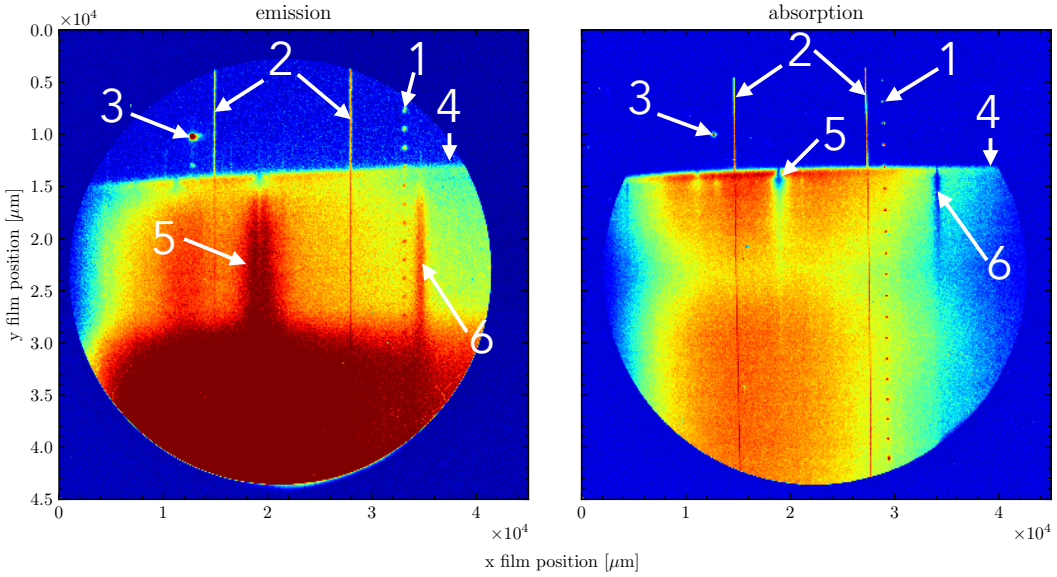

Figure 4.2: False color raw film image of the emission (left) and absorption (right) for shot z3095, a 20 Torr H/He gas fill experiment observed at 5 mm from the gold wall. The identified features are: (1) timing comb; (2) laser fiducials; (3) timing impulse; (4) onset of heating from gold wall; (5) Hβ; (6) 3d $\rightarrow$ 2p He I at 5876 Å.

sorption), the two films shown in Fig. 4.2 share many similarities. Each dataset contains a timing comb ('1' in that figure), whose impulses are spaced almost exactly 20 ns apart. These signals are used in the data reduction process to derive a time axis for the film. A wavelength axis is applied to my data using the laser fiducials at 4579 Å and 5433 Å ('2' in Fig. 4.2). More information about the lasers used in the WDPE is given in Appendix B. Both sets of film data also contain a timing impulse (3). This feature can be used to put all datasets on the same absolute time scale as the Z-machine. However, this is not necessary for the WDPE data and I therefore will not discuss this concept

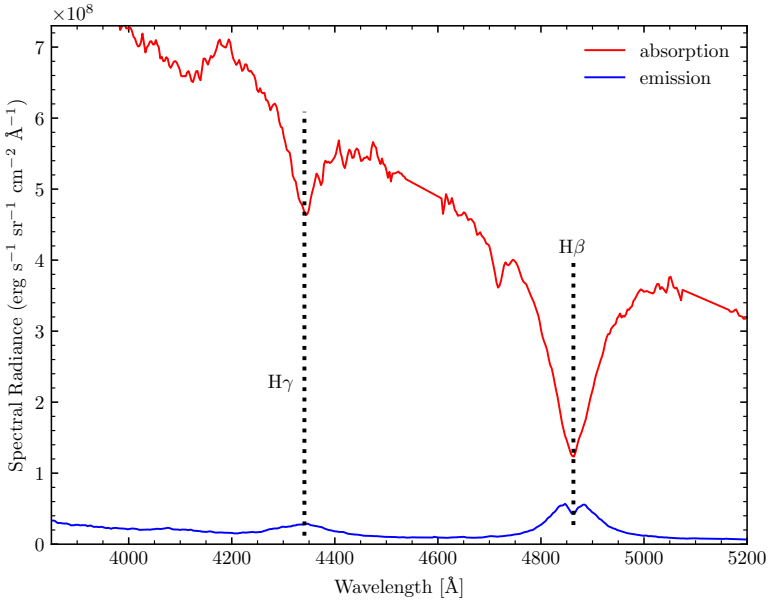

Figure 4.3: Sample absolutely calibrated film spectra that result from the data reduction and calibration methods described in this section. The locations of major spectral lines are indicated.

any further. The final trait shared by both datasets is the onset of heating from the gold back wall (4). I use this feature to define zero time in my experiment and relate all datasets to each other (see Falcon 2014 for more information). The major atomic features used in my experiments (Hβ and He I 5876 Å) are also identified in Fig. 4.2.

4.2.2 Reduction of the film data

The goal of the WDPE data reduction is to extract time-resolved spectra (Fig. 4.3) from the films shown in Fig. 4.2. SNL's PFIDL package (Mix

2007) is used for this purpose. The first step in this process is to transform the film from physical to digital format using a Perkin-Elmer microdensitometer. A NIST-calibrated step wedge then allows for the conversion of film density to radiant exposure units (erg cm^{-2}). This is the final set of units for the reduced film data.

In the next step of the reduction, small rotations introduced during the film scanning procress are accounted for by performing a linear fit to a laser line. Determining the timing comb impulse locations and fitting a 2^{nd} order polynomial to them then allows me to apply a time axis to the film data. The uncertainty of the time dispersion is determined by the standard deviation of the quadratic fit to the timing comb signals. In some instances, the film comb signal is corrupted. I thus developed an alternative time dispersion derivation methodology. Each SVS system has their own distinct timing comb signatures, as shown in Figs. 4.4 and 4.5. Due to their reproducibility, these respective combs can and have been used as substitutes for any comb data that may be compromised on either SVS film.

Once the images has been time resolved, I apply a wavelength axis to the data. Combining the location of the laser lines (see Fig. 4.2) on the film with their respective wavelengths allows for an easy calculation of a linear dispersion for the film data. While a linear dispersion is most certainly not the most accurate approach ($\sigma_\lambda \approx 1.5$ Å), it is sufficient for the purposes of the film data reduction and the scientific goals of the WDPE.

The now time- and wavelength resolved film data is integrated in 10 ns

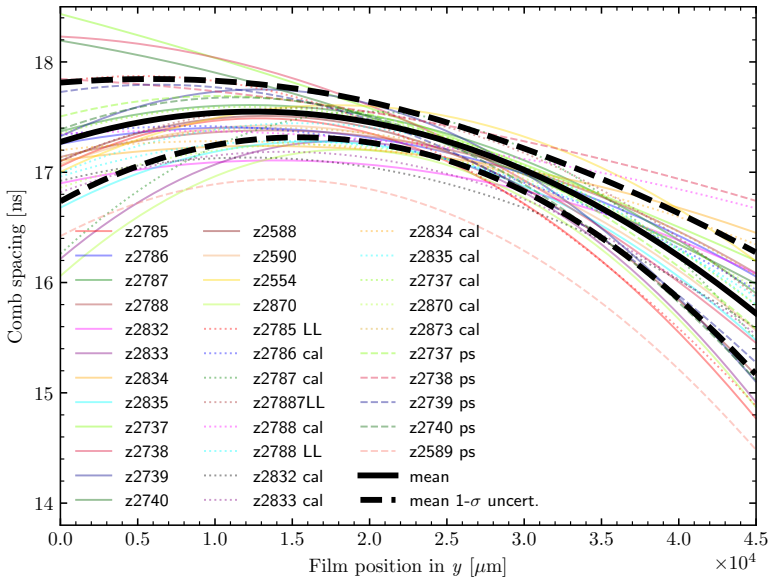

Figure 4.4: Average second order polynomial fits of 29 combs retrieved from shots spanning nearly 2 years for SVS1. The black solid line indicates the average of the complete set, while the dashed black line gives the uncertainty of the average. This solid black line is used as a replacement for compromised timing combs.

intervals during the final step of the WDPE data reduction process. Such integrations mainly serve to increase the signal to noise of the data. I also extract the widths of both laser lines during this process. This allows for the determination of the instrumental broadening, a crucial ingredient for the line fitting algorithm I apply at a much later stage of the data analysis. Since I collect over 2000 Å of spectral data, the delay caused by the transit through the fiber of blue and red photons is also accounted for. Once all the above

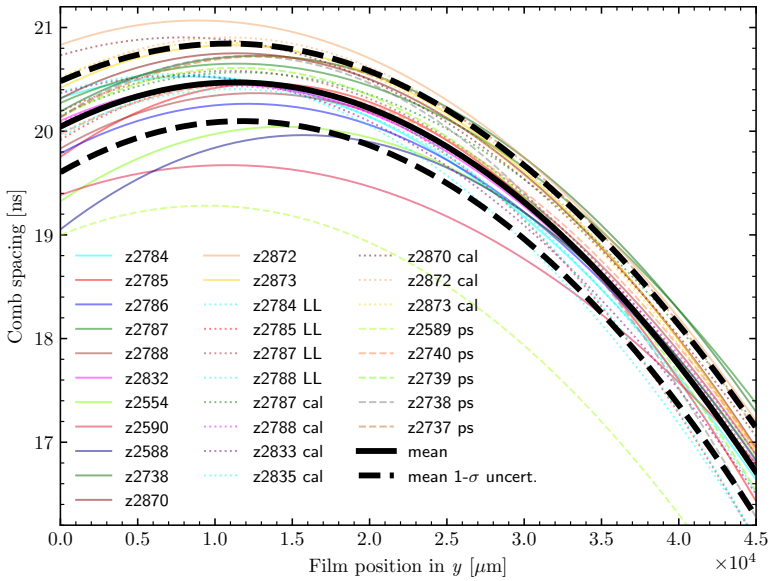

Figure 4.5: Average second order polynomial fits of 29 combs retrieved from shots spanning nearly 2 years for SVS2. The black solid line indicates the average of the complete set, while the dashed black line gives the uncertainty of the average. This solid black line is used as a replacement for compromised timing combs.

steps have been completed, the film data reduction is complete.

4.2.3 Optical components calibration

The experimental spectra are in radiant exposure units (erg cm^{-2}) at the end of the data reduction process. These units are not sufficient to achieve the scientific goals of the hydrogen experiments, which require the ability to directly compare absorption and emission spectra. A conversion to absolute

spectral radiance (erg s^{-1} sr^{-1} cm^{-2} $Å^{-1}$) is thus needed.

This conversion process, called the data calibration, relies on many different inputs. Some of them are derived from the characterization of the optical components used to collect the data, while others are obtained from the data itself. These calibration elements are discussed separately below beginning with the optical components. I have never made extensive use of the data calibration methods I present in this chapter since the scientific goals of my experiments shifted. However, I invested significant amounts of time and energy into developing and automating the software needed for the WDPE data calibration. Anyone in need of their own data calibration methods can use the following descriptions as a starting point.

The optical components used to collect the WDPE data (see Fig. 4.1) are re-used many times. Their calibration data is therefore not tied to individual experiments and can thus be processed separately. I use the laser-driven light source (LDLS) to calibrate all WDPE optical components. The LDLS allows for the derivation of the SVS system response, measurement of data collection solid angles, and fiber transmission values. Its spectral shape is highly reproducible, making it the ideal instrument for calibration purposes. A detailed description of the LDLS shape measurement is given in App. D. The resulting LDLS shapes, measured several times over the course of a year, are shown in Fig. 4.6.

Absolute spectral radiance units contain a solid angle component. The determination of this parameter for the WDPE optical assemblies (see Fig. 4.1)

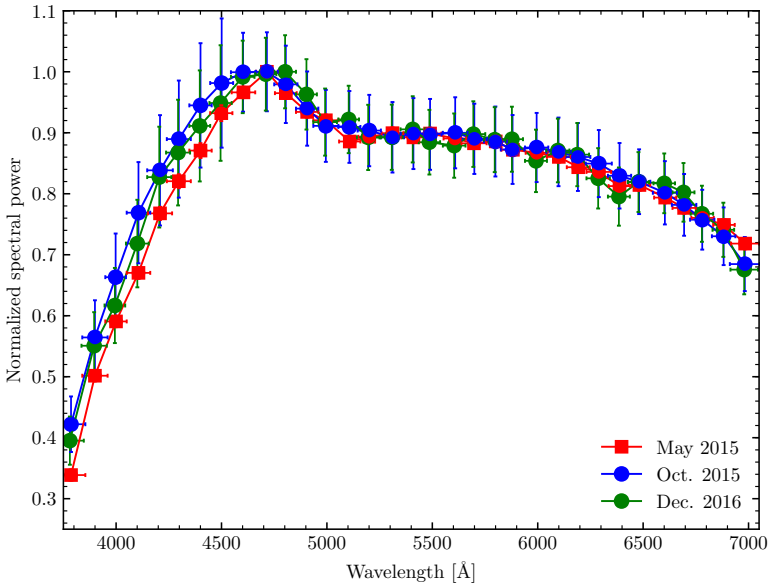

Figure 4.6: Measured LDLS shape used for spectral response determination. Over the course of a year, the shape of this calibration instrument did not change significantly. This is therefore one of most solid aspects of this calibration process.

is thus a crucial component of the data calibration process. I derive required solid angle values from collection-beam diameter and profile measurements, which are performed using a Thorlabs BC-106 VIS beam profiler. To characterize the beam profile and diameter along the optical path of any LOS through the gas cell, I perform beam profile measurements 40 mm, 90 mm, 140 mm, 200 mm, and 240 mm from the end of the optics assembly. An automated analysis routine developed by me then converts these beam profile measurements to beam diameters. The first step in the automated beam profile processing

code is to determine the edges of the beam in the 2D data supplied by the Thorlabs instrument. Once the edge has been found, an ellipse is fit to the outer limits of the beam profile. The ellipse-fitting procedure ensures that the beam profile measurement is not influenced by any reflections in the data. In a measurement that is not influenced by reflections, the eccentricity of the fit ellipse is smaller than 0.02. My automated routine then locates the widest point of the fit ellipse. I define cross section of this widest point to be the beam profile.

Next, I rotate the now extracted beam profile about its center by 180 degrees to find the uncertainties in the measurement. This uncertainty derivation makes the implicit assumption that the beam profile is circular, but as I mentioned above, this assumption is valid given that a usual beam profile measurement is circular to within 2%. My automated routine then finds the beam diameter by integrating the entirety of the beam profile and finding the points in the data at which the integral between those bounds is equal to 99.73% (or 3σ) of the total area. The difference between these points is defined to be the beam diameter. A collection beam area is now easily calculated.

The final step in the optical components calibration procedure calculates solid angles from the above beam diameter and area measurements. A routine devised by Guillaume Loisel solely for the WDPE models the collecting lens used in the WDPE optical setup (see Fig. 4.1) and computes the solid angle this hardware component can view. During this calculation, the geometry of the gas cell with respect to the optical fiber I use to capture my

data is taken into account. In combination with the beam profile and area data processed earlier, I then derive the 'effective', 'on-axis' and 'off-axis' solid angle. The 'on-axis' and 'off-axis' angles are determined by the maximum and minimum viewing angles that can be accepted by the collecting lens, while the 'effective' solid angle represents a mean of the 'on' and 'off' axis angles. The results of this calibration step are shown in Fig. 4.7. In this calculation, it is assumed that all rays propagate through the fiber with the same efficiency and that other potential non-ideal effects (e.g., fiber numerical aperture) do not influence the solid angle calculation. Tests have shown that the final calibrated data are relatively insensitive to changes in the assumed collection solid angle.

4.2.4 Film data calibration

In the previous section, I describe the WDPE optical components calibration. This section will contain a description of the experimental data calibration methods. All measurements presented and discussed here are acquired on experiment day and are only applicable to the corresponding dataset.

The first step of the data calibration process consists of extracting the LDLS shape as captured by the so-called calibration film, which is collected immediately after an experiment. The LDLS film shape is determined using an automated routine I developed. Differentiating between film background and the LDLS data is the most important aspect of this process. The Kodak T-MAX 400 film cartridge used for data collection purposes has a size of 45 mm x 45 mm, while the data, which is captured in the shape of a circle, has a

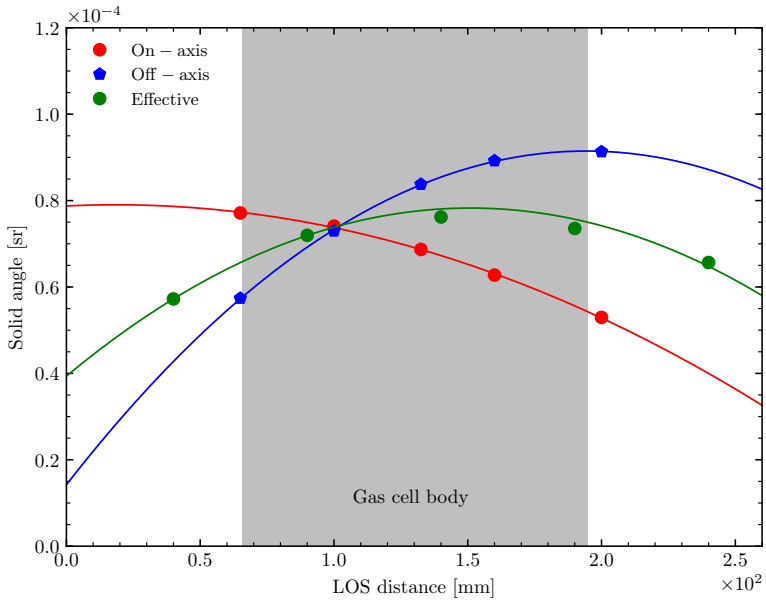

Figure 4.7: Representative solid angle measurements for one of the fibers used in the WDPE. I identify the gas cell extent as well as the 'on-axis', 'off-axis', and 'effective' solid angles.

diameter 41 mm and is centered on the square film. To find the edges of the data, each row of film data is processed individually in steps of 10 pixels starting at the very edge of the film. A mean spectral radiance value over these 10 pixels is calculated and then compared to the average of the next 10 pixels. If the mean pixel values agree for the neighboring slice of pixels, the routine knows that the data portion of the film has not been reached yet. Once the mean pixel values of the sequential groups do *not* agree, there are two options: the routine has encountered a hot spot on the film or it has found the edges of the data. To differentiate between these two possibilities,

the automated routine compares the mean radiance values of the errant pixel group to subsequent groups. If subsequent groups match the mean values of the delinquent slice, the routine has found the edge of the data for that particular pixel row. If the increase in mean pixel value is contained to that group of pixels only, the edges of the data have not been found yet. This process is repeated for all pixel rows in the y-direction of the film.

Once all limits have been found, my automated routine time-averages data contained within these bounds. This results in a single LDLS spectrum. Before the shape of the LDLS on the film can be determined, laser lines and timing combs that are also captured on the calibration film have to be removed. This is achieved by locating the peaks of these features in the final LDLS spectrum and removing them. A representative shape of the LDLS on the absorption and emission cameras can be seen in Fig. 4.8.

Relating the radiant exposure to the absolute power on the film is the next step in the data calibration procedure. The laser lines used during the reduction procedure to apply a wavelength axis to the film also serve as power fiducials for the experimental data. Since the film is currently in the units of ergs cm^{-2}, an integral over the laser line (which is in units of cm^2) at each time step results in the total energy of the laser line on the film. Using the ratio of that energy to the laser input energy (which is recorded at shot time using a Ophir Nova II laser power meter), my automated routines derive an absolute scaling factor for each time step and each laser (green and blue) on the shot as well as calibration film. Since the laser powers between the shot

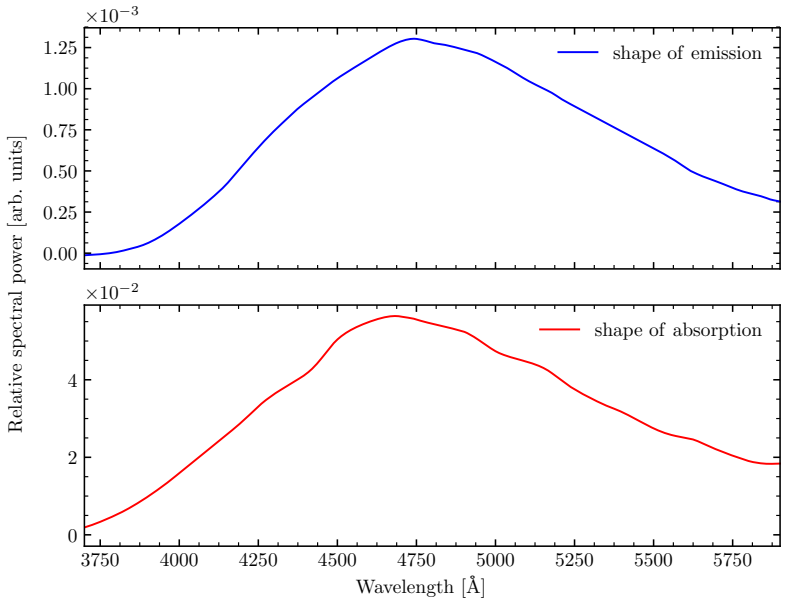

Figure 4.8: Representative shape of the LDS as captured on the absorption and emission cameras used for the WDPE.

and calibrations films do not vary, I should derive the same scaling factors for each of them. Unfortunately, that is rarely ever the case. The precise reason for this behavior is still unknown, but potential explanations include short-term laser power fluctuations or incomplete mode-filling in the fibers used to transport the laser light to the spectrometers. Due to this effect, I consider this portion of the calibration procedure to be the least reliable. However, it is also amongst the most important.

The final step in the data calibration accounts for the signal attenuation caused by the ∼71.8 m transit, feedthrough, and in-chamber fibers I use to

transport the signal from the WDPE gas cell to the SVS systems. To determine the total loss of signal caused by all these fibers, I measure the LDLS flux as a function of wavelength directly at the source using a StellarNet BlackComet spectrometer. The LDLS signal is then passed through the entirety of the fiber path, including the WDPE data collection optics (see Fig. 4.1), which is removed from the buffer during this process. The collecting lens and window are included in this measurement. I then record the resulting flux as a function of wavelength again using the StellarNet spectrometer. Dividing these two flux datasets then allows for the calculation of a transmission as a function of wavelength for the WDPE optical fiber system. In the region of interest ($\sim$4000 Å – $\sim$6000 Å), I derive a transmission of roughly 6% (or a signal loss of 94%). See Fig. 4.9 for a typical transmission curve of a complete WDPE fiber path.

As evident from Fig. 4.9, the transmission drops off severely at lower wavelengths. This effect is caused mainly by the chemical makeup of the fiber, which in WDPE case is high-OH (hydroxyl) silica. This fiber makeup has a high pulsed radiation resistance making it ideal for pulsed power applications (e.g., Lyons & Looney 1993). The large drops in transmission observed at $\sim$6000 Å and $\sim$7100 Å are caused by the high OH content of the fiber. The part number for the standard 100-μm fiber is molex FVP100110125, while those for the bundle are Thorlabs FG105UCS (105-μm core) and Thorlabs FG200UEA (200-μm core).

At this point in the data calibration procedure, all results from previous

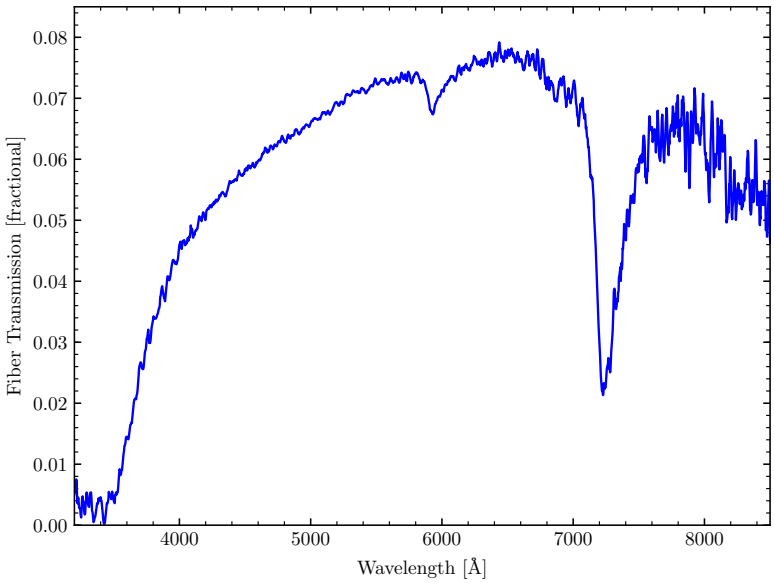

Figure 4.9: Representative fiber transmission as a function of wavelength for the WDPE. The transmission drops off severely at lower wavelengths due to the makeup of the fibers, which in this case are pure silica core fibers with a flourine-doped silica clad around them.

calibration steps are combined to derive an absolute spectral response (defined as $1/\eta$, with η being the efficiency). First, I divide the data shown in Fig. 4.8 by the data shown in Fig. 4.6. This results in the relative spectral response for both the absorption and emission film camera systems. The absolute spectral response is then merely the relative spectral response multiplied by the absolute scaling factors derived earlier. Fig. 4.10 shows a representative absolute spectral response for the emission and absorption systems.

All calibration data needed to convert the absorption and emission spec-

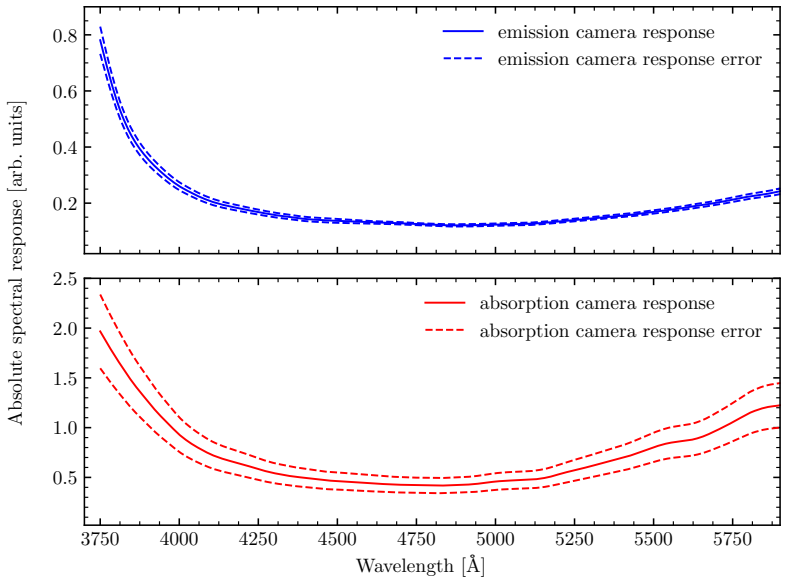

Figure 4.10: Representative absolute spectral responses for the emission (blue) and absorption (red) camera systems.

tra from radiant exposure (erg cm^{-2}) to absolute spectral radiance (erg s^{-1} sr^{-1} cm^{-2} $Å^{-1}$) have been derived. The reduced film data is now multiplied by the absolute spectral response plotted in Fig. 4.10 and subsequently divided by the fiber transmission calibration measurements shown in Fig. 4.9. The resulting spectra are then divided by the collection beam area and the associated solid angle. Finally, the entire dataset is multiplied by 10^9 to convert W to erg/s. The absorption and emission spectra obtained from this procedure are shown in Fig. 4.11.

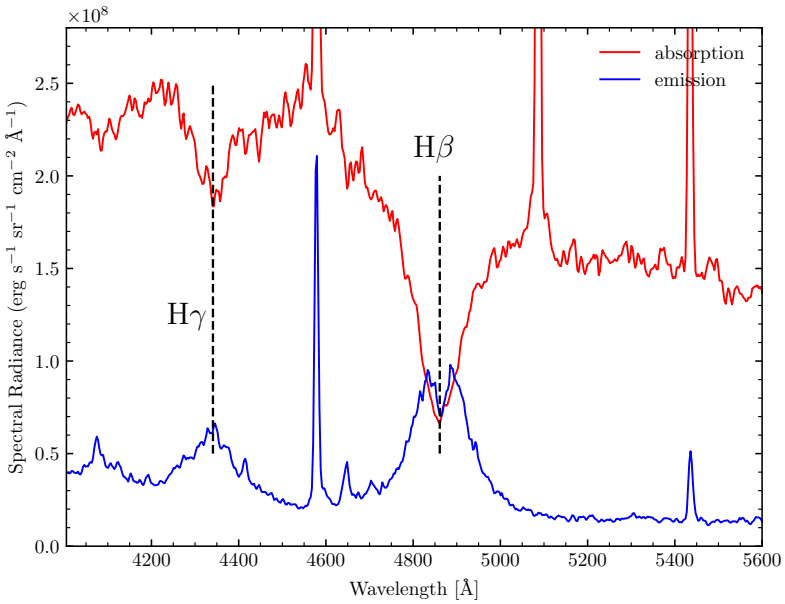

Figure 4.11: Calibrated absorption and emission spectra resulting from the procedures outlined in this section. This data was collected during shot z2832, a pure H shot performed in October 2015. The estimated n_e of the depicted dataset is $\sim 5 \times 10^{17} \mathrm{cm}^{-3}$.

4.2.5 Extracting transmission line profiles

The absorption and emission spectra shown in Fig. 4.11 have all calibration data applied to them. The errors in the radiance of the plotted spectra can be as high as 20%. To extract transmission spectra from my experimental data, I need to correct the absorption spectra for plasma self-emission. This goal can only be achieved if absorption and emission are on an absolute scale. A potential additional scaling factor between the absorption and emission data, which could arise from differences in fiber coupling or spectrometer

systems used to observe the absorption and emission datasets, must therefore be derived. I note here that the above subtraction procedure is required for the WDPE since the backlighter in my platform is not strong enough to overcome self-emission effects.

In the WDPE, the final scaling factor is derived using the continuum LOS. A look back at Fig. 3.9 reveals that both the absorption and continuum LOS observe the same surface on the gold backlighter. Therefore, in an experiment where absorption and continuum LOS data are collected simultaneously, the continuum regions in those two datasets should be at the *exact same* absolute spectral radiance. The needed absorption and continuum data are collected in so-called calibration shots, during which the continuum dataset is captured on the same camera/spectrometer as the emission data, while the absorption dataset is acquired on its usual system. The continuum data is calibrated using the exact same methods as the absorption and emission data. Comparing the continuum regions of the absorption and continuum data therefore allows me to derive the final potential relative scaling factor between the two camera systems. This scaling factor is then applied to the emission spectra before it is subtracted from the absorption data.

To go from the now emission-corrected absorption data to transmission spectra, I simply define a linear continuum across the features of interest (Falcon 2014). Representative experimental transmission line-shapes resulting from this process as well as theoretical fits to them are plotted as black and red respectively in Fig. 4.12. It is precisely this final dataset that is then used

to perform fits to the hydrogen line-shape calculations used in WD astronomy to infer stellar masses.

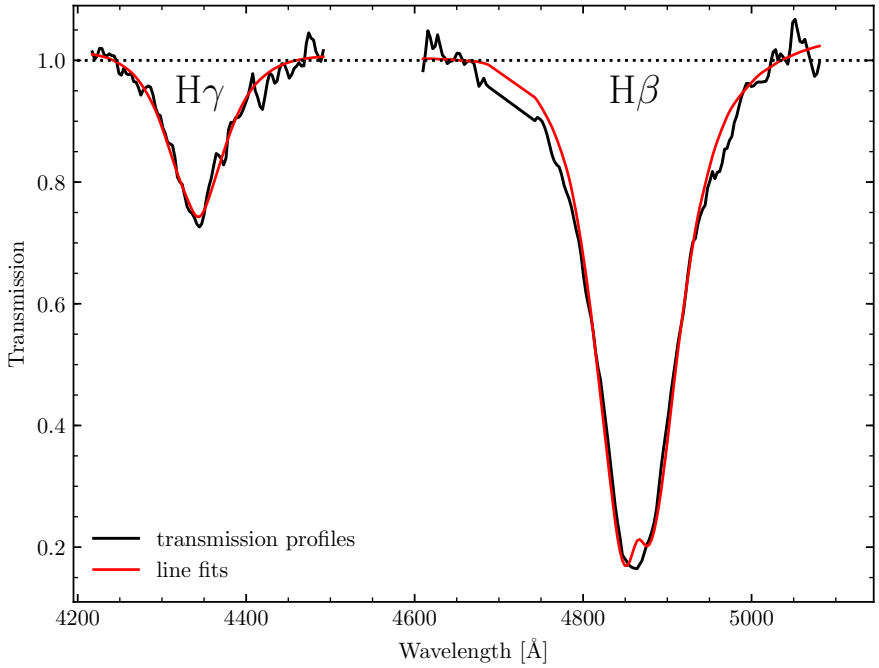

Figure 4.12: The final result of the calibration procedures of the WDPE. I show the experimental line-profiles (black) as well as theoretical fits (red) to the line profiles. These fits enable me to extract an n_e from the plasma.

4.3 Processing the WDPE CCD data

The WDPE CCD data is processed using a combination of SNL's SMASH library (Dolan et al. 2016) and routines developed by me. Since the CCD data is captured in digital format, no microdensitometer conversion step is needed. I show raw CCD images for emission and absorption collected

with a low-resolution (300 g/mm) and high-resolution (600 g/mm) grating in Figs. 4.13 and 4.14 respectively. The CCD datasets share many similarities with the film, except for the absence of the laser fiducials, which are captured in a separate image. See Fig. 4.15 for a sample CCD laser image. The laser wavelengths shown in that figure are: 5435 Å ('1'), 5946 Å ('2'), 6046 Å ('3'), and 6118 Å ('4', see App. B for more information). Unlike the film data, the CCD registers increasing wavelength in the downward y-direction and increasing time in the rightward x-direction. The multiplicity of comb signals ('5') shown in Fig. 4.15 is caused by the co-addition of the individual laser images. The extra emission in the center of the image ('6') is a spurious optical effect that can occur during the collection of the laser fiducials.

The first step of the CCD reduction procedure consists of applying a distortion correction to the data and fiducial images. Distortions in the CCD data are caused by the ramp voltage applied to the two electron deflection plates at the end of photocathode (see Sec. 4.1). SMASH's distort routine allows for the derivation of a distortion correction grid for the CCD images that can be applied to both the data and laser images. I generally reduce and analyze the data using both the distortion corrected and uncorrected approach. Shift measurements show that this does not affect the final results in any significant fashion. A more detailed treatment of this is given in Ch. 6.

Regardless of whether a distortion correction was applied to the data or not, the next step in the reduction procedure is to apply a time axis to the CCD image. Much like with the film data, this consists of determining the

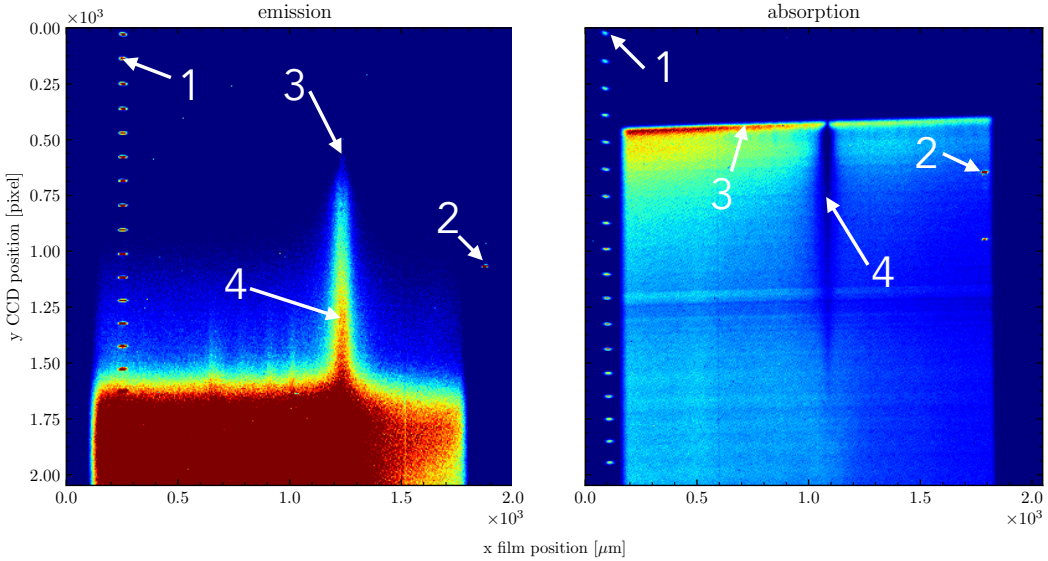

Figure 4.13: Raw low-resolution (300 g/mm) emission (left) and absorption (right) CCD images for shot z3195. The identified features are: (1) timing comb; (2) timing impulse; (3) onset of heating from gold wall; (4) 3d $\rightarrow$ 2p He I at 5876 Å. Dark red regions in the figure indicate high photons counts, while dark blue regions indicate low photon counts. The feature located at y-coordinate of $\sim 1.25 \times 10^3$ in the absorption image (left) is a streak tube artifact. My data analysis ends well before the occurrence of this feature and therefore does not represent any challenges.

location of the timing impulses, which are now 28.5 ns apart, and fitting a 2^{nd} order polynomial to determine the time dispersion as a function of pixel position on the CCD. This dispersion is applied to the laser as well as the data images. The fiducial and data images are then put on the same time scale by determining the onset of heating from the gold back wall (feature 3 in Figs. 4.13 and 4.14, compare Sec. 4.2.2).

The penultimate step in the CCD reduction process is the wavelength

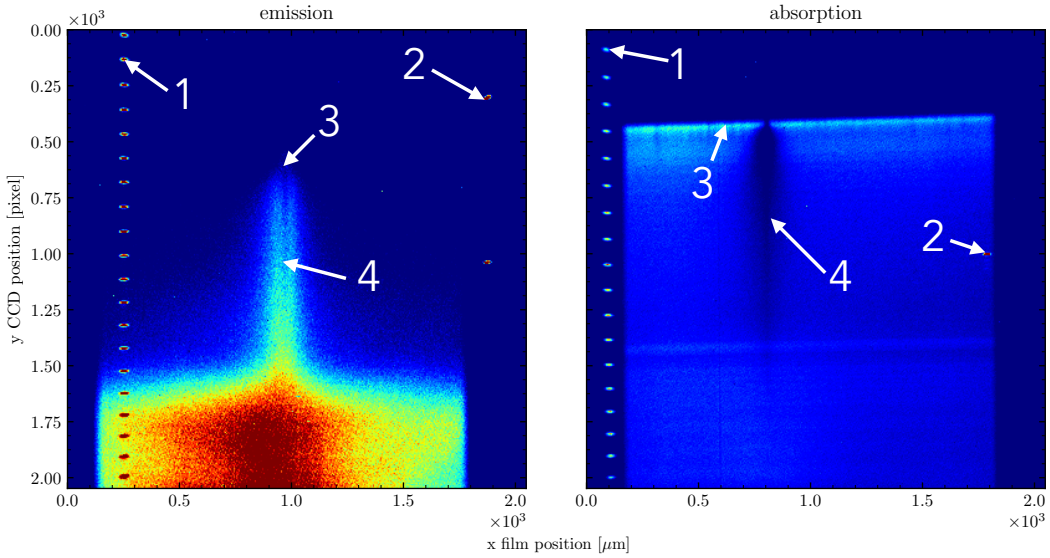

Figure 4.14: Raw low-resolution (600 g/mm) emission (left) and absorption (right) CCD images for shot z3095. The identified features are: (1) timing comb; (2) timing impulse; (3) onset of heating from gold wall; (4) 3d $\rightarrow$ 2p He I at 5876 Å. Dark red regions in the figure indicate high photons counts, while dark blue regions indicate low photon counts. The feature located at y-coordinate of $\sim 1.25 \times 10^3$ in the absorption image (left) is a streak tube artifact. My data analysis ends well before the occurrence of this feature and therefore does not represent any challenges.

calibration of the data. Since these images will be used for Stark shift measurements of helium, it is preferable to use as many wavelength fiducials as possible. A Hg-Ne calibration lamp will produce 13 wavelength features in the spectral range of the CCD data shown in Fig. 4.13. Unfortunately, the lamp lines are much weaker than the experimental data and thus need to be collected at a much lower (8 s) sweep speed. The ramp voltage applied to the electron deflection plates (see Sec. 4.1) therefore differs from that of the 500 ns

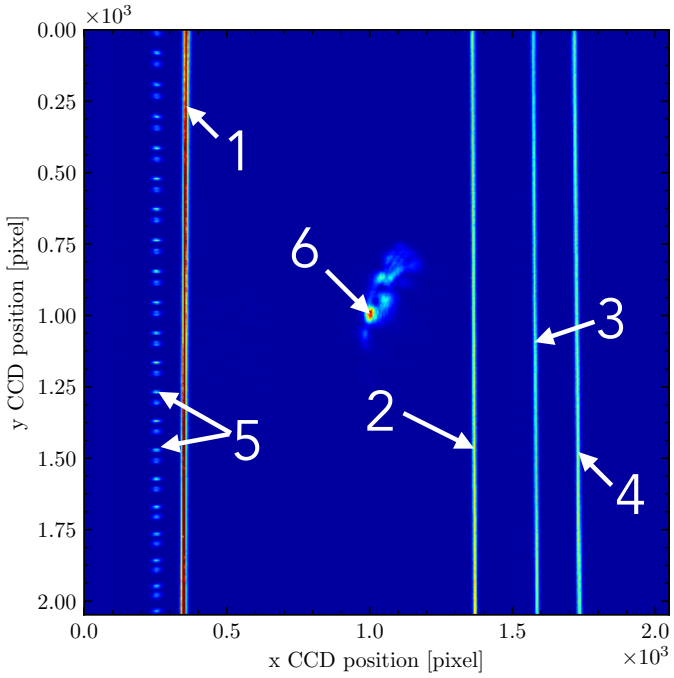

Figure 4.15: Sample image of laser lines used for wavelength calibration purposes. The identified features are: (1) laser at 5435 Å; (2) laser at 5946 Å; (3) laser at 6046 Å; (4) laser at 6118 Å; (5) comb signals resulting from co-added fiducial images; (6) spurious optical effect.

sweep speed used for the experimental data. This is *not* the case for the laser lines, which can be acquired at the same sweep speed as the experimental data. However, the lasers are available at a limited number of wavelengths. The instrumental distortions as well as the wavelength dispersion are dependent on the chosen data collection time duration. Thus, the wavelength dispersion derived from the lamp images cannot be applied to the experimental data (see App. C). As demonstrated in Ch. 6, the lamp images serve as an important validation for the wavelength dispersion derivation technique. Given all these

considerations, I am thus left with the laser lines shown in Fig. 4.15 as my wavelength calibration features.

The most precise approach to wavelength-calibrating the CCD data is to extract each individual pixel row and fit a Gaussian profile with a linear background to each of the four laser lines. This approach has two advantages: it allows me to detect a precise inter-pixel peak location of the laser line and it also gives me the opportunity to determine its error. Tests have revealed a slight dependence of the derived peak location error on the number of fitted points. These trends, however, are not significant. From the location of the Gaussian centers, I then derive a 2^{nd} order wavelength dispersion across the entirety of the CCD. This fit results in the second error contribution to the wavelength dispersion. The third and final error contribution is derived from the difference in actual laser wavelength and that resulting from the derived wavelength dispersion. Once this process has been completed for all pixel rows in the image, the wavelength calibration has been completed. A much more detailed discussion of this process is presented in Ch. 6.

In the last step of the CCD data reduction, I apply the same refraction correction which accounts for the difference in photon arrival times to my data. However, since I only collect, at most, 800 Å of data, the effects are minimal. Finally, the data are integrated over 20 ns to give the final spectra, which are then used to perform the He shift measurements. Please see Ch. 6 for more details.

Chapter 5

An Exploration of Gradients in the WDPE Platform

All preceding chapters have dealt with the scientific motivations, the basic physics of the platform, as well as the data reduction and calibration methods for my experiments at SNL's Z-machine. With all of that in mind, I will now finally present some real science. In particular, I will explore an issue that has plagued the WDPE and WD observations for many years: the disagreement in inferred n_e from different members of the hydrogen Balmer series.

5.1 Extracting White Dwarf parameters using the spectroscopic method

In Sec. 2.1.1, I describe the basic reasoning behind the spectroscopic atmospheric parameter extraction approach. To understand all details of the investigation I present in this chapter, further background on this method is needed. It is generally the hydrogen Balmer series that are used in the spectroscopic method to infer stellar masses. These features are found in the optical regime of WD spectra. The defining characteristic of the hydrogen Balmer series is their shared n=2 lower state. The first few transitions in this

series have specific names associated with them. I list the most commonly used lines and their associated energy levels in Table 5.1. Lines shown in blue are the focal point of the WDPE as well as all the investigations presented in this chapter.

Table 5.1: Hydrogen Balmer lines used to infer WD masses

Feature name	**Feature wavelength** [Å]	**lower energy level [eV]**	**higher energy level [eV]**
Hα	6564.54	10.199	12.088
Hβ	4861.36	10.199	12.749
Hγ	4340.43	10.199	13.055
Hδ	4101.74	10.199	13.221
Hϵ	3970.07	10.199	13.321
Hζ (H8)	3889.05	10.199	13.386
Hη (H9)	3835.38	10.199	13.431

Within the framework of the spectroscopic method, there are two approaches to extracting WD atmospheric parameters. The first, and less common technique, fits a complete model atmosphere calculation to an entire WD observation, both of which are on an absolutely calibrated flux scale (e.g. Koester et al. 2014). The second, and much more prevalent procedure, consists of extracting and fitting individual line profiles. The first step in this procedure consists of again fitting a complete model atmosphere calculation to the entirety of a flux-calibrated WD spectrum. To account for any flux-calibration uncertainties in the continuum regions of the data, a polynomial of some order (I've been told it can range from 2 to 12, Pierre-Emmanuel Tremblay, priv.

comm., June 2016) is superimposed on the model atmosphere. After this initial fit has been completed, the individual lines as well as the model atmosphere calculations are normalized at a set and constant distance from line-center. The fits to extract the WD atmospheric parameters are then repeated with these normalized line profiles (e.g. Liebert et al. 2005). I've invested many months into exploring this latter method of fitting WD spectra. My findings are given in App. A. Different studies have tried to estimate the effects of the two different spectroscopic method approaches, with the most complete account given by Fuchs (2017). I will not focus on the potential difference in these approaches here, but rather explore an effect which has been known about since the early 1990s and was thought to be fixed by Bergeron (1993). The proposed solution to this effect involves altering the so-called critical microfield ($\beta_{\rm crit}$). This critical microfield parameter results from the theoretical treatment of the Stark effect, which explains the shifting and broadening of spectral lines as a function of the plasma electric field. In the case of WDs, this electric field is caused by free electrons and protons in the atmosphere. Applying an electric field to the hydrogen atoms in the WD atmosphere splits the degenerate atomic energy levels. As the electric field increases, so does the splitting of the levels. Eventually, the highest energy Stark-split levels of energy level n will be higher in energy than the lowest Stark-split levels of energy level $n+1$. Once the levels have crossed, it is generally assumed that the lower energy level dissolves and all electrons in that state will be ionized. The associated spectral line will therefore disappear. The precise electric microfield

value at which this happens is called the critical microfield, or $\beta_{\rm crit}$.

Bergeron et al. (1992), who first introduced the spectroscopic mass determination method to the astrophysical community, discovered that as higher-order Balmer lines were included in the commonly-used line normalization fitting routine, the inferred $T_{\rm eff}$ and log g of the WD under consideration began to decrease. Bergeron (1993) found that this problem is caused by non-ideal equation of state effects neglected in the Vidal et al. (1973) line profile theory used by Bergeron et al. (1992). The solution proposed by Bergeron (1993) arbitrarily increased $\beta_{\rm crit}$ by a factor of two to account for these non-ideal effects. This appeared to partly solve the problem (see middle panel of Fig. 2 in Tremblay & Bergeron 2009). However, this is an unsubstantiated ad-hoc solution: no experiments or theoretical models motivate such a multiplication. Since the spectroscopic method proposed by Bergeron et al. (1992) relies on fitting individual line profiles, it is no surprise that such effects were not discovered before 1992, since all past and current hydrogen line-profile theories applicable to WDs have been calculated and validated in emission, mainly using the benchmark experiments of Wiese et al. (1972). In these emission comparisons, differences between various Balmer lines are *not* observed (Wiese et al. 1972; Tremblay & Bergeron 2009; Montgomery et al. 2015). WD observations, however, are performed in absorption. In nearly all areas of astronomy and plasma physics, the principal of complete redistribution is assumed to ensure equality between emission and absorption line profiles (e.g., Hubeny & Mihalas 2014). If so, the community should be able to apply emission-validated line-profile

theories to absorption spectra and still recover an accurate n_e value. The trends observed in WDs then lead to the following questions: (1) are the n_e and T_e trends observed in WDs caused by unknown gradients in the atmosphere of the star? or (2) is there a fundamental flaw in the assumption of equivalence between absorption and emission line profiles? As described in Chs. 3 and 4, the WDPE collects absorption and emission data of the same plasma at the same time. This experimental plasma is expected to be significantly more uniform than that found in a WD atmosphere (see Fig. 3.1). The combination of these aspects puts me in an ideal position to probe the apparent n_e trends resulting from fits to WD spectra and potentially understand their physical origins. Any such investigation has to begin with the effects of gradients on emergent line profiles. The analysis presented in this chapter explores plasma inhomogeneities in the WDPE platform.

5.2 Dimensions of the gas cell body

In Fig. 5.1, I show a schematic cross-section of the WDPE gas cell in the horizontal direction (compare Fig. 3.9). Major distances and angles are identified. The LOS locations identified in that figure are 10 mm from the gold wall, the standard WDPE data collection distance. The two radiation-guiding apertures located between the Z-pinch and the WDPE platform are designed such that the X-ray flux arriving at my gas cell overfills the Mylar window. Using Helios (MacFarlane et al. 2006), I modeled the expansion of these radiation-guiding apertures into the X-ray path upon the interaction

with Z-pinch energy flux and found it to be negligible. This design choice ensures the highest degree of uniformity in plasma heating and makes the total X-ray flux into the gas cell insensitive to small variations in the location of the WDPE with respect to the Z-pinch.

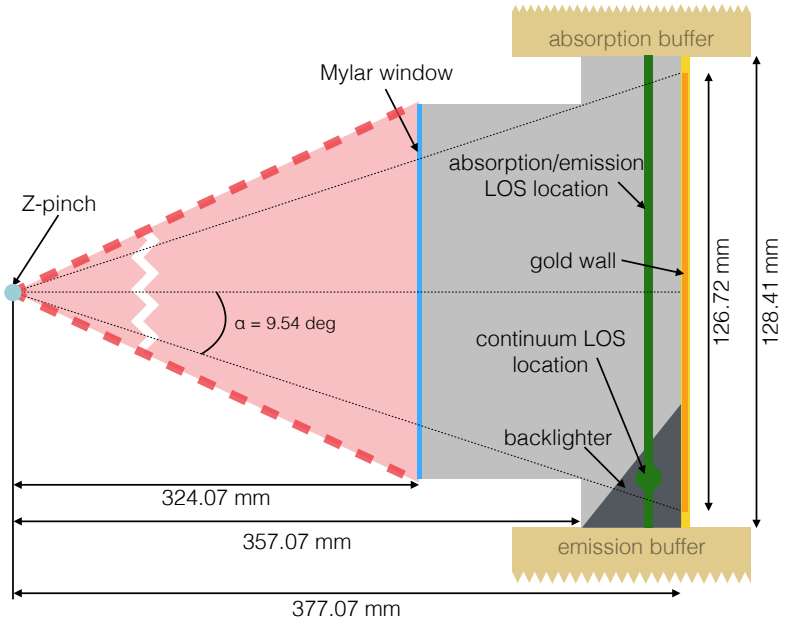

Figure 5.1: Schematic cross-section along the gas cell. Compare to Fig. 3.9. I identify relevant distances and angles. The absorption and emission LOS (green line) are 10 mm from the gold wall. I also give the location of the continuum LOS (green dot), which is looking down onto the backlighter. Locations of the Mylar window and the gold wall are also indicated. The gold wall is subdivided into two parts: the portion directly heated by the Z-pinch X-rays (orange, smaller dimension) and the physical dimensions of this piece of hardware (yellow, larger dimension).

Fig. 5.1 shows the locations of the absorption, emission (green line), and continuum (green dot) LOS with respect to the gold wall. The relationship

between the Z-pinch X-rays, the gas cell geometry, and the LOS depicted in that figure demonstrates a fundamental source of plasma gradients in the WDPE. Specifically, the gold wall in Fig. 5.1 has a total length of 128.41 mm (yellow region in that figure), while the geometry of my gas cell restricts the region directly exposed to the Z-pinch to 126.72 mm (orange region in Fig. 5.1). Since the absorption LOS ends on the backlighting surface, it only crosses this cooler plasma region once. The emission LOS, which enters and exits the gas cell, is exposed to *both* cooler plasma regions. The dimensions of the heated gold wall shown in Fig. 5.1 were calculated assuming that the Z-pinch is a point source. While this does not reflect reality, it represents a slight *underestimate* ($\sim$1%) of the gold wall region exposed directly to the Z-pinch. Therefore, the physical dimensions of the unheated gold wall are *overestimated*. The influence of these effects on the recorded spectra are explored in Sec. 5.6.

5.3 Potential sources of gradients resulting from design of WDPE platform

The motivation for my investigation of plasma inhomogeneities in the WDPE is the apparent disagreement between the $n_{\rm e}$ values inferred from Hβ and Hγ transmission features at every time step in every experiment. As outlined in Ch. 4, and Falcon et al. (2015a,b), these transmission features are extracted by subtracting experimental emission spectra from the corresponding absorption spectra and normalizing the resulting transmission feature. The design of the WDPE platform and its interaction with the Z-pinch X-rays

gives rise to plasma inhomogeneities. In this section, I discuss three sources of inhomogeneities that are directly tied to the hardware of the WDPE: the buffers, the gold wall, and the backlighting surface (see Figs. 3.9 and 5.1).

5.3.1 The absorption and emission buffers

Each LOS is equipped with a so-called buffer (see Fig. 3.9) to protect the collection optics from the harsh plasma conditions found in the main gas cell body. Due to the design of the WDPE platform, the buffers are also filled with hydrogen gas during an experiment. There is thus the possibility of plasma forming in these hardware regions as well. The WDPE design completely eliminates the direct interaction between the buffer gas and the Z-pinch X-rays (see black dotted lines in Fig. 5.1). However, the photons produced by the hydrogen plasma formed in the main gas cell body during an experiment have the potential to heat the buffer gas. This interaction is limited by inserting a 5 mm aperture between the main body of the gas cell and each buffer (see Fig. 5.2). Only one of the 5 mm apertures shown in Fig. 5.2 allows photons to enter the buffer; the other two will be covered by the face of the buffer. Since the absorption and emission LOS must enter and exit the absorption buffer (see Fig. 3.9), its design includes two such apertures. The absorption buffer therefore receives twice the photon flux compared to the emission buffer. The emission LOS traverses both buffers, while the data collected with the absorption LOS is only exposed to the absorption buffer (see Fig. 3.9).

I estimate the effects of the main plasma body on the buffer gas by

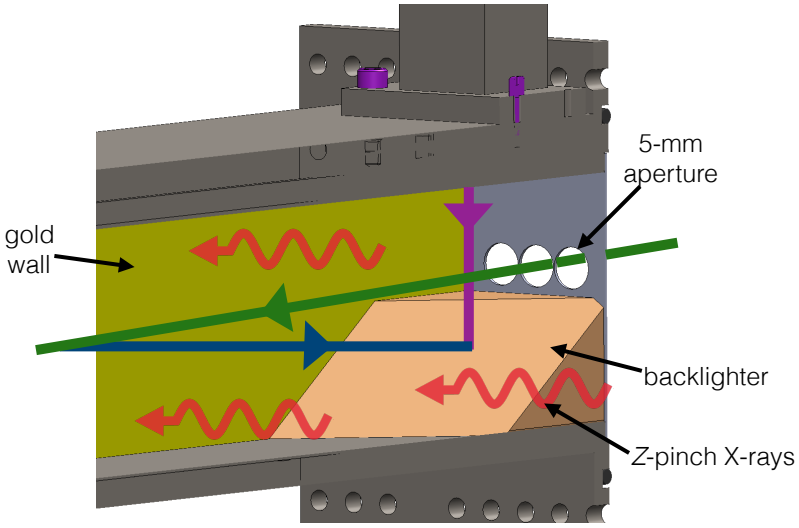

Figure 5.2: Detailed view of the backlighter. Major gas cell components are identified. I again show the different LOS shown in Fig. 3.9. The directions of the LOS are also indicated. The Z-pinch X-rays in this figure are perpendicular to the gold wall and backlighter.

calculating a 1.9 eV blackbody spectral energy distribution. This temperature represents a ∼40% increase over experimentally determined maximum temperature of 1.35 eV (Falcon 2014; Falcon et al. 2015b). Using this blackbody distribution in conjunction with the hydrodynamics code Helios (MacFarlane et al. 2006), I then calculate the resulting temperatures in the absorption and emission buffers. The blackbody flux is doubled for the absorption buffer simulation to account for the additional aperture included in its design (see discussion above). I find that this flux-buffer interaction results in a maximum temperature of ∼0.25 eV in either buffer. Such a temperature is not sufficient to promote a significant number of hydrogen atoms into the n=2 state. Ac-

cording to these calculations, these effects should therefore not influence my absorption or emission measurements.

5.3.2 The gold back wall

The gold back wall provides the second potential source of inhomogeneities in the WDPE platform. Due to its relatively large physical extent, the heating provided by this piece of hardware will vary depending on the precise view factor of each plasma location along the gold wall. I qualitatively derive the different contributions of the entire wall on a single plasma region by using the following equation:

$$\text{heating contribution} = \frac{2}{z} \times \tan^{-1}\Big(h \times \frac{d}{z \times \sqrt{h^2 + 4d^2 + 4z^2}}\Big) \tag{5.1}$$

In the above equation, z represents the distance from the gold back wall to the absorption/emission LOS ($z = 10$ mm in my case, see Secs. 5.3.3 and 5.4), h is the height of the gold wall, which for my setup is equal to 22.51 mm, and d is the distance along the gold back wall, with the center being defined as 0.00 mm. During the derivation of Eq. 5.1, an optically thin plasma was assumed. This is a simplification not representative of reality. Nonetheless, application of Eq. 5.1 to the WDPE geometry yields valuable information about relative gold wall heating contributions. The results are shown in Fig. 5.3. Clearly, the edges of the plasma will be cooler than the main body, introducing notable inhomogeneities in the WDPE. These effects will be further investigated in

Sec. 5.5.

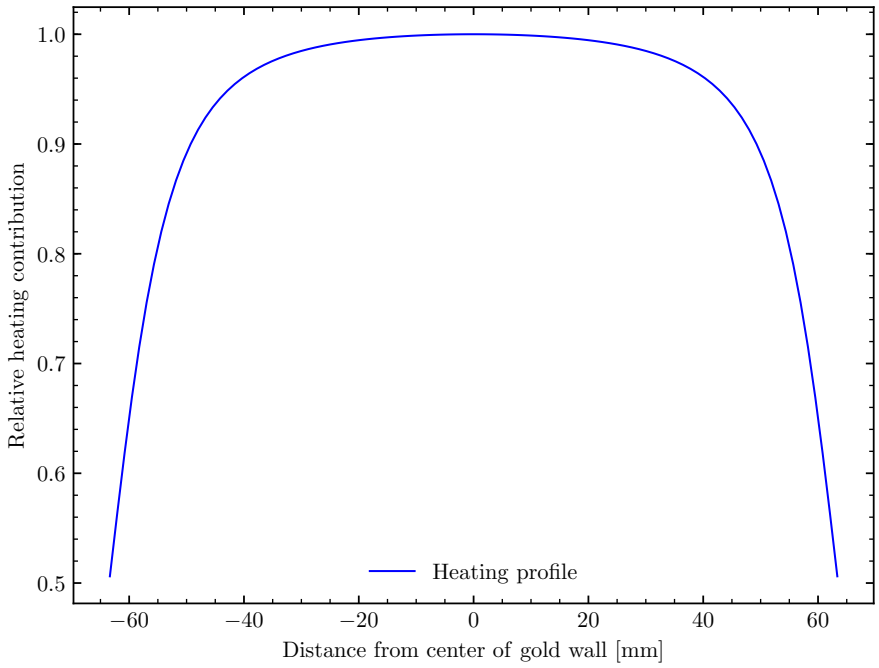

Figure 5.3: Relative plasma heating contributions as a function of distance along the gold back wall. This heating profile is responsible for the most significant WDPE plasma inhomogeneities.

5.3.3 The backlighting surface

Unlike all other hardware gradients I discuss in this section, the backlighting surface only affects the absorption LOS (see Figs. 3.9 and 5.2). In particular, the hydrogen plasma gets heated by two different sources in the vicinity of this piece of hardware: the gold wall and the backlighter itself. The influence of the backlighting surface on final plasma conditions can be ascertained by performing Helios simulations.

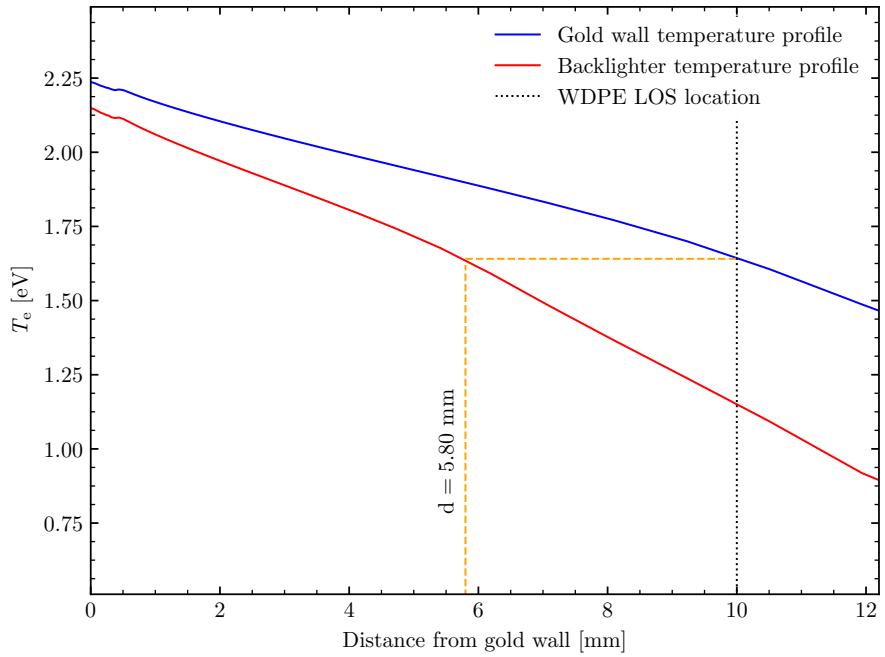

Figure 5.4: Results of a LTE simulation comparing the heating influence of the gold back wall (blue) and the backlighter (red) as a function of distance from the respective pieces of hardware. At the nominal 10 mm LOS (dotted line) for the WDPE, the backlighter dominates the gold wall within $\sim$ 5.80 mm of its surface. The plasma heated by the backlighter reaches a maximum temperature of $\sim$2.15 eV at the surface.

Fig. 5.4 shows a comparison of simulated plasma temperatures as a function of distance from the gold wall (blue) and backlighter (red). The backlighting surface is at a 45° angle with respect to the gold wall and therefore experiences a reduction in incident flux by $\sqrt{2}$. Consequently, the backlighter produces lower plasma temperatures than the gold wall.

In the standard WDPE optical setup, the absorption, emission, and continuum LOS are located 10 mm from the gold wall. All data presented

and analyzed in this chapter were collected at that distance. Ascertaining the relative influence of backlighter and gold wall heating is achieved by determining the plasma temperatures produced by these two pieces of hardware 10 mm from their surface (black dotted line in Fig. 5.4). At this distance, the gold wall heats the plasma to ∼1.6 eV. The plasma created by the backlighter reaches the same temperature at ∼5.8 mm from its surface. The backlighter thus dominates the plasma heating in that region of the absorption LOS and raises the plasma temperature to 2.15 eV over these 5.8 mm. These simulations were performed assuming LTE.

5.4 Review of critical data

5.4.1 Comparison of fully calibrated n_e measurements

Fig. 5.5 shows the percent difference in n_e derived from Hβ and Hγ for three experiments: z2553, z2787, and z2788. All of these experiments are performed under the same experimental conditions and setups. The n_e values used to calculate the percent differences shown in that figure are derived from detailed line-profile fits to 10 ns integrations of my data (see Fig. 4.12 and associated discussion). I use four different hydrogen line-shape theories to extract the plotted n_e values: VCS (Vidal et al. 1973), Gigosos et al. (2003), Tremblay & Bergeron (2009), and Gomez et al. (2016). The n_e inferred by all these theories agree within a few percent (see Falcon et al. 2015b). I therefore only show the theory-averaged percent difference in Hβ n_e and Hγ n_e for each time-step in my experiment. Additionally, I also show the time-averaged Hβ-

Hγ disagreement for each experiment (z2553 - green, z2787 - red, z2788 - blue) in Fig. 5.5. These time-averaged differences agree very well, indicating that whatever process is responsible for them is omnipresent in my experiments. The data shown in Fig. 5.5 indicates that the n_e values derived from Hβ are $\sim$40% higher than those of Hγ. If I assume the Hβ n_e to be correct, this then implies an *underestimate* of the theoretical Hγ FWHM in *absorption*.

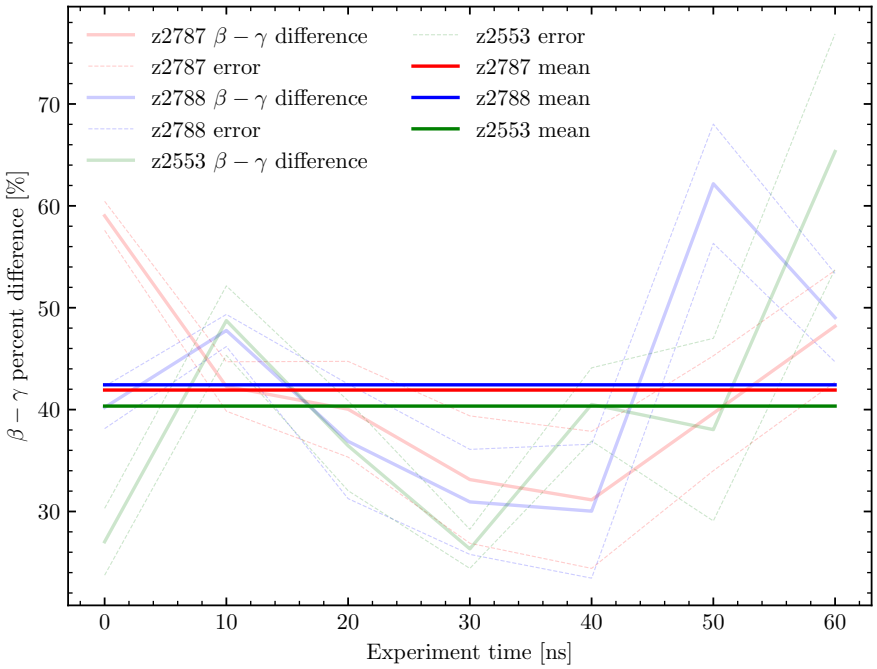

Figure 5.5: Percent differences between Hβ and Hγ n_e as a function of experiment time for shots z2553 (green), z2787 (red), and z2788 (blue). The time-trends are determined by averaging the n_e values inferred from the hydrogen line-shape theories discussed in the text. I also show the time-averaged n_e percent difference as solid straight lines for each shot.

Discrepancies observed between Hβ and Hγ in *absorption* are not com-

pletely without precedent. As mentioned above, Tremblay & Bergeron (2009) analyzed hydrogen WD spectra with a model that had been validated using the emission experiments of Wiese et al. (1972). They found that including increasingly higher order members of the Balmer series (i.e., Hγ, Hδ, Hϵ, etc.) decreases the inferred $n_{\rm e}$ of the WD atmosphere as compared to an Hβ-only fit. This is further evidence that the calculated line width is underestimated for increasingly higher order members of the Balmer series. See their Fig. 2 and associated discussion for more details. In my case, however, I am not fitting astronomical objects, but experimental *absorption* spectra, which should be much easier to analyze and understand. In a WD atmosphere, it is not possible to directly measure the particle density of the plasma. I can perform such a measurement in the WDPE. Furthermore, a standard WD atmosphere covers five orders of magnitude in $n_{\rm e}$ and a factor of four in $T_{\rm e}$. The emergent line profile is integrated over the entirety of those plasma conditions. Plasma gradients undoubtedly exist in my experimental platform as well, but are not expected to be nearly as severe (see Sec. 5.6.3.1 for more information). Unlike a WD atmosphere, I am also able to perform experimental tests to constrain any potential gradients. Finally, as explained in Ch. 4, I observe the plasma using three different LOS, providing me with vastly increased diagnostic capabilities with respect to a standard WD observation. To investigate the origins of the observed difference in $n_{\rm e}$ derived from Hβ and Hγ, I perform a full investigation into possible plasma inhomogeneities in the WDPE.

5.4.2 Comparison of Hβ and Hγ absorption and emission profiles

In addition to comparing the derived $n_{\rm e}$ values from Hβ and Hγ, further insight into the apparent disagreement of these two features can be gained from direct comparison of their absorption and emission line shapes. As pointed out in Ch. 4, I perform an emission-subtraction of the absorption data to then derive transmission spectra. Therefore, the absorption and emission LOS should sample the same $n_{\rm e}$ values, or else such a subtraction approach is incorrect. Assuming that complete redistribution applies to my plasma and that absorption and emission sample the same $n_{\rm e}$ regions, I should then derive matching line-shapes from the WDPE emission and absorption datasets. The theoretical foundation for this comparison is given below.

5.4.2.1 Theoretical foundation for line-shape comparison

The fundamental equation controlling all aspects of my experimental data is given by the radiative transfer equation (e.g., Rybicki & Lightman 1986):

$$\frac{dI_\nu}{ds} = -\alpha_\nu I_\nu + j_\nu \tag{5.2}$$

where I_ν is the frequency dependent intensity, α_ν is the absorption coefficient (or opacity), j_ν is the emission coefficient (or emissivity), and ds is a path element. Assuming a uniform plasma of length L, Eq. 5.2 can be solved and integrated along a path to give the emergent spectrum as:

$$I_\nu = S_\nu(1 - T_\nu) + I_\nu(0) \times T_\nu \tag{5.3}$$

with

$$S_\nu = \frac{j_\nu}{\alpha_\nu}. \tag{5.4}$$

$$T_\nu = e^{-\alpha_\nu L} \tag{5.5}$$

Here, T_ν is the transmission probability as a function of frequency ν, while S_ν is the so-called source function. In the case of bound-bound transitions, which dominate the spectra of the data collected in the WDPE experiments, I can also derive precise expressions for the path-integrated emissivity and opacity of my plasma:

$$j_\nu = h\nu_{ul} n_u A_{ul} \times \phi(\nu) \tag{5.6}$$

$$\alpha_\nu = \frac{8\pi e^4}{3m_e^2 c^4} n_l f_{lu} \times \phi(\nu). \tag{5.7}$$

In these equations, ν_{ul} is the frequency of the transition in question, A_{ul} represents the spontaneous decay rate, n_u and n_l represent the upper and lower state populations, and f_{lu} is the oscillator strength of the transition. The common construct shared by the opacity (α_ν) and the emissivity (j_ν) is the area-normalized line-shape function, $\phi(\nu)$. Since all variables preceding $\phi(\nu)$ in Eqs. 5.6 and 5.7 are approximately constant (i.e., weakly dependent on ν) in my experimental data, the spectral distribution of my emission or absorption lines is entirely determined by the line-shape function. Accurate knowledge of the line-profile function $\phi(\nu)$ is required for many other plasma diagnostic applications (e.g., Ahmed et al. 2017) and the general understanding of radiation transport in plasmas.

The WDPE captures emission and absorption data separately, meaning that Eq. 5.3 can be further simplified. The first term on the right-hand-side (RHS) in Eq. 5.3 gives the emergent self-emission of the plasma and therefore mirrors my emission data. The second term on RHS of that equation corresponds to my absorption spectra and describes the intensity at the backside of the observed region [$I_\nu(0)$] transmitted through the plasma. In the case of the emission data, I set $I_\nu(0) = 0$, meaning that Eq. 5.3 reduces to:

$$I_\nu^{\text{em}} = S_\nu(1 - T_\nu) \tag{5.8}$$

For my absorption data, self-emission effects are negligible at early times (t $\lesssim$ 40 ns, Falcon 2014) leading to:

$$I_\nu^{\text{abs}} = I_\nu(0) \times T_\nu \tag{5.9}$$

Absorption Data For experimental absorption spectra, the first step of my line-shape comparison methodology conversion consists of transmission extraction. I showed in Eq. 5.9 that my experimental absorption data is equivalent to the intensity at the backside of the observed region multiplied by the transmission through the plasma. In Sec. 5.4.2.1, I also mentioned that the dominant source of opacity in the WDPE experiments comes from bound-bound transitions. I can therefore use the continuum regions between the observed spectral features as an estimate for the backlighter intensity $I_\nu(0)$ and normalize my data to arrive at:

$$\begin{aligned} T_\nu &= I_\nu^{\text{abs}}/I_\nu(0) \\ &= e^{-\alpha_\nu L} \end{aligned} \tag{5.10}$$

where I have made use of Eq. 5.5.

Emission Data My experimental emission data has the form of (see Eq. 5.8):

$$I_\nu^{\rm em} = S_\nu(1 - T_\nu) \tag{5.11}$$

Through continuum normalization (which requires me to assume that S_ν is constant over the line profile, a likely valid assumption), I can transform my emission profile to:

$$I_\nu^{\rm em} \approx (1 - T_\nu) \tag{5.12}$$

Eq. 5.12 is clearly non-linear. However, since the experimental emission feature suffers from optical depth effects, it cannot be processed beyond the form of that equation. I note here that no assumptions regarding the optical depth of the plasma have been made in the derivation of Eq. 5.12.

Comparing absorption and emission line shapes Eq. 5.12, which represents the final form of the processed experimental emission spectra, dictates my extraction of the absorption features. Using the same arguments that led to Eq. 5.10, I can convert the observed absorption data to transmission. I have:

$$I_\nu^{\rm abs} = T_\nu \tag{5.13}$$

To obtain a result similar to the emission result of Eq. 5.12, I then invert the transmission profile across the continuum to give:

$$(1 - I_\nu^{\rm abs}) = (1 - T_\nu) \tag{5.14}$$

Eqs. 5.11 and 5.14 are both in the form of (1-T_ν). Any potential non-linearities will therefore affect those two equations equally. To remove any scaling differences introduced by the processing procedures, I force the resulting emission and absorption data to have an integrated area of one. This final step allows for direct comparison of emission and absorption profiles and will allow me to ascertain whether gradients represent any serious threat to my experimental data. The derivation presented here only applies to experimental data at early times, since the influence of self-emission on the absorption spectra has been neglected. The absorption-emission time evolution of shot z2553 (a pure H_2 gas fill observed at 10 mm) shown in Fig. 5.6 shows that self-emission does not become significant until $t \lesssim 40$ ns. The comparison presented in Sec. 5.4.2.2 is thus restricted to these early times.

5.4.2.2 Comparison of processed experimental data

In Sec. 5.4.2.1, I described a method that allows me to directly compare emission and absorption profiles for both Hβ and Hγ. Once I apply this method to my experimental absorption and emission data, the processed spectra in Figs. 5.7 and 5.8 result. The results shown in those plots can be reproduced for over 10 WDPE experiments and always result in the same trends.

A brief look at both Figs. 5.7 and 5.8 immediately reveals a large difference between the behavior of Hβ and Hγ in the WDPE. While everything behaves as expected for the Hβ profile (i.e., absorption and emission profiles agree, except in the core where optical depth and boundary layer plasma ef-

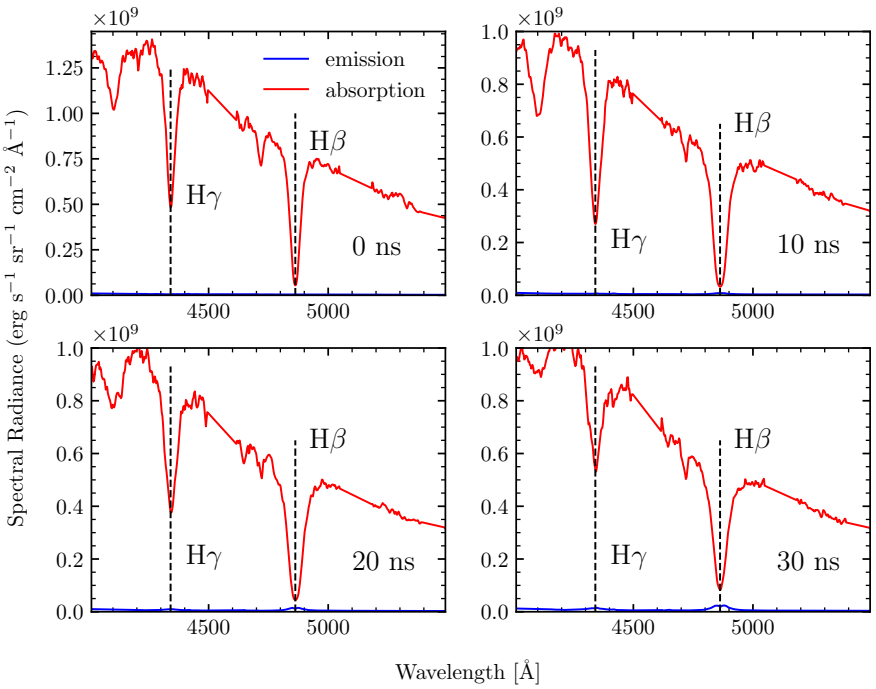

Figure 5.6: Time evolution of the z2553 absorption (red) and emission (blue) data. I show these datasets in absolute units. Self-emission of the plasma (shown in blue) does not become significant until ∼40 ns.

fects become important), the same argument cannot be made about the Hγ profiles. Could it be that the behavior shown in Figs. 5.5, 5.7, and 5.8 stems from plasma gradients? I will explore this possibility in the next section.

5.5 Constraining plasma gradients in the WDPE gas cell

I now combine the considerations presented in Sec. 5.2 with WDPE data to derive and constrain plasma inhomogeneities in the WDPE platform.

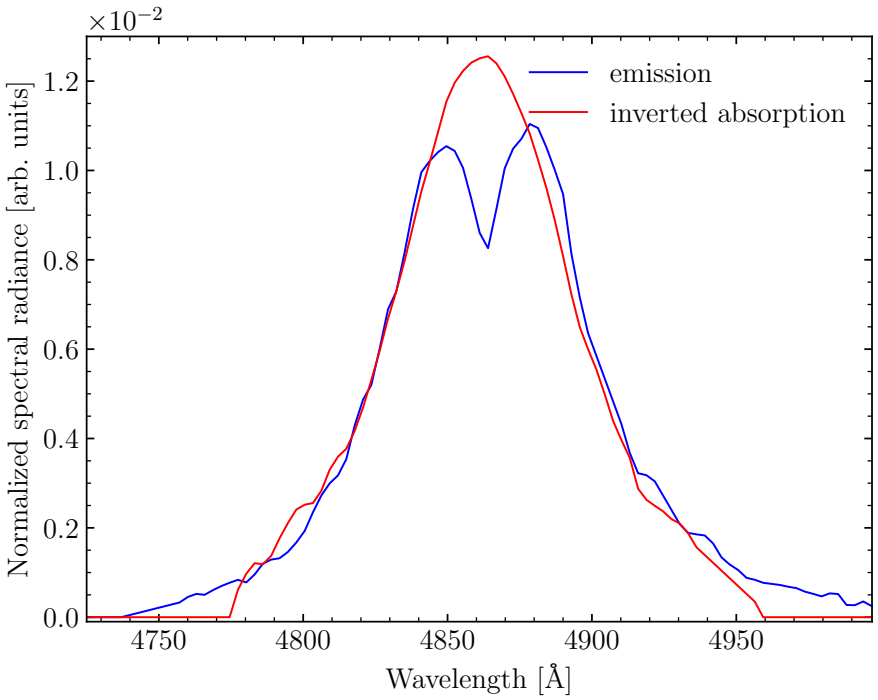

Figure 5.7: Comparison of representative area-normalized Hβ from shot z2553 at 20 ns. These spectral features were processed according to the description given in Sec. 5.4.2.1. The two line profiles are in excellent agreement, except for the core, were optical depth and boundary layer plasma effects become significant.

The most important parameters in any such investigation are T_e and n_e measurements. Since all the experiments considered in this chapter were performed with a pure hydrogen gas fill, the experimentally determined n_e will allow me to directly determine a LTE T_e (Falcon et al. 2015b). The datasets I process in this section do not easily lend themselves to the line profile fitting method I describe in Sec. 5.4. I therefore developed an alternate n_e extraction approach that does not rely on absolute calibrations, emission-corrected

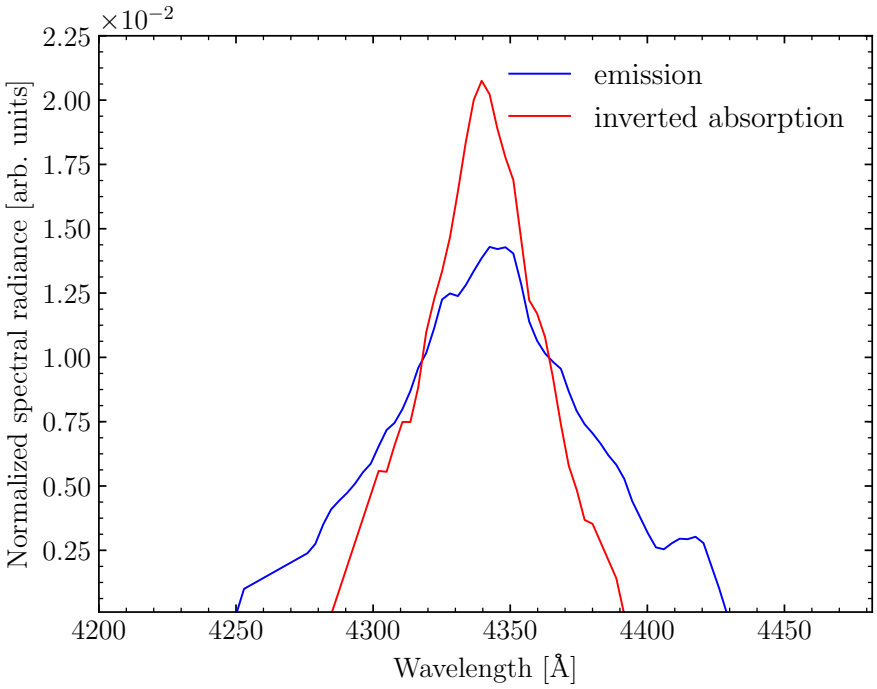

Figure 5.8: Comparison of representative area-normalized Hγ from shot z2553 at 30 ns. These spectral features were processed according to the description given in Sec. 5.4.2.1. Unlike the the Hβ profiles shown in Fig. 5.7, the Hγ profiles in absorption and emission do *not* agree.

absorption spectra, or detailed line-profile fits. The specifics of my approach are given in App. E.

Fig. 5.9 shows a comparison of the n_e values derived from detailed line-profile fits to those obtained from the full-width-at-half-area (FWHA) method described in App. E. The purple line in that figure gives the percent difference between the FWHA and line-profile fitting approach. The n_e values derived by the two methods agree well. I thus feel justified in using the FWHA approach

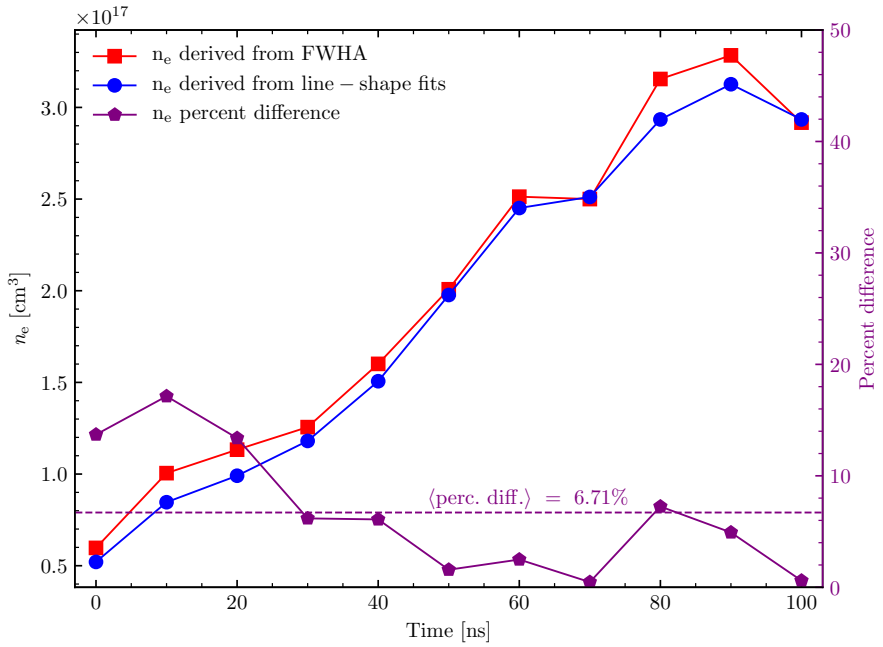

Figure 5.9: Comparison of n_e values inferred from detailed line-profile fits to emission-corrected absorption spectra (blue) to the FWHA n_e values inferred from uncorrected absorption spectra. The results agree very well. I also show the calculated percent difference between the two methods (purple).

to extract n_e values from my experimental data. All further n_e values presented in this chapter were derived using the FWHA approach.

Using the FWHA technique in conjunction with the WDPE absorption and continuum data, I now derive a T_e and n_e gradient along the gold wall. Specifically, I will obtain the absorption vs. continuum LOS n_e ratio. The reasoning behind deriving this parameter is simple: spectra resulting from the absorption LOS represent an integration along the entire gold wall (see Fig. 5.10). The continuum LOS observes only the very edge of the gas cell

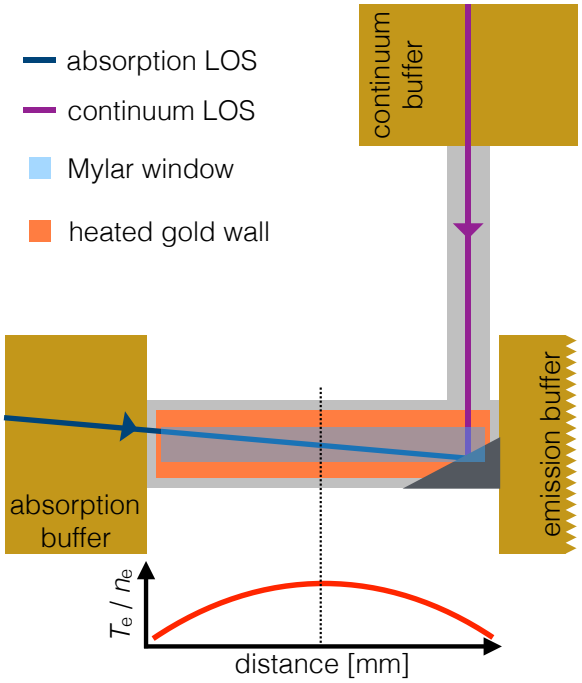

Figure 5.10: Comparison of absorption (blue) and continuum (purple) LOS optical paths. The absorption LOS integrates along the gold back wall, while the continuum dataset allows me to measure the n_e values at the edge of the gas cell.

(see Fig. 5.10), normal to the absorption optical path. If a gradient such as the one shown at the bottom of Fig. 5.10 existed, I would then expect an analysis of the absorption spectra to result in higher n_e values than the continuum data. Such a potential n_e difference can then be used to constrain inhomogeneities along the gold wall. Since the backlighter heats the plasma in these regions as well, any n_e values I derive from the continuum LOS will present a *lower* bound on these measurements. I use five calibration shots (see Ch. 4) to perform this absorption vs. continuum comparison. Their optical as

well as experimental setup is always the same, making them ideal candidates for this purpose.

Sample raw absorption and continuum Hβ spectra in optical depth units at various times are shown in Fig. 5.11. The absorption spectra shown in that figure were *not* corrected for emission. I also display Voigt fits to hydrogen lines in that figure. The left column in Fig. 5.11 depicts my cleanest data at $t = 0$ ns, while the right column gives the data at $t = 80$ ns. From this figure, it is obvious that the continuum signal (bottom row) is much lower than that of the absorption (top row) LOS. This is expected since the absorption LOS integrates over $\sim$110 mm of plasma, while the continuum LOS only integrates over $\sim$15 mm. It is also evident that any continuum data observed at $t >$ 80 ns will suffer from signal-to-noise (S/N) issues. Any n_e values derived from this LOS at later times should therefore be consumed with caution.

The most instructive parameter for determining the gradient along the gold wall is the ratio of continuum and absorption n_e values. Fig. 5.12 shows this ratio for all five calibration shots used in this section. Continuum and absorption n_e measurements are approximately equal at early times. At $t \geq$ 40 ns, the n_e values derived from the absorption LOS are significantly higher than those of the continuum spectra. The continuum-absorption n_e ratio stabilizes at $t = 60$ ns for all shots. Two plausible explanations exist for this behavior. Radiation transport effects in the plasma are the most likely explanation for the n_e trends presented in Fig. 5.12. The plasma is optically thin at early times, enabling the entire gold wall to heat all regions of the plasma

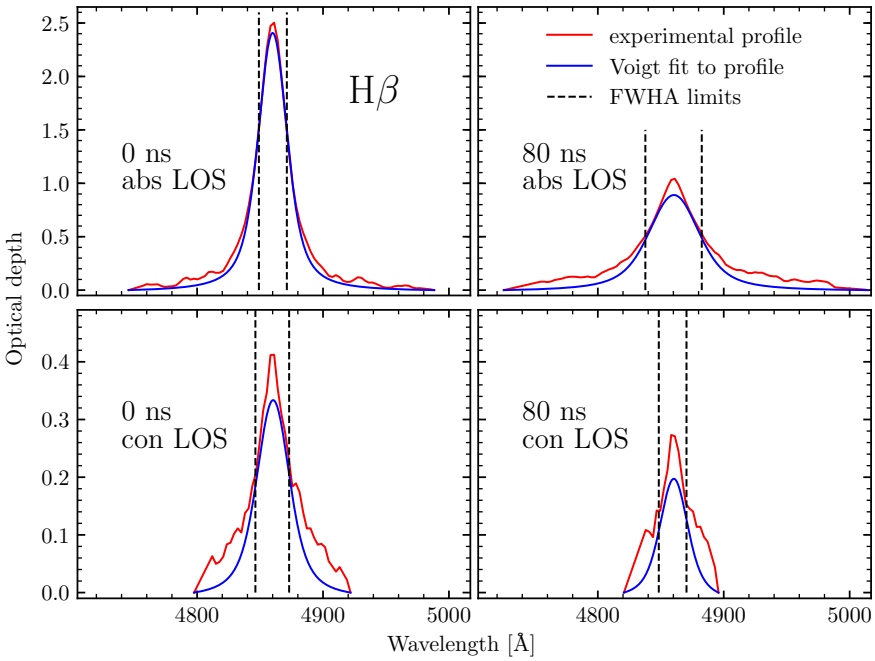

Figure 5.11: Comparison of Hβ absorption (top row) and continuum spectra (bottom row). Several Absorption spectra exhibit much stronger spectral features than the continuum data, as expected from path length differences in the two LOS.

more homogeneously than in the optically thick case (Falcon et al. 2015b). In this optically thin stage, I would still expect the edges of the plasma to be slightly cooler than the central component due to the physical extent of gold wall (see Sec. 5.3.2). At later times, the opacity of the plasma changes in such a way as to reduce the efficiency of the gold wall heating, especially at the boundary regions of the gas cell. This behavior is qualitatively demonstrated in Fig. 5.13. The absorption-continuum n_e ratio is expected to decrease with increasing time of the experiment due to this effect. This is exactly what

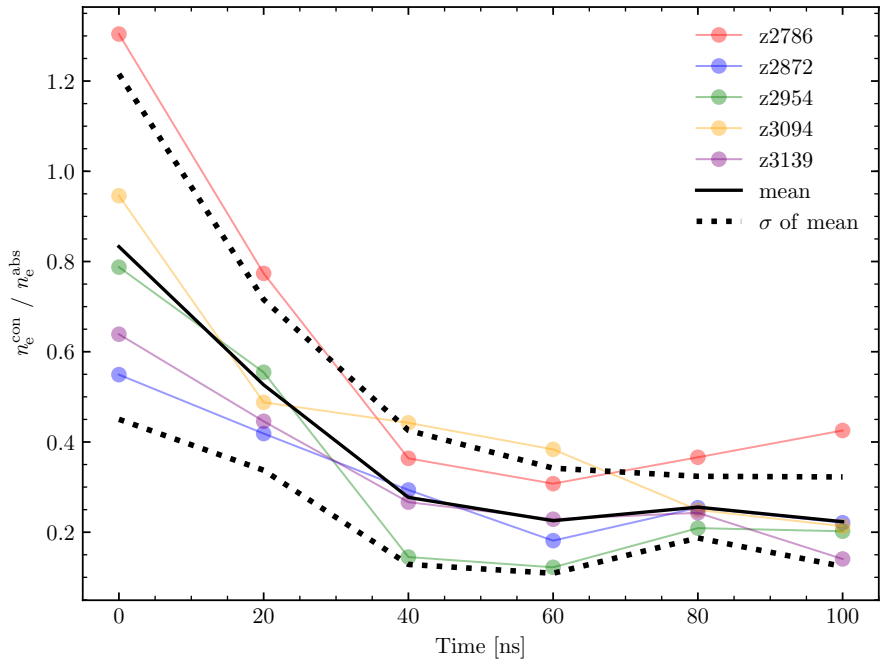

Figure 5.12: The ratio of n_e values inferred by the continuum data to that derived from the absorption data. I also show the mean ratio (black line) and its standard deviation (dashed black line) derived from all shots. The n_e-ratio trends are the same for all shots, regardless of gas fill.

is observed in Fig. 5.12. This explanation appears to be supported by the experimental data as well as the absorption and continuum n_e measurements.

Another potential explanation for the trends observed in Fig. 5.12 could be found in the data acquisition location. Since the continuum data is collected close to the edge of the cell, pressure gradients could push the plasma into the buffers thereby lowering the observed T_e and n_e of this LOS as compared to the absorption LOS. Calculating the plasma sound speed in the gas cell allows me to test the viability of this explanation. This is calculated to be

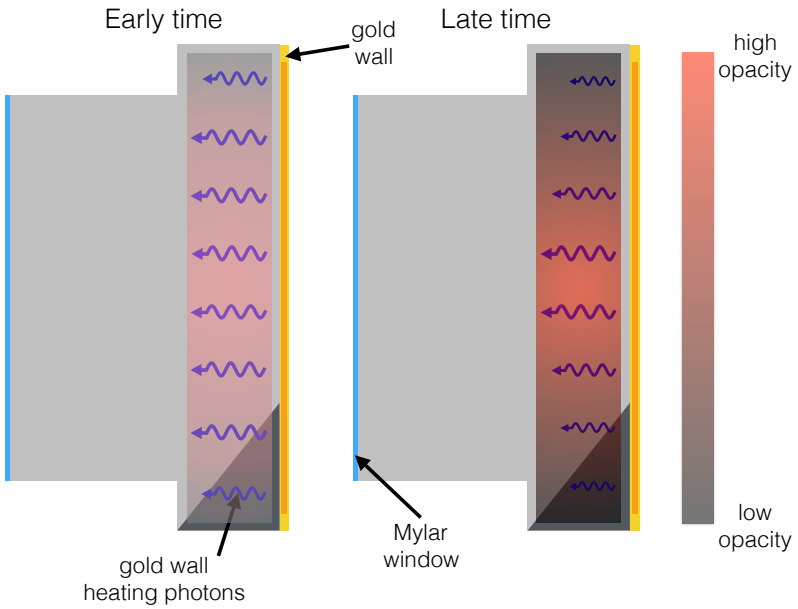

Figure 5.13: I show the evolution of the opacity in my gas cell. Early in time (left), the opacity of my plasma is nearly uniform along the gold wall. As the experiment progresses, the opacity becomes higher at the center of my gas cell and lower at the edges (right). Such behavior explains the experimental data and the n_e trends observed in Fig. 5.12.

$c_s = 1.22{\times}10^7$ mm/s. Thus, over the course of a 100 ns experiment, plasma particles and electrons move $\sim$1.22 mm. This velocity is not enough to move particles out of the continuum LOS, which has a diameter of $\sim$3 mm (see Ch. 6 and Falcon et al. 2015a).

The data presented in Fig. 5.12 enables me to derive a gradient for the plasma along the heated regions of the gold back wall. As noted above, the experiments considered in this chapter are performed using a pure hydrogen gas fill, so n_e and T_e are intimately related. Higher derived n_e measurements are

the result of higher T_e values and vice versa. The experimental measurements imply that $n_{e\ bulk,\ max} \approx 3.12{\times}10^{17}$ cm^{-3}, while $n_{e\ edge,\ max} \approx 0.89{\times}10^{17}$ cm^{-3}, which leads to $n_{e\ edge,\ max}$ / $n_{e\ bulk,\ max} \approx 0.29$. From the absorption n_e values and the measured total particle density, I can also derive an LTE $T_{e\ bulk,\ max} \approx 1.35$ eV. Using all these constraints in conjunction with the physical dimension and time constrains of the WDPE, I can derive a unique solution for the gradient along the gold wall. This plasma gradient is symmetric, has a maximum temperature of 1.9 eV at the center of the gas cell and drops to 0.85 eV at the edges. Its complete structure is discussed in Sec. 5.6.

5.6 Plasma gradients along the absorption and emission LOS

I now use all previously discussed parameters and constraints to derive a complete description of the plasma inhomogeneities along each LOS. Absorption and emission gradients are of crucial importance to the WDPE since each of these datasets is used to extract transmission spectra (see Sec. 5.4, Falcon et al. 2015a,b), which, in turn, allow me to extract a n_e measurement. One hypothesis to be tested is the possibility of the absorption and emission LOS probing different n_e environments. If that should be the case, I could then potentially explain the 40% difference in n_e derived from Hβ and Hγ. Another hypothesis that could be explored is data analysis weaknesses. The investigation of most hypotheses requires a detailed understanding of T_e and n_e trends along each LOS. I begin my analysis with the absorption optical

path.

5.6.1 The absorption LOS

Fig. 5.14 shows a simplified version of the absorption LOS. Details of the absorption LOS and its data collection physics are described in Ch. 3. Potential gradients along this LOS are discussed in Sec. 5.3. I now combine all aspects of this optical path to derive a T_e gradient as a function of distance along this LOS.

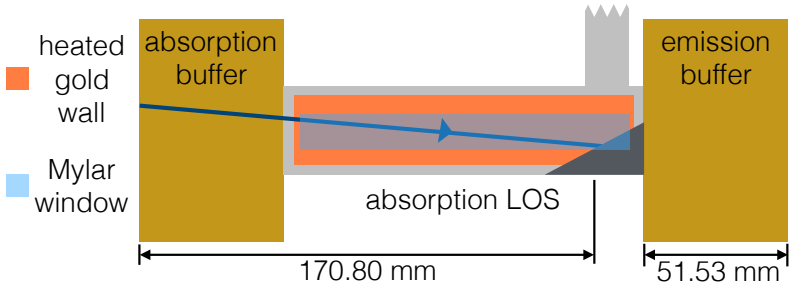

Figure 5.14: Schematic representation of the absorption LOS. The optical path begins in the absorption buffer and then proceeds to cross the unheated region of the gold wall to finally enter the main body of the plasma. This optical path ends on the backlighting surface.

As shown in Fig. 5.14, the absorption LOS first traverses the absorption buffer. The discussion in Sec. 5.3.1 revealed that only a few millimeters of the buffer closest to the gas cell body will experience a significant change in temperature due to the plasma in the main gas cell body. More specifically, the temperature of the absorption buffer plasma will rise to at most 0.25 eV over the final 5 mm. I remind the reader that I have purposely inflated the amount

of energy flux incident on this buffer gas and therefore expect to simulate a temperature higher than that found in the actual buffer. Once the absorption LOS has traversed the buffer and entered the gas cell, it encounters a small section of plasma not exposed to a part of the gold wall directly heated by the Z-pinch X-rays. T_e here rises from 0.25 eV (inner edge of buffer) to 0.85 eV (temperature at edge of gold wall, see Sec. 5.5). After having crossed this cool boundary layer, the absorption LOS arrives at the main body of the plasma, whose T_e and n_e structure was discussed in Sec. 5.5. Only one region remains to be considered in the absorption LOS: the backlighting surface. The discussion in Sec. 5.3.3 shows that the backlighter dominates the heating of the plasma within ∼5.80 mm of its surface. According to Helios simulations, T_e increases from 1.15 eV to 2.15 eV in that final distance.

5.6.2 The emission LOS

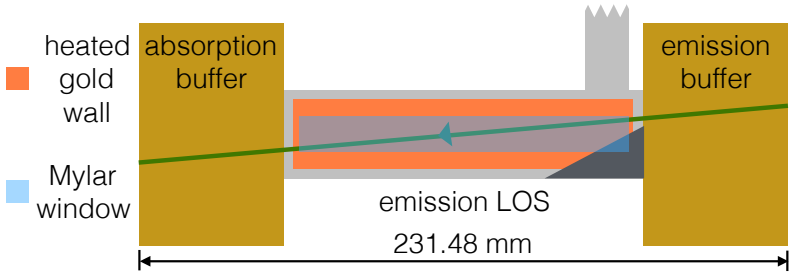

Figure 5.15: Schematic representation of the emission LOS. I identify several hardware components and distances. Please see text for more details.

Fig. 5.15 depicts a schematic of the emission LOS. This optical path begins in the buffer opposite the absorption. It traverses the gas cell at the same

angle as the absorption LOS, ensuring that both optical paths are exposed to the same vertical gradient, should one exist. As discussed in Sec. 5.3.1, the emission buffer receives half the flux from the gas cell body as compared to the absorption buffer, resulting in T_e of $\sim$0.2 eV for that section of plasma. Much like the absorption LOS, the emission now traverses the unheated gold wall until it reaches the heated portion. The modeled absorption and emission T_e trends agree almost exactly until the central part of the gold wall is reached. At that point, the temperature of the emission LOS drops consistently since it is not exposed to the backlighter.

5.6.3 Absorption and emission gradients

I now combine all the data presented in Sec. 5.6.1 and 5.6.2 to derive detailed gradients along the absorption and emission LOS. The resulting T_e gradients are shown in Fig. 5.16, while Fig. 5.17 gives the final n_e structure of my plasma. The simulation program Spect3D (MacFarlane et al. 2007) was used to convert the derived T_e trends to a plasma n_e under the assumption of a pure hydrogen gas fill and LTE conditions. The absorption and emission LOS are on opposite sides of the gas cell and therefore experience slightly different gradients. To allow for an easier comparison of the absorption and emission optical path, I plot the gradients in Figs. 5.16 and 5.17 as a function of distance from the beginning of the respective LOS. With the exception of the backlighter, the gradients along the absorption and emission optical path are very similar. In each of these figures, I show the most extreme potential gra-

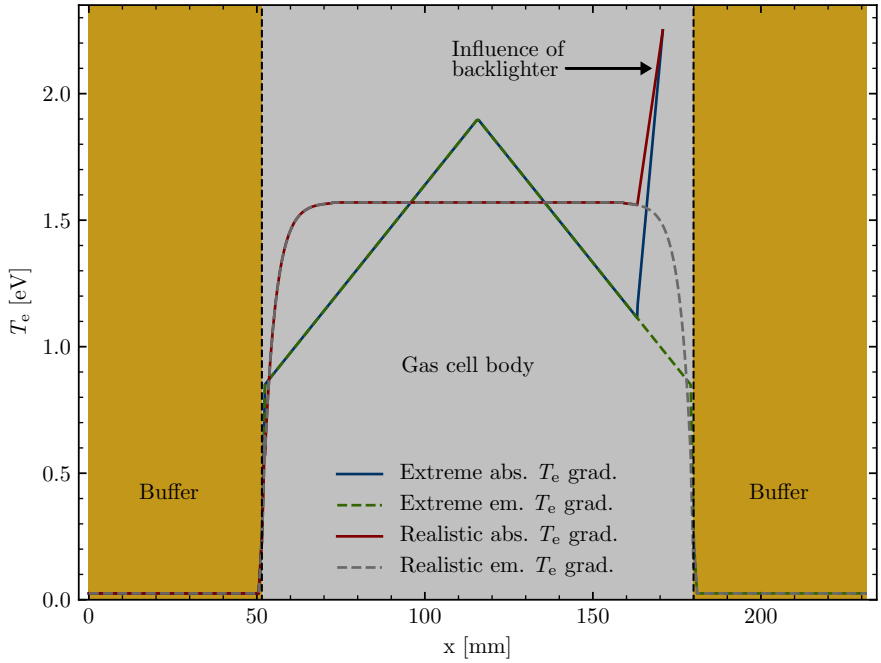

Figure 5.16: The most extreme T_e gradient as a function of the distance from the beginning of the respective LOS. I identify major hardware regions of the gas cell and also highlight the influence of the backlighter on the absorption LOS. For comparison purposes, I also show what I believe to be a more realistic and representative T_e gradient in the platform.

dients (absorption: blue, emission: green dashed) along with inhomogeneity trends I believe to be much more realistic for the WDPE platform (absorption: maroon, emission: grey dashed). I adopt the extreme gradients shown in Figs. 5.16 and 5.17 for the purposes of this investigation. Comparing the realistic and extreme (adopted) gradients highlights the severity of the plasma structure adopted for this inhomogeneity investigation. The purpose of adopting the extreme gradients is to ensure that I am in no way underestimating

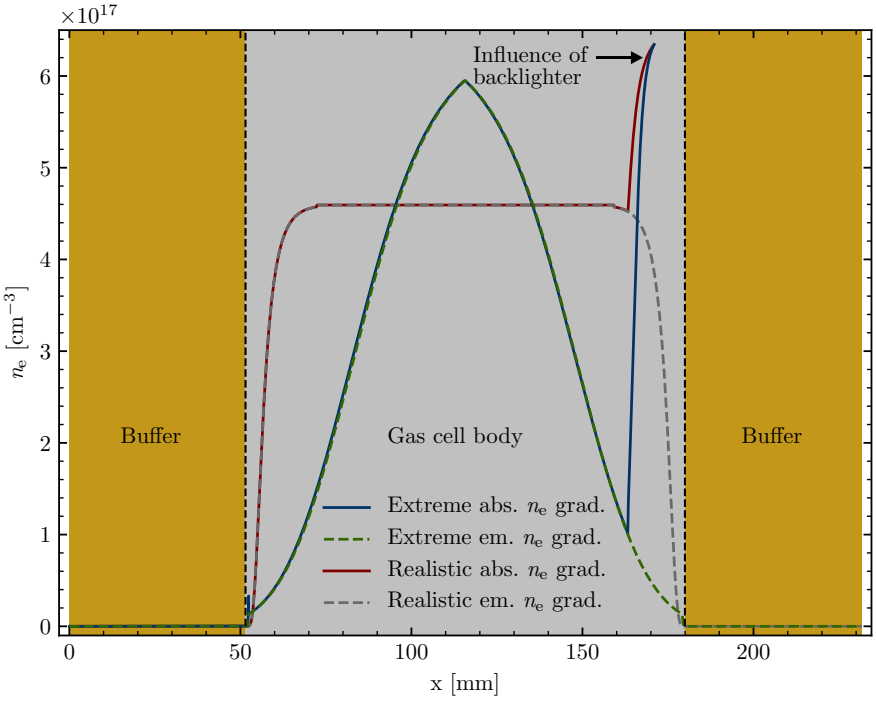

Figure 5.17: The n_e gradients that result from the extreme T_e gradients presented in Fig. 5.16. I identify major hardware regions of the gas cell and also highlight the influence of the backlighter on the absorption LOS. For comparison purposes, I also show what I believe to be a more realistic and representative n_e gradient in the platform.

its effect on my experimental data. To retain as much realism as possible in the adopted gradient, I ensure that its integrated n_e matches that of the experimental data. The reader is reminded, however, that this adopted gradient does *not* represent a physically realistic situation by any means. The integrated effects of these inhomogeneities on the final emergent spectra will be presented and discussed in Sec. 5.6.3.1.

5.6.3.1 Comparison of processed simulation data

An easy and efficient method of determining the influence of plasma structure on my experimental data is to compare the n_e values derived from simulated Hβ and Hγ profiles using the FWHA method I presented earlier. Once I apply this method to Spect3D simulations that incorporate the extreme T_e and n_e gradients shown in Figs. 5.16 and 5.17, the processed spectra in Figs. 5.18 and 5.19 result.

The measured FWHA limits and the associated n_e values for all lines displayed in Figs. 5.18 and 5.19 are listed in Table 5.2. The respective absorption and emission profiles for Hβ and Hγ agree well, but the derived n_e values for these two lines differ quite significantly. For Hβ, the derived n_e values for absorption and emission disagree by 4%, whereas n_e inferred by those two datasets for Hγ shows a 5% difference. However, the absorption-and-emission-averaged Hβ ($\langle n_e \rangle = 3.79\times10^{17}$ cm^{-3}) and Hγ ($\langle n_e \rangle = 3.13\times10^{17}$ cm^{-3}) n_e values differ by $\sim$19%.

Table 5.2: Derived n_e values for my simulated absorption and emission Hβ and Hγ profiles

Line	**type**	**FWHA [Å]**	n_e **[cm^{-3}]**
Hβ	absorption	66.4	3.85×10^{17}
	emission	65.6	3.73×10^{17}
Hγ	absorption	83.8	3.21×10^{17}
	emission	81.2	3.05×10^{17}

In addition to not replicating the experimentally observed 40% differ-

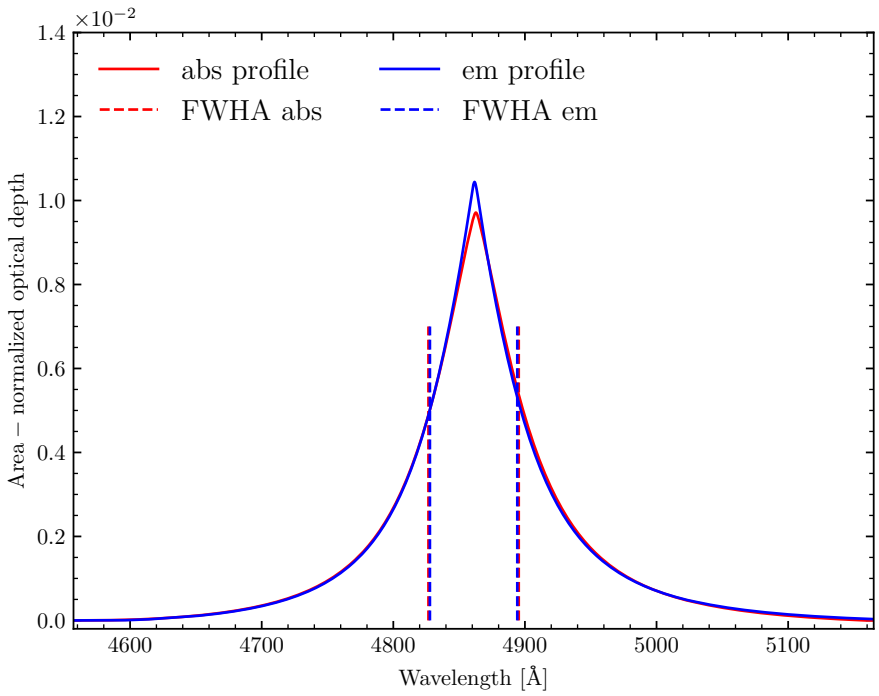

Figure 5.18: Comparison of area-normalized Spect3D Hβ absorption and emission line profiles resulting from the extreme gradients shown in Figs. 5.16 and 5.17. These features were processed according to the description given in E. The two line profiles are in excellent agreement, except for the core, were optical depth and gradient effects become significant. However, the FWHA limits (dashed lines) for these profiles remains largely unaffected.

ence in n_e derived from Hβ and Hγ, the spectra shown in Fig. 5.19 do *not* reproduce the Hγ line profile disagreements depicted in Fig. 5.8. My simulations therefore also seem to imply that gradients are not responsible for those effects. This result leaves two further options for the behavior observed in Fig. 5.8: (1) additional gradients that could be responsible for the experimental Hγ absorption-emission disagreement have been neglected in the analysis

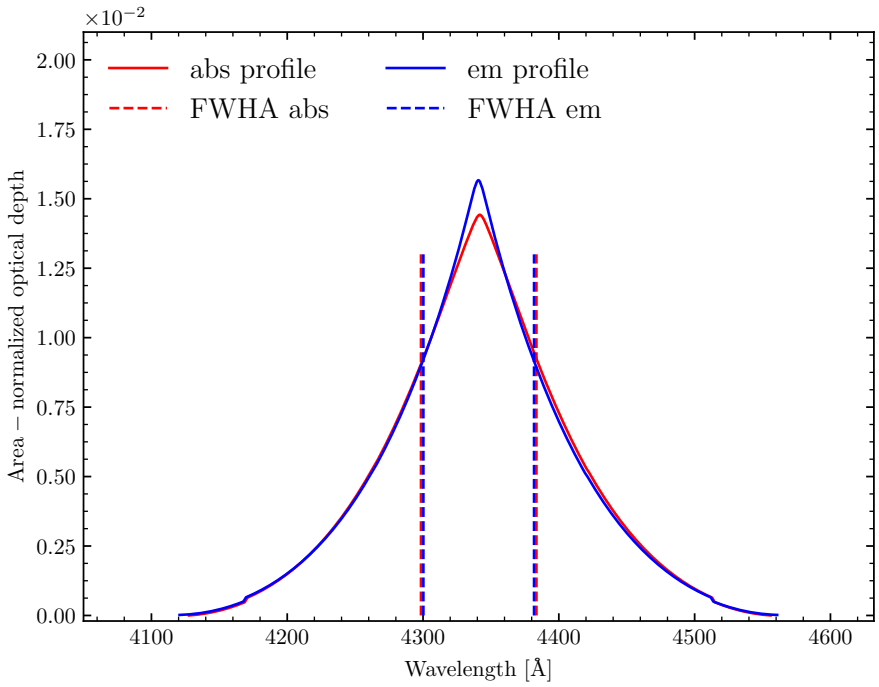

Figure 5.19: Comparison of area-normalized Hγ from Spect3D simulations incorporating the extreme gradients shown in Figs. 5.16 and 5.17. These spectral features were processed according to the description given in E. The two line profiles are in excellent agreement, except for the core, were optical depth and gradient effects become significant. More details are given in the text.

presented in this chapter or (2) the plasma created in the WDPE platform does not adhere to the assumption of complete redistribution.

5.6.3.2 Detailed investigation of the Hβ and Hγ line profiles

The discussion in the previous section highlights that gradients could possibly explain part of the difference I observe in experimentally determined Hβ and Hγ n_e values. I will now explore potential reasons for this behavior.

An obvious starting point for such an investigation is the methodology used to extract the n_e values in the WDPE.

The adopted WDPE method of deriving n_e values from the experimental data relies on the extraction of the individual Hβ and Hγ spectral features. This step is required for *both* the detailed line fit as well as the FWHA method. To extract the individual profiles, I manually define a line-continuum and use the resulting transmission feature to perform an n_e measurement. The hydrogen spectrum resulting from the gradients shown in Figs. 5.16 and 5.17 is plotted as a green line in Fig. 5.20. I also display such manually defined line-continua in that figure. The orange dashed spectrum depicted in Fig. 5.20 represents the emergent spectrum of a uniform 1.35 eV plasma slab at an n_e of $\sim 3.5\times10^{17}\mathrm{cm}^{-3}$. A backlighter at a temperature of 5 eV was assumed for this spectrum. Since instrumental broadening is inconsequential for this investigation (Falcon et al. 2015a), no such parameter was applied to any spectrum shown in Fig. 5.20. For this analysis, I will only use synthetic spectra such as the ones shown in Fig. 5.20 as they enable a much easier investigation of certain data analysis effects. All conclusions I present below should also apply to my experimental spectra.

Different regions of the plasma gradients I show in Figs. 5.16 and 5.17 affect the green spectrum depicted in Fig. 5.20 disparately. This becomes especially evident when I compare the gradient spectrum in that figure (green) to that calculated assuming a uniform 1.35 eV plasma slab (dashed orange), the maximum experimentally determined temperature. From Fig. 5.20, it is

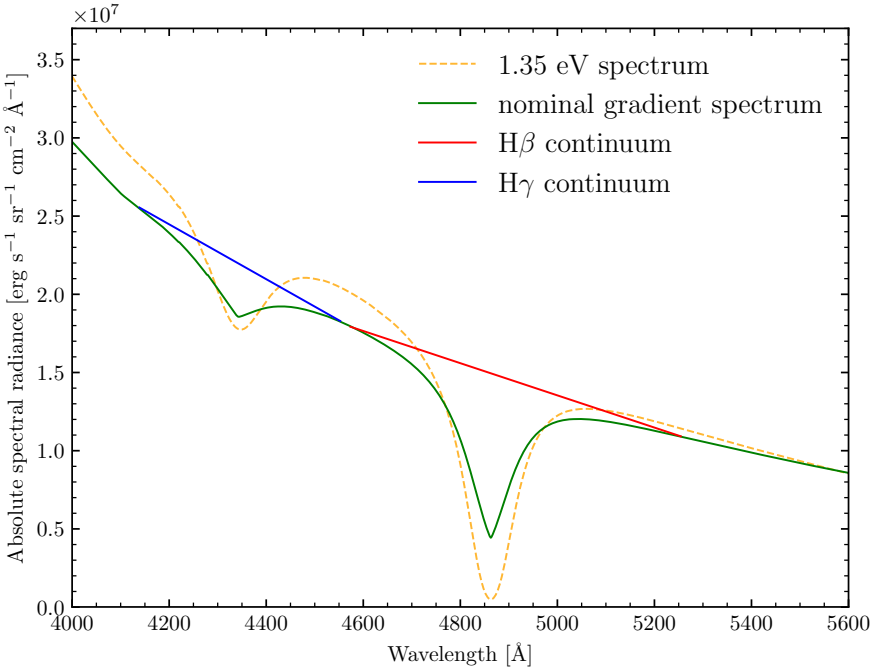

Figure 5.20: A sample synthetic spectrum (green) with all gradients discussed in Sec. 5.6.3.1 applied to them. I also show representative choices for the Hβ (red) and Hγ (blue) continuum regions. The dashed orange line represents a 1.35 eV pure hydrogen spectrum.

obvious that Hβ and Hγ line cores of the gradient spectra are dominated by the low n_e regions at the edge of the gas cell (i.e. the cores are narrower than those of the 1.35 eV lines), while the wings, which are wider than their 1.35 eV counterparts, are controlled by the high n_e regions. It is precisely these high n_e regions that could be responsible for the difference in derived n_e from Hβ and Hγ in the simulated and experimental data . While defining the continuum regions displayed in Fig. 5.20, it is relatively easy to determine the continuum regions on the red edge of Hβ since the next lower line in the spectrum of a

pure hydrogen plasma is Hα (6562.79 Å), more than 1,700 Å away from the center of Hβ. At my experimental n_e and T_e values, the predicted Hα FWHM ranges from ∼11 Å to ∼30 Å (Gigosos & Cardeñoso 1996). I therefore do not expect this line to significantly affect the plasma continuum regions on the red side of Hβ.

The same argument cannot be made for the blue wing of Hβ. Here, a clear overlap between the Hβ blue wing and the red wing of Hγ impedes proper continuum placement (see Fig. 5.21 and associated discussion). In that data region, I thus have no choice but to use the maximum flux between the two lines as a guide for the manual continuum placement procedure. Extracting the true Hγ profile presents me with even greater challenges since this feature is influenced by Hβ on the red side and Hδ on the blue side (see Fig. 5.20). Both the detailed line profile fit method as well as the FWHA method require accurate line profiles. These line overlapping effects could have significant impacts on the derived n_e values and would also affect Hβ and Hγ differently.

To ascertain the influence of these line overlapping effects on the final derived n_e, I perform a simple test. In Fig. 5.21, I show three artificially constructed line profiles: Hβ, Hγ, and Hδ. Each of these spectral features are derived using Xenomorph at the lowest and highest n_e values I derived for my potential plasma gradient shown in Fig. 5.17. Unlike the hydrogen lines shown in Fig. 5.20, the Xenomorph profiles are *not* part of a full spectral calculation and can therefore be used to directly study the influence of line overlapping effects on total line integral, a parameter crucial for both WDPE n_e extraction

methods. Fig. 5.21 shows the Hβ-Hγ overlapping regions in orange, while the Hγ-Hδ regions are shown in purple. Each of the highlighted regions will be removed during the WDPE line normalization method. The reduction of the Hβ line integral resulting from this procedure is minimal, while that of Hγ is severe. Since the wings of the lines are dominated by the high-density regions in the plasma, these line integral reduction effects should decrease in tests with lower density profiles.

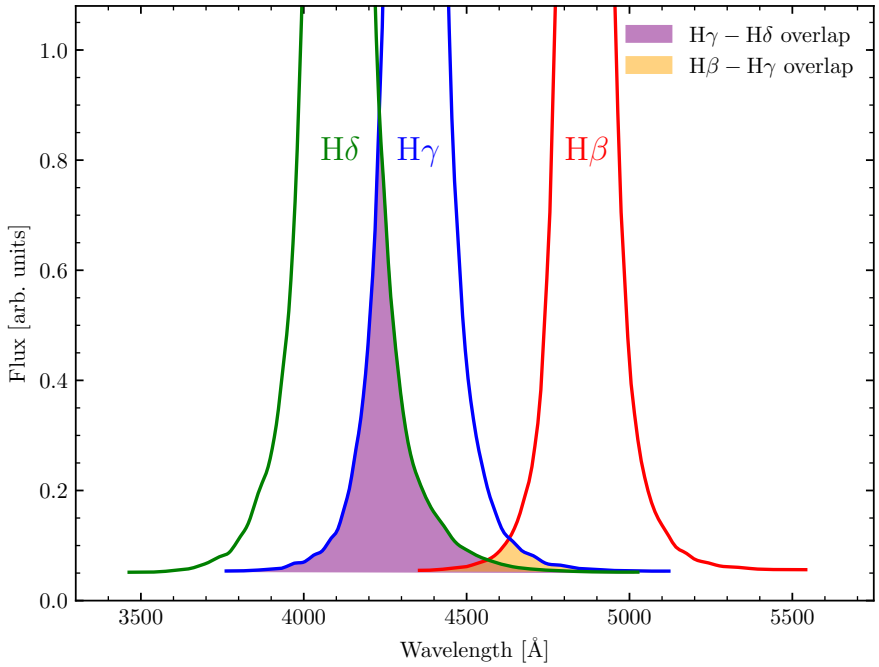

Figure 5.21: Line-overlapping effects for Hβ and Hγ. The plotted line profiles are calculated with Xenomorph assuming the highest and lowest experimental n_e. Clearly, such effects will reduce the total line integral of Hγ more than Hβ. This effect appears to be partly responsible for the observed differences in n_e derived from Hβ and Hγ.

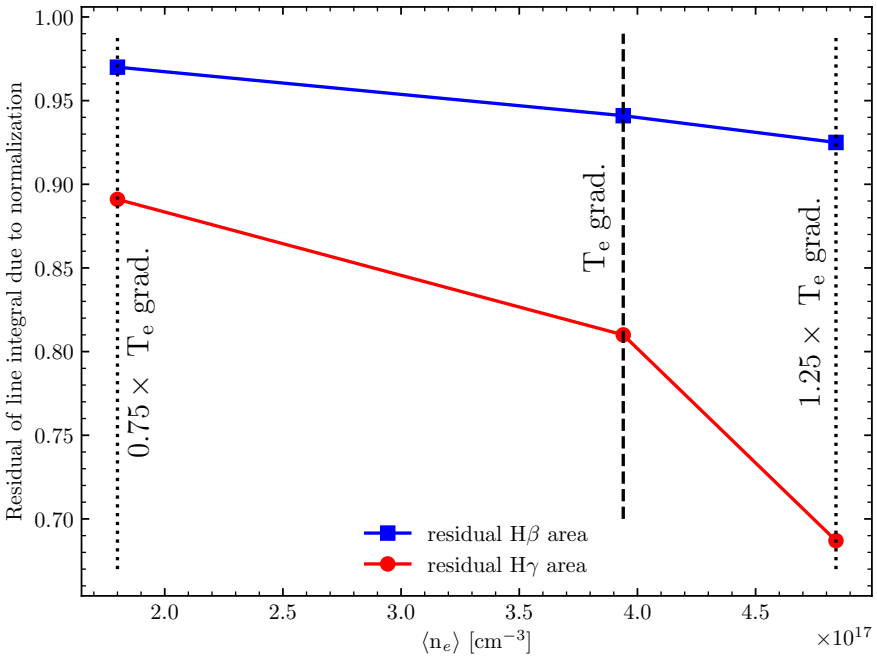

Figure 5.22: Comparison of the residuals of total line integrals of Hβ and Hγ due to $n_{\rm e}$ effects. As expected, the effects on the total normalized line integral of Hβ are very small (7% at most). The effects on Hγ are much more severe, with the highest density Hγ line having its integral reduced by nearly 32%.

Fig. 5.22 depicts the results of this overlapping test at varying densities. In that figure, I show the Hβ (blue) and Hγ (red) residual line integral as a function of adopted plasma $n_{\rm e}$. The residual line integral is defined as the ratio of the line integral with the overlap regions removed (see purple and orange regions in Fig. 5.21) to the total unattenuated integral (red, blue, and green profiles in Fig. 5.21). I also list the gradient scaling factors, which are the multiplicative constants applied to the extreme $T_{\rm e}$ gradients shown in Fig. 5.16 for these testing purposes, on the plot. As expected, the decrease

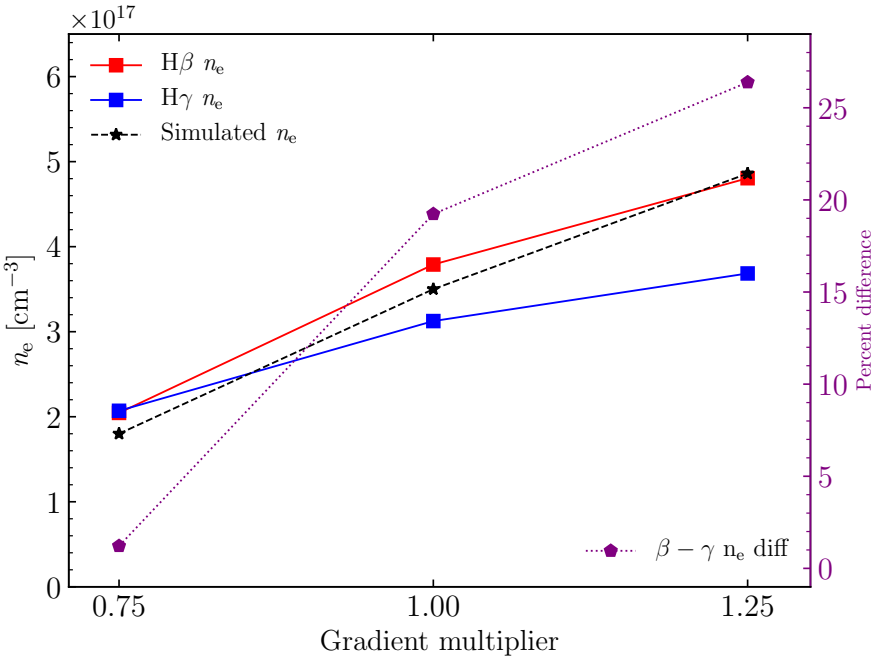

Figure 5.23: Comparison of n_e values derived from Hβ (red) and Hγ (blue) as a function of plasma temperature. The simulated plasma n_e is given as a black dashed line. Percent difference between Hβ and Hγ n_e values is plotted using a purple dotted line. These trends are exactly what is expected based on my understanding of line-overlapping effects.

for the integrated Hγ line profile caused by line-overlapping effects is much more severe than that of Hβ. The Hβ area is reduced by at most 7%, while the Hγ line integral can drop up to 32%. These trends are also reflected in the corresponding Hβ and Hγ $n_e$values, which are shown in Fig. 5.23. In that figure, I also plot the percent difference between the n_e values derived from Hβ and Hγ. The percent difference is calculated as (n_eHβ - n_eHγ) / ((n_eHβ + n_eHγ)/2). Clearly, part of the experimentally determined 40% n_e difference

between Hβ and Hγ can be ascribed to data analysis effects. However, this figure also demonstrates that such effects are only applicable at higher $n_{\rm e}$ values, so gradients and line-overlapping effects *cannot* explain the differences between Hβ and Hγ observed at lower ($n_{\rm e} \lesssim 1{\times}10^{17}{\rm cm}^{-3}$) densities.

5.7 Conclusions

In this chapter, I present a thorough exploration of plasma inhomogeneities in the WDPE platform. Specifically, I investigate whether plasma gradients could possibly explain the difference in $n_{\rm e}$ I infer from my experimental Hβ and Hγ line profiles, as well as the difference in Hγ absorption and emission line shapes (see Sec. 5.4). My discussions in Sec. 5.2 and 5.5 describe details of my hardware design and how they could give rise to potential gradients. I also demonstrate that my hardware design is able to accommodate modest variations in several fundamental aspects of the experimental setup without significantly altering the final plasma parameters.

Using all the information presented in Sec. 5.5, I derive a plasma gradient for the absorption and emission optical paths, the two LOS usually employed in my traditional line-shape approach of extracting plasma parameters (see Ch. 4 and Falcon et al. 2015a,b for more details). Possible influences ranging from the differential heating of the buffers to the impact of the backlighting surface were taken into account. I also present an analysis of the WDPE absorption and continuum data that allowed me to extract a $T_{\rm e}$ and $n_{\rm e}$ gradient along the gold wall, the main heating element in the gas cell. All of these find-

ings are then combined in Sec. 5.6 to show that even though both LOS likely suffer from plasma gradients, they affect each dataset equivalently. My study culminates with Figs. 5.18, 5.19, and Table 5.2 which establish that a combination of plasma gradients and data analysis effects could produce a <20% n_e difference between Hβ and Hγ. This derived n_e disagreement only applies to the higher density data and therefore cannot explain the discrepancy at lower n_e ($\lesssim 1\times10^{17}$cm^{-3}). The mystery of the disagreeing experimental n_e values presented in Sec. 5.4 is therefore still mostly unsolved. However, as mentioned in the introduction to this chapter, such n_e trends have been observed in WD spectra before. Other possible reasons for my experimental disagreement such as fundamental atomic physics effects will be explored in a future publication.

Chapter 6

Helium Shifts and Widths at White Dwarf Photosphere Conditions

The analysis presented in Ch. 5 is focused on issues related to hydrogen in WDs. This chapter covers a completely new class of experiments: those exploring the behavior of helium at white dwarf photosphere conditions. All data presented and analyzed here were collected solely by me. I also led the hardware development efforts aimed at improving the He shift measurement quality. Experiments performed as part of this process are summarized in App. F.

6.1 Scientific motivations of the He experiments

The origin of DB WDs is currently an unsolved problem. Fontaine & Wesemael (1987) first presented a DB evolutionary channel which assumes that the helium and hydrogen WD populations have the same mean mass. The theory presented in that paper is based on the discovery of so-called PG 1159 stars in the Palomar-Green survey (Green et al. 1986). Such stellar objects are almost completely devoid of hydrogen and mainly show He and C in their atmospheres (e.g. Reindl et al. 2015). They also have much higher

temperatures than standard WDs (e.g. Werner et al. 1991, 1996), indicating that PG 1159 stars could potentially represent evolutionary progenitors of hydrogen deficient WDs (e.g. Werner et al. 1991; Kawaler & Bradley 1994; Hügelmeyer et al. 2006; Reindl et al. 2015).

The evolution from PG 1159 to a DB WD is generally explained using observational constraints. The hottest known WDs all have hydrogen dominated atmospheres and start to appear at a $T_{\rm eff}$ of ∼80,000 K (e.g. Barstow et al. 2014). Fontaine & Wesemael (1987) explain this through gravitational settling. The small amounts of hydrogen present in the atmospheres of PG 1159 stars float to the top, while gravity pulls the heavier elements such as helium or carbon towards the bottom. The resulting PG 1159 star then enters the WD evolutionary track as a DA (Liebert et al. 1987). After cooling to a $T_{\rm eff}$ of ∼30,000 K, convection in the atmosphere will be significant enough to mix the outer hydrogen layer with the much more massive helium layer. A DB WD has thus been born. This final convection step is included since from an atomic physics point of view, helium lines in the atmospheres of WDs could be excited at a temperature of ∼45,000 K. A suspicious absence of observed DB WDs in the temperature range from ∼45,000 K to ∼30,000 K necessitates Fontaine & Wesemael (1987) to incorporate this argument.

For this proposed DB evolutionary channel to work correctly, the PG 1159 hydrogen layer mass has to adhere to very strict limits. First, its mass must be high enough to allow for the appearance of hydrogen dominated WDs at temperatures of ∼80,000 K. Second, the total mass of hydrogen also has to

be low enough to enable convective mixing of the hydrogen and helium layers to produce a DB WD at ∼30,000 K (Beauchamp 1995). Third, an optical depth of one has to be reached in this hydrogen layer between WD surface temperatures of ∼30,000 K and ∼80,000 K, further constraining its physical properties. This last condition ensures that the WD will appear to be a DA in that surface temperature range. Simulations show that all of the above hydrogen layer restrictions are only met if its mass in WDs and PG 1159 stars is $\sim 10^{-15}$ $M_{\odot}$ (Eisenstein et al. 2006).

The ratio of known DA to DB WDs is roughly 5:1. According to the evolutionary channel proposed by Fontaine & Wesemael (1987), it should therefore be expected that ∼20% of all hot WDs have hydrogen layer masses comparable to the above value. Unfortunately, asteroseismological observations of variable DA WDs indicate that the majority of all WDs possess a much higher hydrogen layer mass, somewhere around 10^{-4} $M_{\odot}$ (Clemens 1995; Bradley 1998). This much higher hydrogen layer mass agrees with simulations of standard PG 1159 stars. These simulation results should be consumed with caution as stellar mass loss, a very difficult and poorly constrained mechanism, is usually treated at a very elementary level in such PG 1159 models. Nonetheless, it seems unlikely that incorrect treatment of mass loss could explain the eleven order of magnitude hydrogen layer mass difference.

The discovery of 28 DBs with $T_{\rm eff} > 30{,}000$ K by Eisenstein et al. (2006) dealt another blow to the Fontaine & Wesemael (1987) DB evolutionary theory. It thus appears that observed WDs and PG 1159 stars neither have the

required hydrogen layer masses nor the needed surface temperature distribution to entirely fit the Fontaine & Wesemael (1987) model. This evidence casts significant doubt on the evolutionary equivalence of DA and DB WDs. However, it is important to point out that DBs at $T_{\rm eff} > 30{,}000$ K are deficient by a factor of $\sim$2.5 compared to other helium WD populations. Eisenstein et al. (2006) also admit that the current knowledge of DB atmospheres is not nearly as advanced as that of the DAs. In any case, the picture presented by Fontaine & Wesemael (1987) is not as simple as has been claimed in the past.

From the discussion above, it is obvious that other DB evolutionary channels should be explored. The Fontaine & Wesemael (1987) evolutionary model does not attempt to explain the origin of PG 1159 stars. From a theoretical standpoint, the origins of hydrogen deficient post-AGB stars (i.e., PG 1159 stars) has been attributed to a late helium shell flash in these objects (e.g., Herwig et al. 1999; Iben et al. 1983). In such a scenario, the star leaves the AGB and experiences a so-called final thermal pulse. The majority of the atmospheric hydrogen gets mixed in with the still fusing helium convective shell during this pulse (or shell flash). The hydrogen gets burned in the helium layer, leaving behind an extremely hydrogen deficient star. It is currently believed that such a helium shell flash is the evolutionary mechanism for PG 1159 stars, the potential progenitors of DBs (Werner & Herwig 2006). Unlike the scenario proposed by Fontaine & Wesemael (1987), the shell flash scenario does *not* assume that both DA and non-DA progenitor stars have the same initial stellar masses nor that they result in the same mean WD mass. How-

ever, the precise helium shell flash stellar mass signature is currently unknown (Bergeron et al. 2011).

Nather et al. (1981) present another DB evolutionary channel. The authors describe the interacting binary system G61-29. Spectroscopic data collected for that system leads Nather et al. (1981) to conclude that the matter being transferred between the two stellar objects is almost pure helium. Orbital period measurements of G61-29 reveal that the two member stars have a very high mass ratio. Since G61-29 is not a known X-ray source, the higher-mass member of this binary system cannot be a neutron star or black hole. It therefore must be a WD. Orbital dynamics dictate that the lower-mass member of G61-29 has to be either a $\sim$1 $M_{\odot}$ helium-burning star or a $\sim$0.02 $M_{\odot}$ WD. The measured absolute visual magnitude of the system is too low for a helium-burning star, indicating that the lower-mass member of G61-29 also has to be a helium WD. Nather et al. (1981) propose that the mass transfer between the two WDs will never cease leading the member stars to merge into a single stellar object, which would be a DB. It is difficult to speculate about the mass of this single DB WD, but it is likely that the mean mass distribution of the DB population created under such circumstances would not match that of the DAs. A complete list of all currently known interacting helium binary systems can be found in Green et al. (2018).

It should now be obvious that the origin of DB WDs is still an unsettled question. Only one parameter is required to differentiate between the proposed evolutionary scenarios: the mean mass of the DB population. Obtaining that

parameter, however, is much easier said than done. As explained in Ch. 2, serious problems with both the gravitational redshift and spectroscopic mass determination methods for DBs exist. The DB GR measurements suffer from uncertain He I Stark *shifts*, which need to be accounted for to determine helium WD masses using this technique. Applying the spectroscopic method to DBs produces an unexpected log g upturn at low $T_{\rm eff}$ (see Fig. 2.4), which makes the resulting masses inherently suspicious. It is currently believed that the spectroscopic surface gravity increase originates from a potentially flawed implementation of neutral broadening in helium WD atmospheres (e.g., Koester & Kepler 2015). Hence, the two major DB mass determination methods suffer from atomic physics weaknesses. In this chapter, I describe how I use the WDPE platform to investigate these problems. I will first discuss my Stark shift measurements, aimed at solving issues related to the GR mass determination method and then proceed to detail my investigation into neutral broadening.

6.2 Disagreements between existing He I 5876 Å shift measurements and models

Atoms in WD atmospheres, as well as almost all other plasmas, are subjected to electric fields caused by free electrons and ions in the system. Broadened and shifted spectral lines result from such electric fields. This behavior is called the Stark effect. The physical reason for the broadening and shift is conceptually quite simple: when immersed in an electric field,

the atomic energy levels shift. This changes the distribution of electrons in the atom and also removes the degeneracy of the associated energy levels. A schematic representation of the Stark effect's influence on atomic energy levels is depicted in Fig. 6.1. Unfortunately, modeling this behavior in neutral helium is difficult due to issues concerning Debye screening and the role of ions in such calculations (e.g., Büscher et al. 1995).

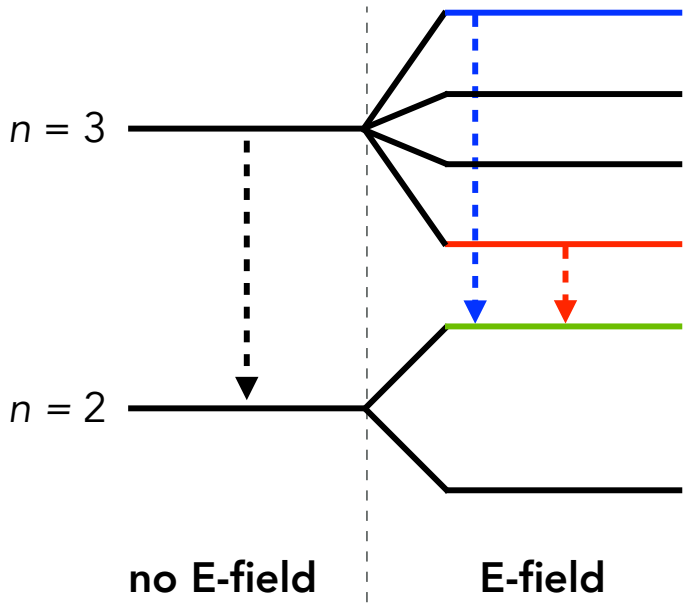

Figure 6.1: A schematic representation of the influence of the Stark effect on atomic energy levels. On the left, I show unperturbed and degenerate energy levels. Once an electric field is applied, the degeneracy is removed and the levels are split. Such a system is depicted on the right ('E-field').

The centroid location of spectral lines is defined by the energy level differences of the involved states. In Fig. 6.1, I show a transition from the n=3 to the n=2 state in an atom. The no E-field case (left) results in a

spectral line location defined by the simple formula:

$$\lambda = \frac{hc}{E_3 - E_2} \tag{6.1}$$

where c is the speed of light, h represents Planck's constant, and E_3 as well as E_2 stand for the respective energy level values. Once an E-field is applied, Eq. 6.1 becomes invalid because the energy levels are now split (see E-field in Fig. 6.1). Depending on the precise energy levels involved in the transition under consideration, an E-field can decrease (red dashed arrow) or increase the energy level difference (blue dashed arrow). In the case of the *lowered* difference, the spectral line will be shifted to *longer* or *redder* wavelengths, while in the case of an *increased* difference, the spectral line will be shifted to *shorter* or *bluer* wavelengths compared to those given by Eq. 6.1. The magnitude of the level splitting shown in Fig. 6.1 is a function of the electric field strength, which in turn, is dependent on the density of free electrons and ions in the plasma. Hence, the shift of a spectral line should change as a function of electron density. These shifts become significant in the atmospheres of WDs and need to be accounted for in the GR mass determination method.

The strongest transition in the optical spectra of low-temperature (1.3 eV $\lesssim T_{\rm e} \lesssim$ 3.75 eV) laboratory and astrophysical helium plasmas is the $2p \rightarrow 3d$ He I feature located at 5875.62 Å. Its lower level ($1s2p$) energy is 20.964 eV, while the upper level ($1s3d$) is at 23.073 eV. Due to the relatively high lower-energy level of this line, the associated state will not be significantly populated and therefore won't produce a spectral feature until the plasma reaches a temperature of ∼15,000 K or ∼1.3 eV. This line becomes very weak above temperatures

of ∼45,000 K or ∼3.75 eV, making it ideal for the determination of the DB population GR mean mass, since it allows the observer to average over a large range of surface temperatures, resulting in a representative value. It is for this precise reason that Falcon et al. (2012) used this transition for their DB GR mass measurements. The authors of that study attempt to place constraints on the shift of He I 5876 Å at DB atmospheric conditions by measuring the wavelength change with respect to Hα. They derive an mean He I 5876 Å shift of $\sim$ -0.13 Å for all the stars in their sample. It is unclear, however, if WDs with pure helium atmospheres have the same evolutionary channel (and therefore mass) as those with a hydrogen-helium mix composition.

The He I 5876 Å transition is also of considerable interest from an atomic physics point of view. For more than six decades, theory and experiment have disagreed on the magnitude and sign of the Stark shift for this particular feature. Griem et al. (1962) performed the first Stark shift calculations for this line by only considering the electron effects on the splitting of the energy levels and the resulting shift. Their calculations made use of the impact approximation to model these electron effects. In this approximation, electrons move very quickly with respect to the perturbed atomic system. Their paths are therefore assumed to be linear or hyperbolic. The electron-atom interaction can then be treated as a collision. This approach is further validated by the fact that the 'collisional' time is much shorter than the time it takes for an electron to transition between two states. The shifts resulting from this treatment are shown in Fig. 6.2 as blue 'x' markers.

Cooper & Oertel (1969) performed the next iteration of Stark shift calculations by including Debye shielding in their calculations. Such shielding occurs because plasmas contain both positive (ions) and negative (electrons) charges that, on average, will reduce their individual local effectiveness. The electric field strength in the vicinity of an atom will therefore be reduced with respect to the pure electron case. Upon the inclusion of shielding effects, the predicted shifts now turn from the slight blueshifted values predicted by Griem et al. (1962) to a moderately increasing redshift as a function of $n_{\rm e}$ (see red pentagons in Fig. 6.2).

Of course, electrons and shielding are not the only effects that produce Stark shifts in spectral lines. Whenever a plasma contains free electrons, they are usually accompanied by free ions and/or protons. Effects of these charged particles on the shift of the He I 5876 Å transition were included over the decades by Griem (1974), Dimitrijevic & Sahal-Brechot (1990), and Gigosos et al. (2014). As evident from Fig. 6.2, these effects lead to increasingly severe blueshifts of He I 5876 Å. It appears that from a theoretical standpoint, the question of the shift of this line is much less settled than that of other He I lines, such as the ones at 5016 Å or 7281 Å (Gigosos et al. 2014), both of which can also be seen in DB, but in much smaller $T_{\rm e}$ ranges than He I 5876 Å.

Theoretical developments in the calculation of the He I 5876 Å Stark shift have been accompanied by experiments aimed at testing the various models and approximations. Berg et al. (1962) were amongst the first such experiments. They used an electromagnetic 20 mm internal diameter shock tube to

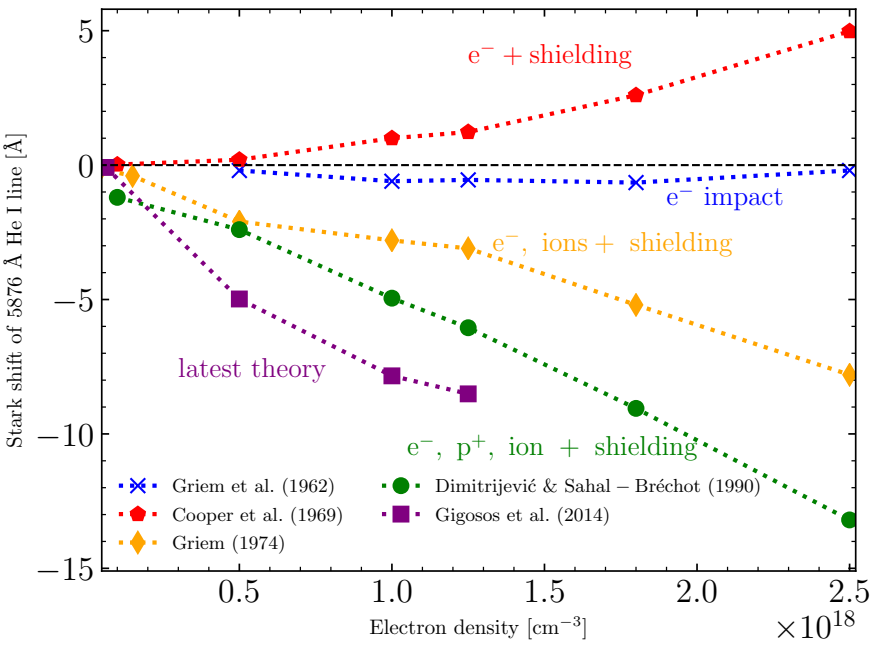

Figure 6.2: The evolution of Stark shift calculations for the He I 5876 transition. Initial calculations (blue x), which included electron effects only, predict a very mild and constant blueshift as a function of n_e. Upon the inclusion of shielding effects, a moderate redshift arises (red pentagons). Incorporating further plasma effects such as ions and protons results in an increasingly severe blueshift for this line (orange diamond, green sphere, purple square).

produce their plasma. Two electrodes are mounted on one end of the shock tube and once they discharge, a shock is launched into the gas-filled tube. This shock front has the potential to ionize the atoms in the gas and hence creates a plasma. Since spectra resulting from the Berg et al. (1962) experimental approach are of very low signal to noise (S/N), many experiments have to be performed repeatedly to obtain a single, usable dataset. The temperatures in the Berg et al. (1962) experiment were determined by line-to-continuum

intensity ratios, while the electron densities were obtained by the continuum ratio of the shock heated plasma and the carbon arc. The T_e and n_e determination methods rely on complicated atomic input data that may or may not be known to the needed degree of accuracy. Berg et al. (1962) report two He I 5876 Å shift measurements, both are in the red direction (black stars in Fig. 6.3). The quoted error on those shift measurements is ±1 Å.

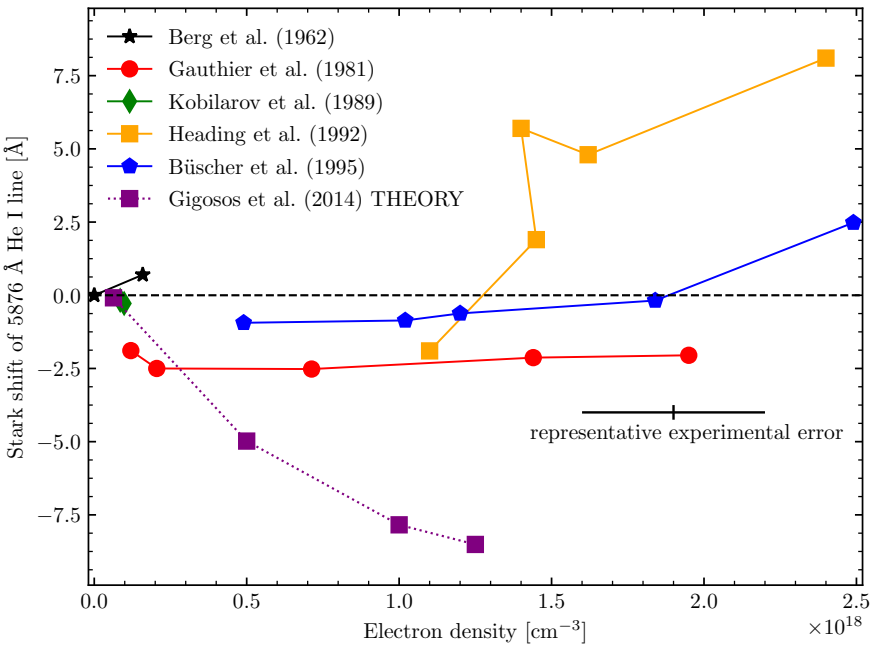

Figure 6.3: Comparison of different experiments aimed at experimentally determining the shift of the He I 5876 Å transition. I also show the latest theory of Gigosos et al. (2014) for comparison purposes. Clearly, all experiments exhibit a large range in measured n_e for this particular line, further highlighting the need for additional experimental and theoretical studies of this line.

Gauthier et al. (1981) performed another He Stark shift experiment that covered a much greater range in n_e than Berg et al. (1962). Their plasma was

created through the use of a CO_2 laser, which deposited ∼1 J of energy into a glass container containing helium gas. Their optical setup recorded the plasma spectrum side-on, necessitating an Abel inversion of the data before any shift measurements could be performed. A crucial assumption for such a procedure is the homogeneity and symmetry of the plasma. Gauthier et al. (1981) provide ample proof for this requirement. Much like Berg et al. (1962), Gauthier et al. (1981) also have to co-add ∼60 spectra to obtain sufficiently high S/N data. Their plasma n_e was determined using the width of the He I 3889 Å line, while their temperature is deduced from the intensity ratios of the He I 3889 Å and 6678 Å lines. I show the results of their experiments as red circles in Fig. 6.3. They derive an almost flat Stark blueshift as a function of n_e for the He I 5876 Å line.

Disagreements in theory and experiments for the He I 5786 Å were already apparent when Kobilarov et al. (1989) published their investigation. They aimed to explore the influence of ion-dynamics on the calculated and measured shift of that line. Their experimental setup consisted of a pulsed arc discharge apparatus within a 13.5 mm diameter glass tube. During a discharge, a continuous flow of either pure helium or various helium-hydrogen and helium-argon mixtures is fed into the tube thereby creating a plasma. N_e values are derived using laser interferometry. T_e is determined using the intensity ratio of O II lines at 4366.9 Å and 4369.3 Å. The n_e determination in this experiment is independent of any atomic models, while the temperature determination again relies on atomic input data. Kobilarov et al. (1989) derive

two shift values for He I 5876 Å (green diamonds, almost indistinguishable, in Fig. 6.3), both of which are slightly blueshifted and agree with the trends observed by Gauthier et al. (1981). The shift errors quoted by Kobilarov et al. (1989) are ∼0.01 Å.

The He I 5786 Å shift measurements published by Heading et al. (1992) are not easily compared to other experiments and theories. The experimental setup of Heading et al. (1992) is very similar to that of Kobilarov et al. (1989) in that they use a pulsed arc discharge and laser interferometry to provide n_e estimates. The diameter of their experimental glass tube is 100 mm. I plot the Heading et al. (1992) results as orange squares in Fig. 6.3. They were the first to measure a transition from blue- to redshift in the He I 5876 Å line, although the precise n_e value at which this changeover occurs is uncertain. However, the line profiles presented in that study exhibit severe asymmetries, which could be indicative of significant inhomogeneities in the plasma. The Heading et al. (1992) results are thus to be consumed with caution.

Büscher et al. (1995) published the latest He I 5876 Å experimental shift study. Their experiments were conducted using a slightly altered arc discharge called a gas-liner pinch. In this gas-liner pinch setup, two gases are used: the driver gas and the test gas. The driver gas, hydrogen in the case of the Büscher et al. (1995) He shift measurements, is heated first by a bank of discharging capacitors. At peak compression, the test gas, which was chosen to be helium, is then inserted into the center of the gas vessel, where it is then heated by the surrounding driver gas (Finken & Ackermann 1981, 1982). It

has been demonstrated that such a setup results in a very uniform test gas plasma with low optical depths (Glenzer et al. 1992). Büscher et al. (1995) use optical Thompson scattering to determine plasma n_e and T_e values. The shift measurements reported in this publication are plotted as blue pentagon in Fig. 6.3. Like Heading et al. (1992), Büscher et al. (1995) also derive a transition from blue to red in the shift of He I 5876 Å, but do so at a much higher n_e and measure a much more gradual transition. Shift errors quoted by Büscher et al. (1995) are $\sim$0.008 Å.

The discussion above highlights both theoretical and experimental challenges associated with the He I 5876 Å Stark shift predictions and measurement. Potential weaknesses in theoretical models include the number of states included in the calculations (Heading et al. 1992), incorrect implementation of Debye shielding (Büscher et al. 1995), or, since the cited calculations use semi-classical approximations, the absence of quantum effects. Experimental disagreements can be traced to several potential effects. All experiments listed above were performed in emission, except for Gauthier et al. (1981), who also attempted to perform experiments in absorption. However, the reported shift values are obtained from their emission data. One potential source of disagreement could therefore be the optical depths of the lines. Most experimenters went to great lengths to ensure the collection of optically thin He I 5876 Å emission features. However, how important is such an effect? Since I collect both absorption *and* emission at the same time, I could investigate whether such considerations can explain the differences between the different experi-

ments as well as experiments and theory.

Another potential source of disagreements between experiments stems from the co-addition of as multiple datasets (up to 60 in the case of Gauthier et al. 1981, 10 for Büscher et al. 1995) to derive a shift measurement. An implicit assumption made during this process is high experimental reproducibility. If such co-additions are not performed carefully, they could potentially result in uncertain Stark shift measurements. As I demonstrate in a later section of this chapter, the WDPE produces very high S/N spectra in a single experiment so I do *not* have to rely on co-added spectra to infer my n_e and He I 5876 Å shift values.

The final potential sources of experimental disagreements are Doppler shifts and plasma non-uniformities. Berg et al. (1962) and Kobilarov et al. (1989) adopted an approach during which the plasma was in motion as the data was collected. Such motion could potentially influence the peak location of the He I 5876 Å line. In the WDPE, the plasma is at rest for the duration of the experiment. Doppler shifts are therefore of no concern in my measurements. Plasma inhomogeneities for pure hydrogen plasmas in the WDPE were thoroughly investigated in Ch. 5 of this thesis and found to be negligible. It is reasonable to assume that such an analysis extends to He I 5876 Å line. Taking all these considerations into account, the WDPE is in an ideal position to re-examine the question of the He I 5876 Å shift measurements measurement and thereby explore experiment-theory disagreement, as well as the experiment-experiment variance.

As a final point in this section, I briefly comment on plasma parameter determination methods. Some of the experiments I discussed above employ independent plasma diagnostics to derive n_e and/or T_e (e.g. Büscher et al. 1995), which results in errors of $\pm 15\%$. The majority of studies, however, use spectral lines as diagnostics, which may be unreliable due to unknown or unconfirmed atomic input data. Such an approach may lead to $\pm 20\%$ errors in derived n_e and T_e. The WDPE was initially designed to study hydrogen line profiles (e.g. Falcon et al. 2013; Montgomery et al. 2015). In Ch. 5, I present a thorough investigation into the behavior of Hβ in my platform. I conclude that this line is a very reliable n_e and T_e diagnostic with errors estimated to be at the $\pm 10\%$ level. The majority of the uncertainty results from the line normalization needed for the n_e and T_e extraction. See App. E for more information. My He I 5876 Å Stark shift measurements therefore have the potential to be more accurate than those of previous experiments.

6.3 Initial attempts at an He shift measurement

The two most important components of a successful shift measurement are an accurate n_e diagnostic and a high-resolution/high S/N spectral dataset. The WDPE platform should be able to fulfill both of those requirements. My initial He Stark shift experiments indicated, however, that changes to the WDPE design as well as the data collection methods were needed before a successful measurement could be performed. The required updates as well as my initial shift measurements are described in this section.

The initial He shift experiments were performed with the standard WDPE setup presented in Sec. 3.2. Since the scientific goal has now evolved to measuring the Stark shift of He I 5876 Å as a function of n_e, a density diagnostic is needed. The work presented in Ch. 5 provides clear motivation to use Hβ for that purpose. All He shift experiments presented in this current chapter were therefore performed with a 50/50 molar H_2/He gas mixture. It has been shown that the presence of helium or other elements in a plasma being used to perform He I 5876 Å Stark shift measurements does not influence the shift measurement or n_e diagnosis, making a H_2/He gas mixture the ideal choice for these experiments (Kobilarov et al. 1989; Büscher et al. 1995; Kunze 2009). In addition to the low-resolution film data that was captured for the analysis in Ch. 5, I now also record two high-resolution spectra of the He I 5876 Å transition. The film data (see Fig. 4.2), which contain the Hβ line, are used for plasma parameter extraction purposes, while the CCD data (see Figs. 4.13 and 4.14) are utilized for the Stark shift measurements.

Collecting four instead of two datasets per shot requires an updated data-acquisition approach that delivers sufficient signal to four cameras. A fiber splitter attached to the standard single-core in-chamber fiber (see Ch. 4 and Fig. 4.1) is an obvious solution to this problem. Unfortunately, tests showed that the inclusion of a fiber splitter in the optical path reduced the signal arriving at the cameras by at least 70%. Such a low signal would be undetectable for both the film and CCD systems. Another relatively simple option consists of using a fiber bundle instead of a single-core in-chamber

fiber. I chose a dual-core bundle with one 105 μm and one 200 μm core fiber (see Sec. 4.1) for the initial He shift experiments. The smaller diameter fiber is used to collect the low-resolution, plasma diagnostic film data, while the signal transported in the 200 μm diameter fiber results in the high-resolution He shift CCD data. This fiber bundle is the only change in the WDPE setup or hardware adopted for the initial He shift experiments.

Scoping experiments performed at the 10 mm LOS did not produce any helium lines in the experimental spectra. I therefore decided to perform all initial He shift experiments at 5 mm from the WDPE gold wall radiation source to ensure that both the n=3 and n=2 levels in helium have sufficient population to produce emission and absorption lines. I learned later that the 5 mm LOS is not ideal for He shift measurements due to the large gradients caused by the proximity to the gold wall. Additionally, the entire line of reasoning leading to that decision was incorrect since the He scoping experiments at the 10 mm LOS contained an incorrect gas fill, not the helium I had requested. All final, definitive He shift shots (see Sec. 6.4.5 and bottom panel of Fig. 6.4) were performed at the 10 mm LOS. The 5 mm shots did, however, provide me with valuable information about the influence of boundary layer plasmas on my recorded line profiles as well as test data to develop my shift extraction software. More details about these aspects are given below.

First issues with the initial He shift data collected at the 5 mm LOS arose upon analysis of the high-resolution CCD absorption spectra. I show the time-evolution of this dataset in the top panel of Fig. 6.4. The absorption

data behaves just as expected at 0 ns (red) and 60 ns (blue). At later times, the He I 5876 Å absorption feature appears to transform into an emission line (120 ns (green) and 180 ns (yellow)). Such helium absorption-emission transformations were also observed in all other initial 5 mm LOS H_2/He experiments performed using the standard WDPE setup.

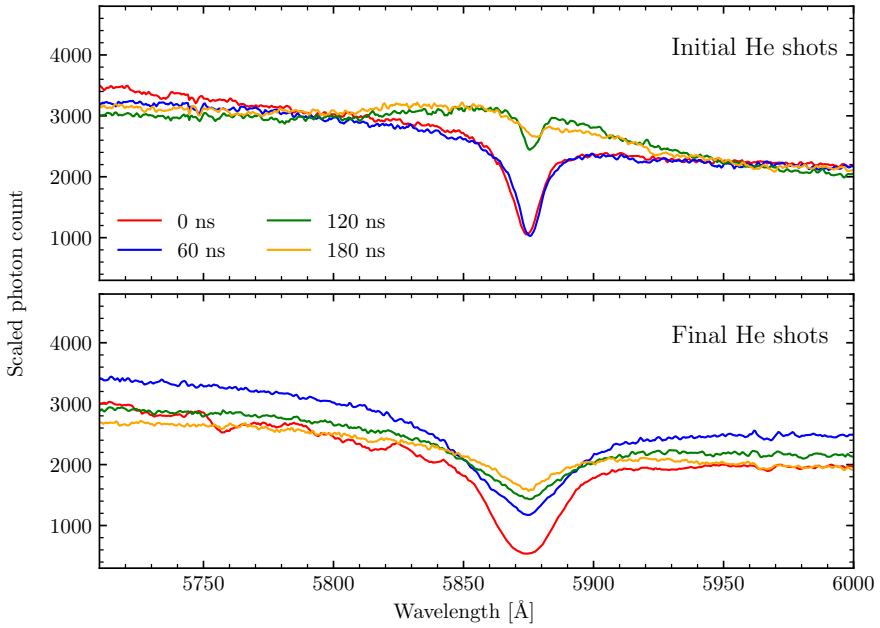

Figure 6.4: Time evolution of z3093 (top panel), and z3195 (bottom panel) He I 5876 Å absorption data. The z3093 spectra (top panel) show absorption at early times (0 and 60 ns), which, at later times appears to turn into emission. I observed such behavior in several other initial H_2/He shots as well. Shot z3195, which is plotted in the bottom panel, represents the final He shift data that was obtained with the updated experimental platform. As mentioned in the text, these high-resolution CCD data are collected using the 200 μm core fiber.

The inclusion of a fiber bundle was the only major change in the initial

H_2/He shots with respect to the standard H experiments discussed in Ch. 5. A logical starting point for a potential cause of the effects observed in the top panel of Fig. 6.4 is thus the updated WDPE optical setup. Two potential issues could arise from the fiber bundle: (1) the interaction of the fiber bundle beam diameters with the 5 mm apertures (2) absorption measurements may now be more difficult since the total area beam diameter at the location of the backlighter may exceed the size of the heated portion of that piece of hardware. Each of these problems is caused by the fact that the initial WDPE cell design was developed for a single 100 μm fiber, while the bundle contains one 105 μm fiber and one 200 μm fiber.

The most critical point in the absorption and emission optical path is the 5 mm aperture shown in Fig. 5.2. The absorption LOS passes through one of these apertures when entering the cell (see blue line in Fig. 3.9), while the emission LOS passes through two such apertures when entering and exiting the cell (see green line in Fig. 3.9). In the standard hydrogen experiments, I use a beam profiler (see Sec. 4.2.3) to measure the beam diameter of the standard 100 μm-core fiber at the locations of the apertures along the optical path. Such tests ensure $\sim$2 mm clearance between the collection beam and the 5 mm aperture. I repeated this beam diameter measurement with the bundles containing 105 μm-core and 200 μm-core fibers. Fig. 6.5 shows the results of these measurements as a function of distance from the fiber end. The 'initial' labels for the beam (dashed red) and aperture diameters (5 mm, horizontal black dotted) in that figure refer to those used during the collection

of the initial He shift data presented in the middle panel of Fig. 6.4. The altered beam (solid blue) and aperture diameters (6 mm, again horizontal black dotted), which were adopted to correct shortcomings in the initial He shift data, are labeled 'final' in Fig. 6.5. Additionally, I also show the locations of these apertures as well as the backlighter (see Fig. 5.2) along the each LOS as vertical black dashed lines. All these aspects will be discussed in the following paragraphs.

Inspection of Fig. 6.5 immediately reveals major problems with the 200 μm fiber beam diameters (red and blue dots) for both the absorption and emission optical path. The beam diameters measure $\sim$3.2 mm at the location of the first aperture ($\sim$50 mm from the fiber end) and $\sim$4.8 mm at the location of the second ($\sim$190 mm from the fiber end). For the collection of the initial He shift data (Fig. 6.4, middle panel), these apertures had a 5.0 mm diameter, making the proximity of the 200 μm fiber collection beam diameter to the second aperture problematic, since additional photons from this hot aperture could potentially contaminate the emission data. Only the emission LOS will suffer from this design flaw (see description of optical path in previous paragraph).

The absorption optical path suffers from beam diameter issues relating to the backlighting surface. As explained in Ch. 5, WDPE absorption measurements are possible since the backlighter is *hotter* than the plasma. The late-time data (120 ns and 180 ns) presented in the middle panel of Fig. 6.4 indicates that the self-emission of the plasma is now able to overcome the

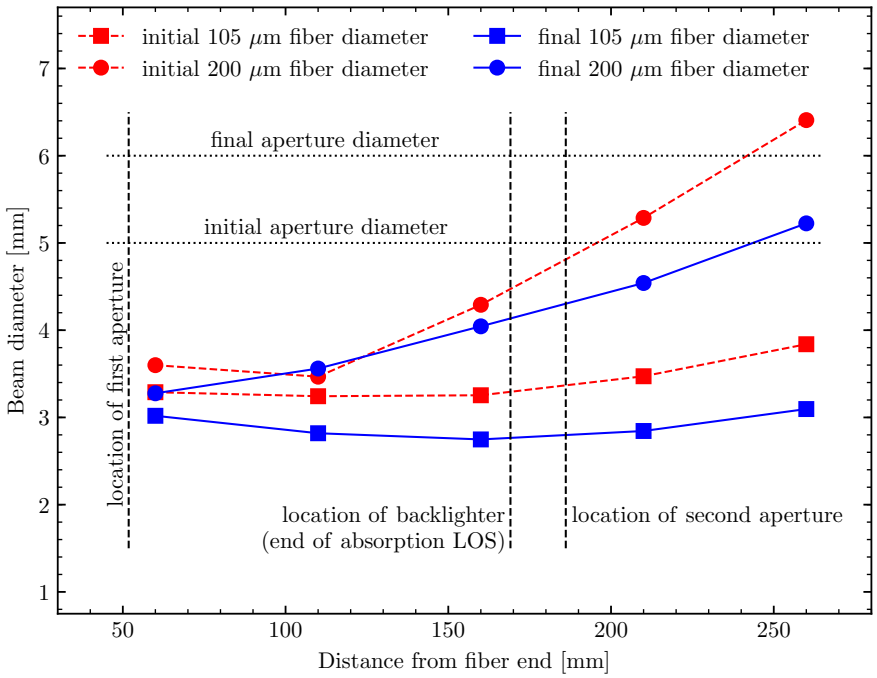

Figure 6.5: Representative beam diameter measurements as function of distance from the fiber end. The beam diameters adopted for the collection of initial He shift data (middle panel Fig. 6.4) are shown in red (square - 105 μm core, dot - 200 μm core). The final beam diameters, which were used to the collection of the final He shift data (bottom panel of Fig. 6.4) are plotted in blue. I also indicate the locations of the two apertures as vertical dashed lines as well as their initial and final aperture diameters (horizontal black dotted lines). See text for further details.

backlighting surface radiation. However, this is merely an effect caused by the usage of a fiber bundle for the collection of the absorption data. Fig. 6.6 shows the interaction of the backlighting surface with the absorption LOS fiber bundle. The part of the backlighting surface directly heated by the Z-pinch has a height of $\sim$4.8 mm. The initial He shift absorption data was collected

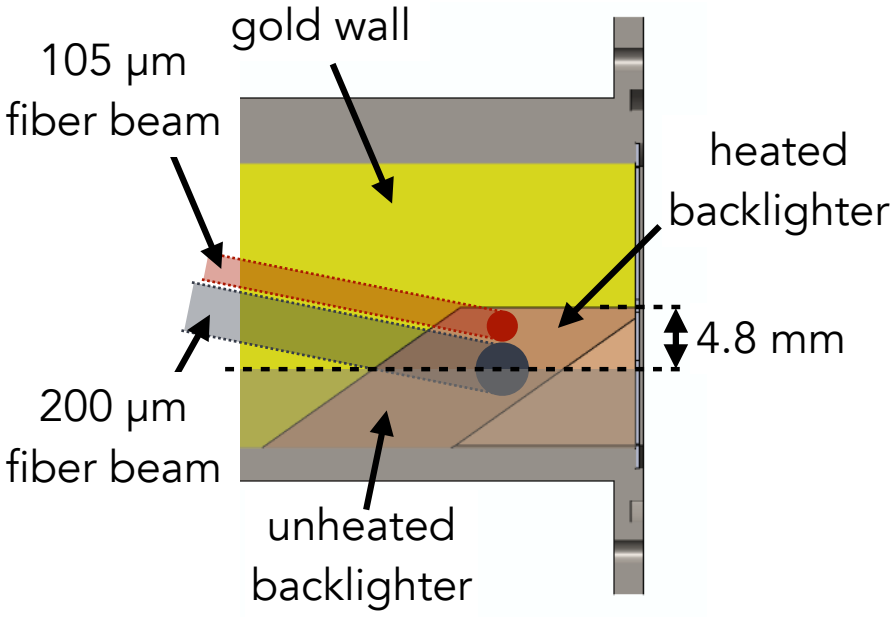

Figure 6.6: Schematic view of the backlighting surface and its interaction with the absorption fiber bundle diameters. I show the diameters of the 105 μm and 200 μm fiber beams on the backlighter. In a top-to-bottom fiber arrangement, the 200 μm core fiber will be exposed to the unheated portion of the backlighter (labeled dark grey area). I believe that this fiber arrangement is responsible for the absorption-emission transition observed in Fig. 6.4.

by aligning the 105 μm and 200 μm fibers top-to-bottom on the backlighter. The total beam diameter of the absorption fiber bundle at the location of the backlighter is $\sim$7.8 mm ($\sim$3.30 mm for the 105 μm fiber and $\sim$4.5 mm for the 200 μm fiber, see red dashed in Fig. 6.5). Hence, one of the fibers (in the case of the initial He shift data, the 200 μm core) will be exposed to a part of the backlighter not directly heated by the Z-pinch (see Fig. 6.6). This unheated surface will have a much lower temperature resulting in the data turning from absorption to emission, just like in Fig. 6.5.

An obvious solution to this issue is side-by-side arrangement of the fibers. However, if such a strategy is pursued, one fiber will be closer to the gold wall than the other by ∼2.29 mm. As mentioned in Sec. 3.2, the observed plasma n_e values can be varied by changing the distance between the LOS and the gold wall. Simulations and experiments have shown that at the 5 mm LOS, a difference of 2.29 mm in distance from the gold wall can result in n_e changes as large as 0.5×10^{17} cm^{-3} (Falcon 2014). Thus, the 105 μm core fiber, which is used to collect the plasma diagnostics data on film, probes *very* different n_e regions than the 200 μm core fiber that records the density dependent He shift spectra if such measurements are performed with a side-by-side fiber arrangement at 5 mm from the gold wall.

Given the problems outlined above, the 5 mm LOS is less suitable for He shift measurements. Additional scoping experiments that contained helium gas showed that He can also be excited at the 10 mm LOS. Side-by-side alignment of the fibers at the 10 mm LOS is inconsequential since the n_e and T_e values do not vary significantly ($\pm5\%$) at that distance from the gold wall. This is confirmed by simulations and experiments (Falcon 2014). The n_e diagnostic problem is thus solved at the 10 mm LOS as both the 105 μm core fiber plasma diagnostic data and the He shift spectra collected by the 200 μm core fiber receive data from similar density environments. However, more clearance between the final 5 mm aperture and the 200 μm fiber beam diameter in the emission LOS is still required. This is easily achieved by making slight adjustments to the collecting lens identified in Fig. 4.1. In addition to decreasing

the beam diameter, I also increased the aperture diameter on the emission side to 6 mm (label 'final aperture diameter' in Fig. 6.5). The combination of these two changes ensures sufficient clearance between the emission LOS beam diameter and the final aperture. With these hardware updates, I am now in a position to perform accurate and reliable He shift measurements, the results of which are shown in the bottom panel of Fig. 6.4.

6.4 He shift shots with the updated WDPE platform

Implementation of the hardware and data collection updates described in the previous section allow for the execution of accurate and reliable He shift measurements. A quantitive analysis of these updates is given in this section. In addition to an n_e diagnostic, another crucial ingredient of a shift measurement is the wavelength calibration of the instrument used to collect the experimental data. A T_e diagnostic is also needed but since the shift only weakly depends on this parameter, I consider it to be of secondary importance. In the following sections, I will first focus on the wavelength calibration of the CCD instruments before then discussing the n_e and T_e diagnostics.

6.4.1 Wavelength calibration of the CCD camera systems

A broad overview of the CCD wavelength calibration methods are given in Sec. 4.3. Here, I provide a more in-depth discussion of the CCD wavelength calibration methodology. The data presented and discussed below was collected using a 300 g/mm grating, which allows for a more accurate wavelength

calibration since more laser lines can be included in the dispersion fits.

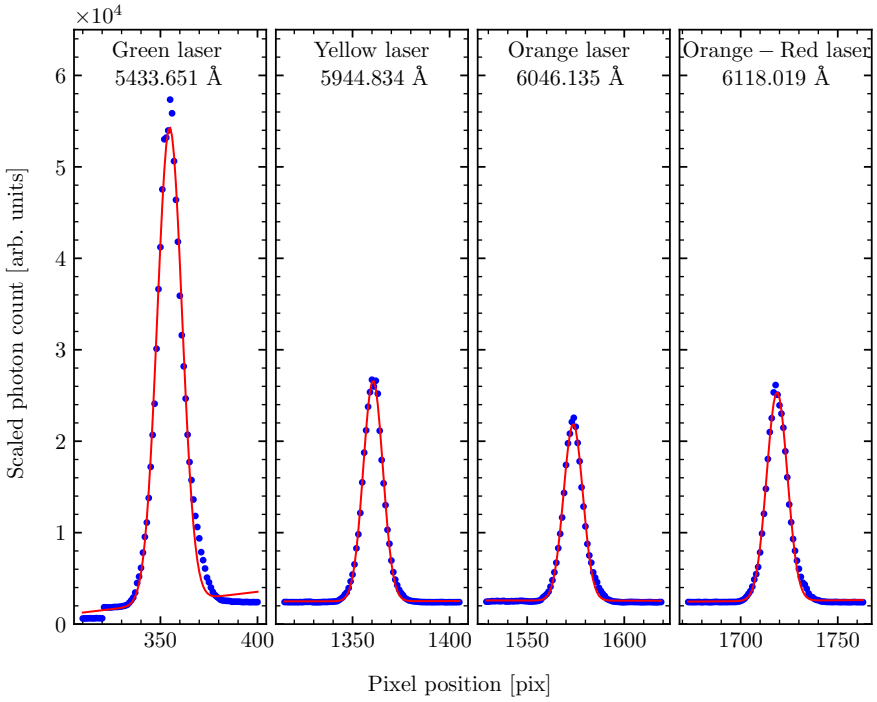

Figure 6.7: Fits of Gaussian profiles to laser lines used for calibration purposes. The green laser line is from the standalone Melles Griot LGR 193 laser (see App. B), while the yellow, orange, and orange-red lasers were produced using the REO 30602 laser (see App. B). Despite the fact that these are 1 ns integrations, each laser produces ample signal for fitting purposes. The centers defined by the Gauss fit are used for wavelength calibration purposes.

Extracting a wavelength calibration from the laser lines shown in Fig. 6.7 requires multiple steps. The laser line CCD image is integrated over two pixel rows in the y-direction and then processed. To minimize the influence of uncertain pixel values on the peak location of the laser line, I fit each profile with a Gaussian (see Fig. 6.7). While the fits to the laser profiles shown in Fig. 6.7

do not appear to reproduce their centers, tests have shown that the centroid of the Gaussian fit is not influenced by such uncertain pixel values, but matches the FWHM center of the laser profile to within $\sim 5 \times 10^{-4}$. Therefore, these Gaussian fits are ideal for deriving the *true* center of the laser lines. The resulting fitted centroids in combination with the corresponding laser wavelength are then used to calculate a wavelength dispersion across the CCD. The panels in Fig. 6.8 depict each individual laser-line-center and wavelength combination, along with the resulting first- (red solid) and second-order (green dashed) wavelength dispersion when all four points are fit simultaneously. I also list the respective sum of squared residuals. The second order fit clearly produces smaller residuals than the first order fit and delivers more accurate results. I therefore adopt the second order fit for wavelength calibration purposes. The validity of this assumption was tested using spectra of a slow-swept Hg-Ne lamp image containing 13 spectral features that can also be used for wavelength calibrations. In the first iteration of this test, I derive a second-order wavelength dispersion from lamp lines in close wavelength proximity to the laser lines shown in Fig. 6.7. Successive iterations of this test then included more and more lamp lines in the wavelength dispersion fit. The order of the polynomial used to derive the dispersion was kept constant. The dispersions derived using more than four datapoints differed by ~ 0.1 Å from the initial iteration. In the laser line only case, the dispersion error is also ~ 0.1 Å, so no significant change in the wavelength dispersion is expected if more laser lines were present. Fitting all lamp lines with increasingly higher polynomials also

did not result in significant changes to the wavelength dispersion.

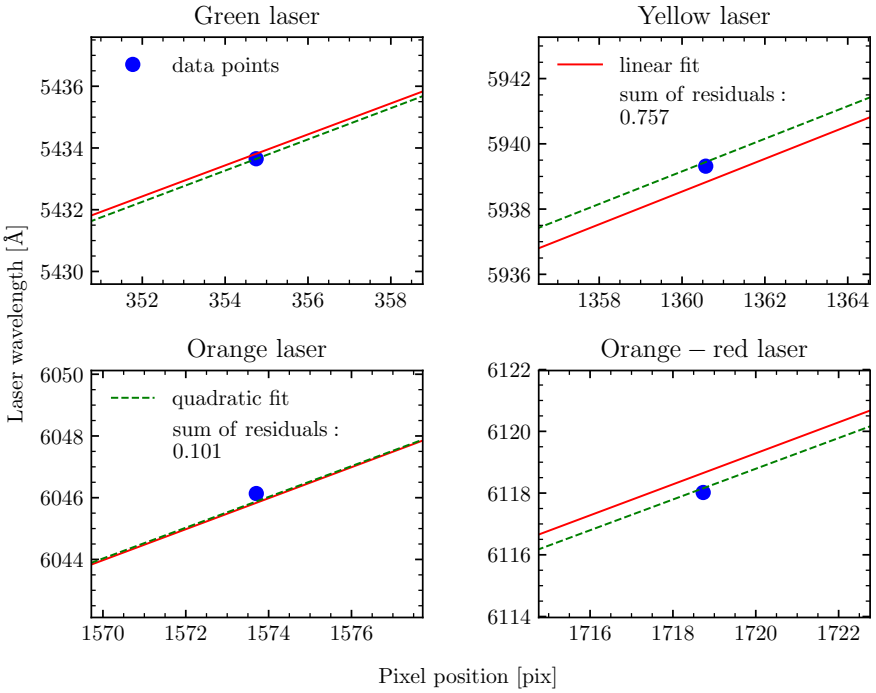

Figure 6.8: Wavelength dispersion across the CCD derived using the Gaussian fits shown in Fig. 6.7. I show each laser center-wavelength combination individually as well as a first- (red solid) and second order (green dashed) fit to all datapoints simultaneously. The second order fit is clearly superior.

As a final note in this section, I briefly discuss the derivation of my wavelength calibration errors. They consist of:

- error in fit Gauss peak (±0.05 - 0.1 Å)
- error in dispersion caused by error in Gauss peak (±0.05 - 0.1 Å)
- error between fit and actual wavelength of laser (±5×10^{-5} - 0.2 Å)

I list the minimum and maximum ranges for each error in parenthesis above. These errors are added in quadrature to give a final, combined wavelength error of ∼0.1 - 0.5 Å, depending on the specific lineout. This final error is about a factor of 2-5 larger than those of previous experiments, but they are still well within the limits required to differentiate between different theories and experiments.

6.4.2 The influence of distortion on the wavelength calibration

As explained in Sec. 4.3, all data collected with the CCD systems suffer from distortions. These can be accounted for in the SMASH data analysis library using a so-called geometric calibration image, which contains a series of isopoints (Dolan et al. 2016). In the following description of the distortion correction algorithm, I refer to the distorted image grid using $x-y$ coordinates while the undistorted (or distortion corrected) image is referenced using $r-s$ identifiers. The isopoints are used to define a so-called isomesh. This isomesh serves as the basis for the distortion correction and is defined as follows: first, the transformation origin of the entire image is defined as the centermost isopoint of the $x-y$ grid. The origin of the $r-s$ system is also set at this centermost isopoint. The path of the r axis is defined along the isopoint central group, while the s axis path is defined by the shortest distance from the centermost isopoint to an isopoint in an adjacent group. Once the path of the r=0 and s=0 lines have been defined in the distorted coordinate system, the arc length of each isopoint on those axes is calculated. The resulting distances

define the isopoint locations in the $r - s$ (i.e. undistorted) coordinate system. Once the undistorted isopoints have been defined, a transformation mesh for each isopoint can be derived. Transforming an isopoint located in the distorted $x - y$ grid to the undistorted $r - s$ grid requires the following transformations:

$$r = a + bx + cy + dxy \tag{6.2}$$

$$s = e + fx + gy + hxy \tag{6.3}$$

In Eqs. 6.2 and 6.3, parameters $a-h$ are derived using the four nearest isopoints in the $x - y$ and $r - s$ coordinate systems. Once such a transformation has been performed on all isopoints, geometric distortions have been removed from the image.

A measure of the distortion correction accuracy can be determined from laser line peak intensity locations. Since lasers have a single, well-defined wavelength, they should trace out perfectly straight lines across the CCD. Fig. 4.15 reveals that in the uncorrected laser image, this does not appear to be the case. Application of the distortion correction algorithm to that laser image should fix the issue. Fig. 6.9 shows a comparison of distorted (dotted) and distortion corrected (solid) peak laser intensity locations as a function of experiment time (i.e., x location on the CCD). The usual experiment time range I use for the He I shift measurements are marked grey in that figure. In all cases except the green laser, the distortion correction merely translates the location of the laser, but does not significantly change the trend of the location as a function of time. This indicates that CCD data distortions in

the vicinity of the spectra line under consideration (He I 5876 Å, close to the yellow laser at 5944.83 Å) are not severe.

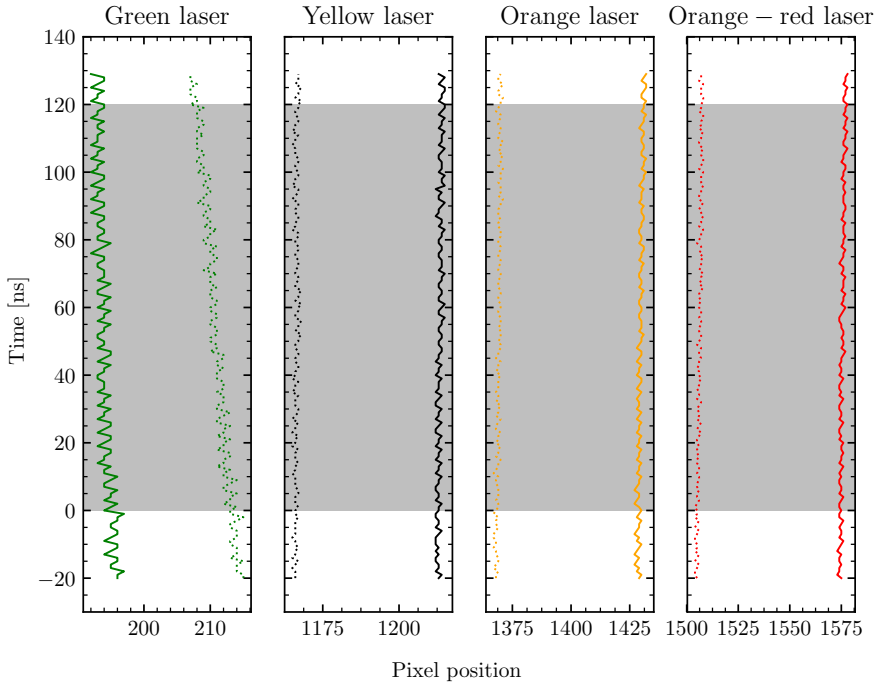

Figure 6.9: The peak positions of the laser lines used for wavelength calibration purposes as a function of experiment time. The dotted lines show the locations in the distorted image and the solid lines show the peak locations once the correction has been applied. For all laser lines, except the green, the distortion correction merely translates the position of the laser but does not appear to change the position of the laser as a function of time. The experimental times considered in the WDPE are highlighted in grey. The green laser is located at 5433 Å, the wavelength of the orange laser is 5944 Å, the orange laser has a wavelength of 6046 Å, while the orange-red laser is at 6118 Å. More information can be found in App. B.

The severity of the data distortion can also be ascertained by determining the difference between the distorted and distortion corrected laser po-

sitions. Fig. 6.10 shows these difference values as a function of experiment time. The data plotted in that figure was derived by performing 20 ns integrations of the fiducial image. The data again indicates that the distortion correction merely changes the lateral position of laser lines, but not their position as a function of time on the CCD. Even in the case of the green laser line, the trends as a function of time are small. The maximum standard deviation of the green laser position over 20 ns (time integration window for the WDPE He I shift measurements) is ∼1.2 Å, which translates to change in the derived wavelength for each pixel by ∼0.55 Å. This value is comparable to the largest derived experimental error (see above). The difference between the wavelength calibration performed with and without distortion correction of the laser and data images is discussed in Sec. 6.4.5.

6.4.3 n_e determination in H_2/He mixture plasmas

A successful Stark shift measurement also requires an accurate n_e diagnostic. I employ the FWHA approach outlined in Ch. 5 and App. E for this purpose. A fundamental question that has to be asked is whether the presence of helium changes the plasma n_e values as compared to the pure hydrogen case. Deriving FWHA n_e values for pure hydrogen and H_2/He mix plasmas is one way to answer this question.

Fig. 6.11 shows the FWHA n_e trends for three different experiments: the standard hydrogen experiment z2553 (red, Falcon et al. 2015b), z3193 (green), and z3195 (orange), both of which are H_2/He mix experiments. Setup

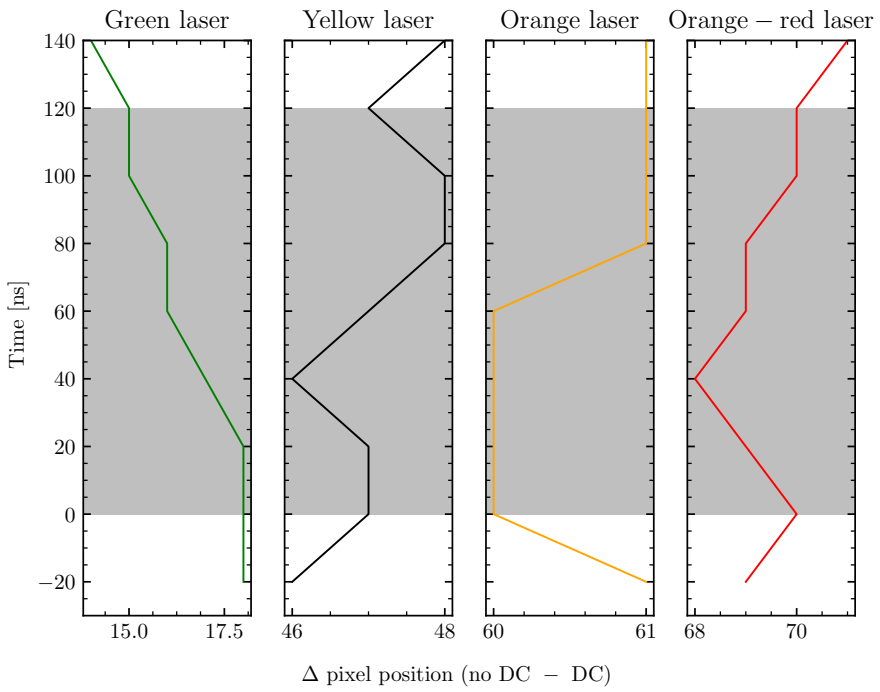

Figure 6.10: Difference in peak laser positions for the undistorted (DC) and distorted (no DC) laser calibration images in 20 ns integrals. For every image except the green laser, the corrections are lateral only, indicating again that distortions in the vicinity of He I 5876Å are not severe. The green laser is located at 5433 Å, the wavelength of the orange laser is 5944 Å, the orange laser has a wavelength of 6046 Å, while the orange-red laser is at 6118 Å. More information can be found in App. B.

data for all these shots is listed in Table 6.1. Based on Fig. 5.9 and associated discussion, I estimate the FWHA n_e measurement error to be ±10%. A brief look at Fig. 6.11 reveals that all three shots produce comparable n_e trends. This seems to indicate that the addition of He to the gas mixture does not significantly change plasma n_e. Simulations that assume the 'realistic' plasma T_e gradient shown in Figs. 5.16 confirm that ∼95% of all He atoms present

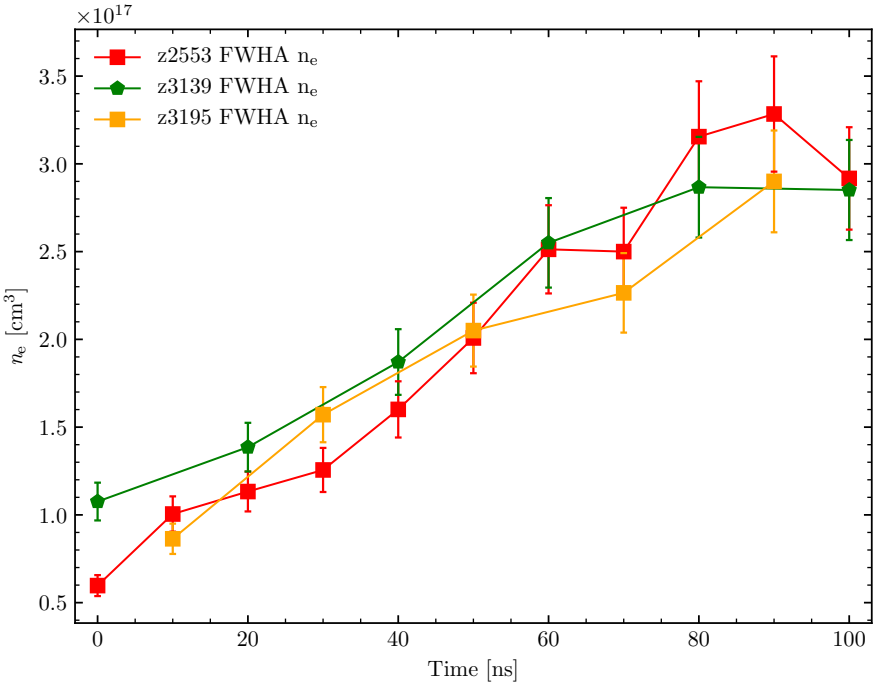

Figure 6.11: Comparison of n_e values derived from three different experiments using the FWHA method: z2553 (red, 10 T pure hydrogen), z3139 (green, 20 T H_2/He) and z3195 (orange, 20 T H_2/He). The derived n_e trends are very similar, indicating that the He is not a major electron donor at the WDPE plasma conditions.

Table 6.1: n_e comparison shot data

shot	**LOS dist. [mm]**	**gas fill**	**H_2 partial pressure [Torr]**
z2553	10	10.63 ± 0.05 H_2	10.63 ± 0.05
z3193	10	21.96 ± 0.42 H_2/He	14.64 ± 0.42
z3195	10	20.71 ± 0.21 H_2/He	13.80 ± 0.21

remain in the ground state. Helium ionization only occurs in close proximity of the backlighting surface and therefore contributes little, if anything, to the overall plasma n_{e}.

6.4.4 T_{e} determination in H_2/He mixture plasmas

In Sec. 6.4.3, I demonstrated that the vast majority of the electrons in my H_2/He mix plasmas are donated by hydrogen. I can therefore estimate the LTE plasma T_{e} using the Saha equation:

$$\frac{n_{i+1}n_e}{n_i} \approx \frac{n_e^2}{n_1} \approx \frac{2g_{i+1}}{g_i}\frac{(2\pi m_e k_B T_e)^{1.5}}{h^3}e^{-\chi/k_B T_e} \tag{6.4}$$

In the simplification of Eq. 6.4, I assume that hydrogen ionization is the source of all plasma electrons and that all non-ionized H atoms are in the ground state. Both of these assumptions are well justified (see Sec. 6.4.3 and Falcon et al. 2015b). I adopt the usual values for all constants in Eq. 6.4, with $\chi = 13.6$ eV, the ionization energy of hydrogen. T_{e} values resulting from this equation are shown in Fig. 6.12 as orange squares. This figure also shows the ionization fraction of experiment z3195 in purple. Since I don't perform detailed line fits in the FWHA n_{e} determination method, I do not have the capabilities of deriving a hydrogen n=2 population. However, data presented Falcon et al. (2015b) indicate that the WDPE plasma reaches LTE after ∼50 ns. I have no reason to suspect otherwise in the H_2/He mix experiments. The experimental LTE regime is highlighted grey in Fig. 6.12

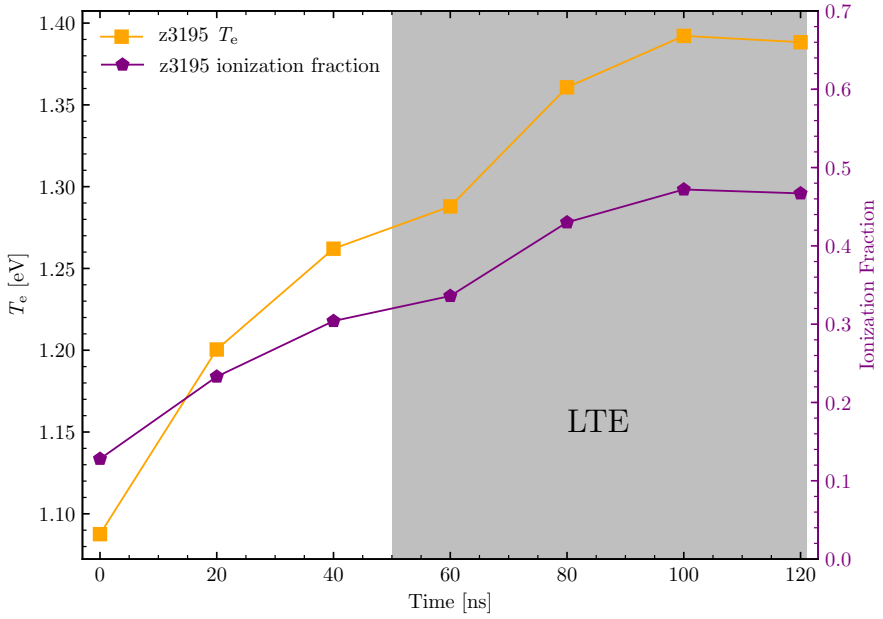

Figure 6.12: Derived T_e (orange) and ionization fraction (purple) for experiment z3195. For the first 50 ns, the temperatures are most likely slight overestimates due to the assumption of LTE. The region of assumed LTE is highlighted in grey.

6.4.5 The He I 5876 Å shift measurement

Now that I've described and quantified the wavelength calibration and plasma parameter extraction methods, I am in a position to perform the shift measurement. I use my emission and absorption data to measure the Stark shift.

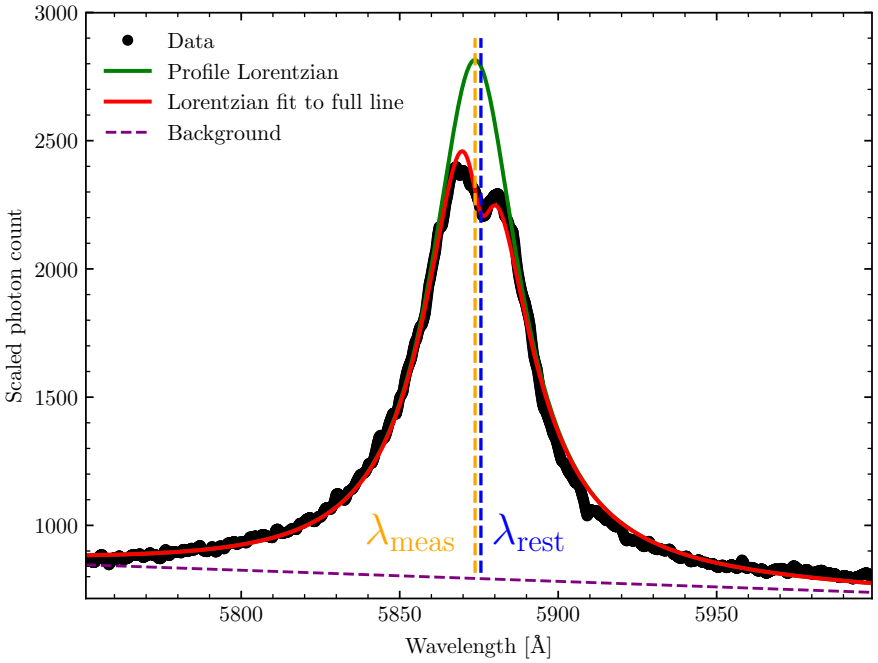

Figure 6.13: Emission shift measurement of the z3195 He I 5876 Å line integrated from 60-80 ns. Due to the self-absorption feature at the center, emission data is fit with two Lorentzians: one for the profile (green) and one for the dip in the center. I also show the linear background to the fit, as well as the rest and measured wavelength of this line. The difference is obvious.

6.4.5.1 The emission shift measurement

Many studies have shown that the He I 5876 Å transition has a Lorentzian shape (e.g., Heading et al. 1992; Büscher et al. 1995; Gigosos et al. 2014). I therefore use that particular line shape to extract the Stark shift. Fig. 6.13 depicts a shift measurement performed on the z3195 60-80 ns emission lineout. Due to the clear presence of a self-absorption feature in the center of the

emission line, I fit this profile with the following combination of Lorentzians:

$$L_{prof} \times e^{L_{dip}} \tag{6.5}$$

In Eq. 6.5, L_{prof} is the Lorentzian fit to the bulk of the profile (green in Fig. 6.13), while L_{dip} represents the fit to the self-absorption feature. Since the dip in the center of the emission profile is a *transmission* measurement of the self-absorption, an exponential of a Lorentzian has to be fit to that feature. The complete fit incorporating both L_{prof} and L_{dip} is plotted as a red line in Fig. 6.13 and contains six free parameters: two Lorentizan amplitudes, σ values, and centers. During the fitting process, the center of the self-absorption Lorentzian (L_{dip}) is set to the measured location of that feature, which was generally 5875.621 Å, the rest wavelength of this feature. The resulting Lorentizan fit to the profile (L_{prof}, green in Fig. 6.13) is then used to perform the shift measurement. The central location of the profile Lorentzian clearly differs from the rest wavelength of the He I 5876 Å transition (see λ_{meas} and λ_{rest} in Fig. 6.13).

6.4.5.2 The absorption shift measurement

The absorption shift measurement is also extracted using Lorentzian fits to experimental profiles. These fits, however, are performed in optical depth units (see Fig. 6.14). Unlike the emission profiles, the absorption data does *not* suffer from obvious self-emission effects. To ensure that a cold boundary layer plasma does not influence the shift measurements, I exclude the central portion of the absorption line profile (black - full data, green - fit data in

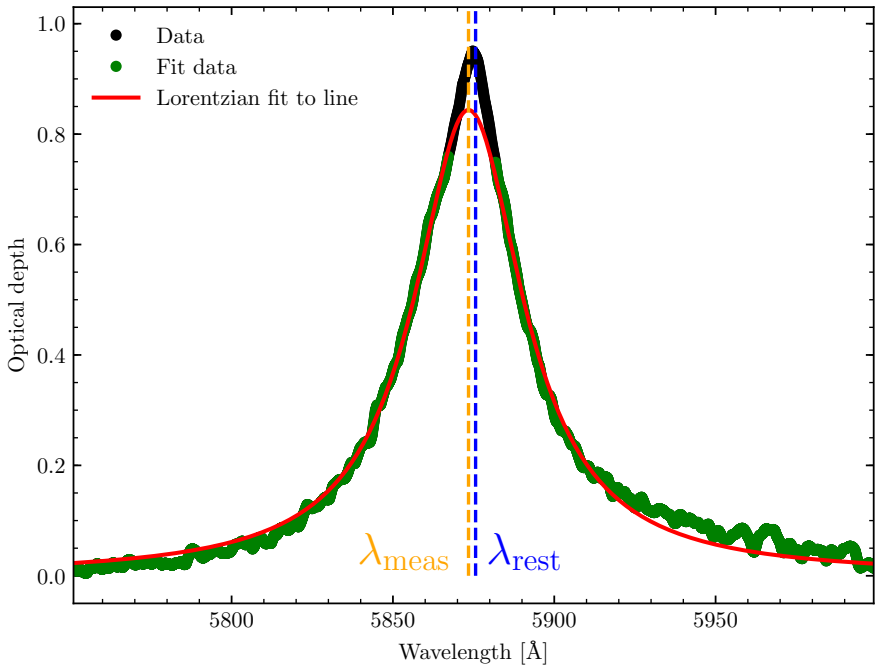

Figure 6.14: Sample absorption shift measurement of He I 5876 Å line from shot z3195. This is again an integration from 60-80 ns. Due to potential extra absorption coming from a boundary layer of cool plasma, I exclude the central peak of the absorption profile. See text for more details.

Fig. 6.14) during the fitting process. The final shift is then derived using the red Lorentzian in Fig. 6.14. This Lorentzian represents the fit to the green data points. My tests have shown that unless more than 50% of the line profile is excluded in the fitting process, the derived shift is fairly insensitive to the width of the excluded portion of the profile.

An approximate calibration for the width that should be excluded to account for boundary layer plasma effects can be obtained from the higher-resolution 600 g/mm data shown in Fig. 4.14. A 20 ns lineout from that CCD

image is presented in Fig. 6.15. Since the resolution of the data shown in Fig. 6.15 is twice that of the spectra plotted in Fig. 6.14, it gives a much clearer picture of the influence of potential cold boundary plasmas on the absorption line profile. Fig. 6.15 shows a fit of the product of two Lorentzian exponentials (red) to the data (black dots). This Lorentzian can be deconvolved into the profile only (green in Fig. 6.15) and central dip (orange in Fig. 6.15) components. The width of the central dip fit is then used to calibrate how much data is to be excluded in the absorption shift determination shown in Fig. 6.14. Upon exclusion of the central absorption component in that figure, a clear difference between the measured and rest wavelength can be observed. Further evidence for the assumption that the extra central absorption seen in Figs. 6.14 and 6.15 originates from a cold boundary layer plasma is provided by the fact that those features are located at 5875.62 Å, the rest wavelength of the line being studied. This indicates that a low T_e and n_e plasma is responsible for this behavior.

6.4.5.3 Comparison of absorption and emission shift measurements

Optical depth and plasma inhomogeneity arguments have been invoked to explain differences in experimental He I 5876 Å shift measurements (e.g., Büscher et al. 1995). Since I collect both absorption and emission spectra of the same plasma at the same time, I am in an ideal position to test these assertions. As demonstrated in Fig. 6.15, boundary layer plasmas influence my absorption spectra, while optical depth (or self-absorption) effects are present

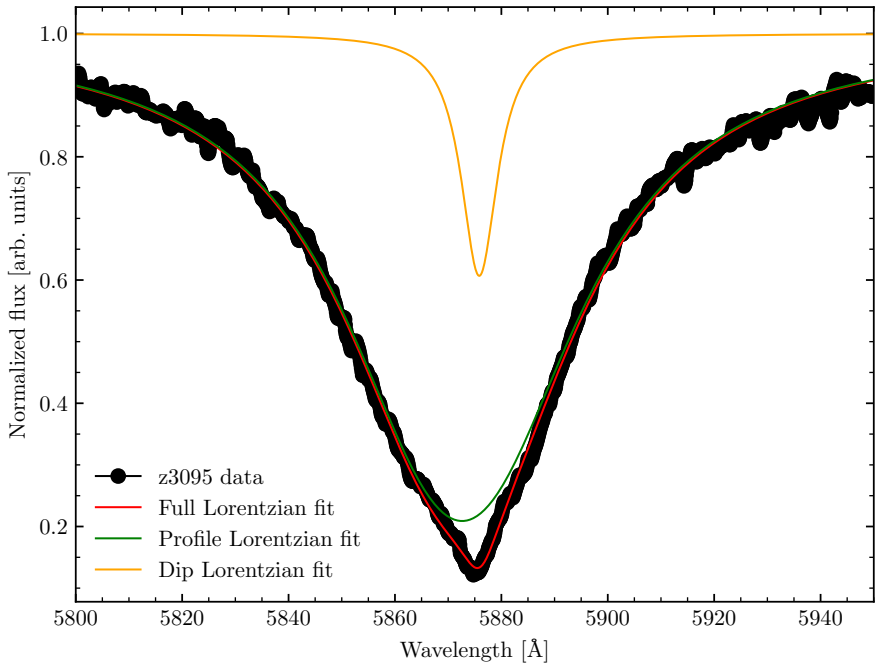

Figure 6.15: Sample absorption shift measurement of He I 5876 Å line. Due to potential extra absorption coming from a boundary layer of cool plasma, I exclude the central peak of the absorption profile.

in my emission data (see Fig. 6.13). Deriving differing shifts from absorption and emission profiles would indicate that the both of these issues can significantly impact He I 5876 Å Stark shift measurements. Fig. 6.16 shows the shifts of the z3195 absorption (red) and emission (blue) profiles. The emission shift cannot be measured until ∼60 ns after onset of heating from the gold wall since the corresponding line is not strong enough until that point in the experiment. As evident from Fig. 6.16, absorption and emission shifts are consistent.

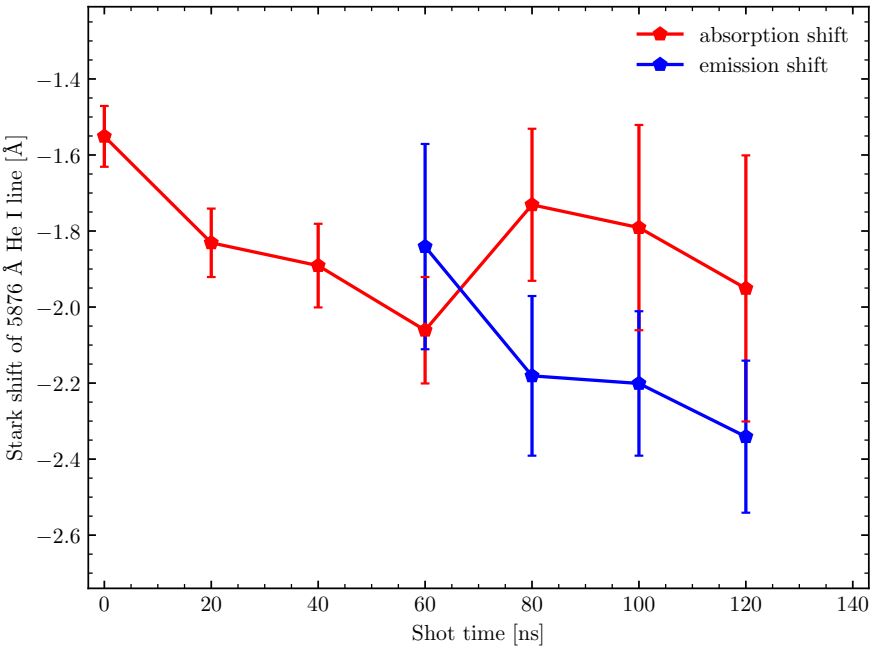

Figure 6.16: Comparison of absorption (red) and emission (blue) shifts. Within the errors, these shifts agree, indicating that boundary layer plasma and optical depth effects are not as important as previously thought. Furthermore, the agreement of absorption and emission indicate both LOS sample the same n_e values.

6.4.5.4 The influence of distortion correction on the He I 5876 Å shift measurement

Sec. 6.4.2 describes the influence of data distortion on the CCD wavelength calibration. The associated effects on the He I 5876 Å shift measurements are discussed here. I show a comparison of raw (orange) and distortion corrected (blue) shift measurements in Fig. 6.17. As already alluded to in Sec. 6.4.2, the distortion correction only produces a transverse shift of the laser lines on the CCD. Only small time trends are introduced during this

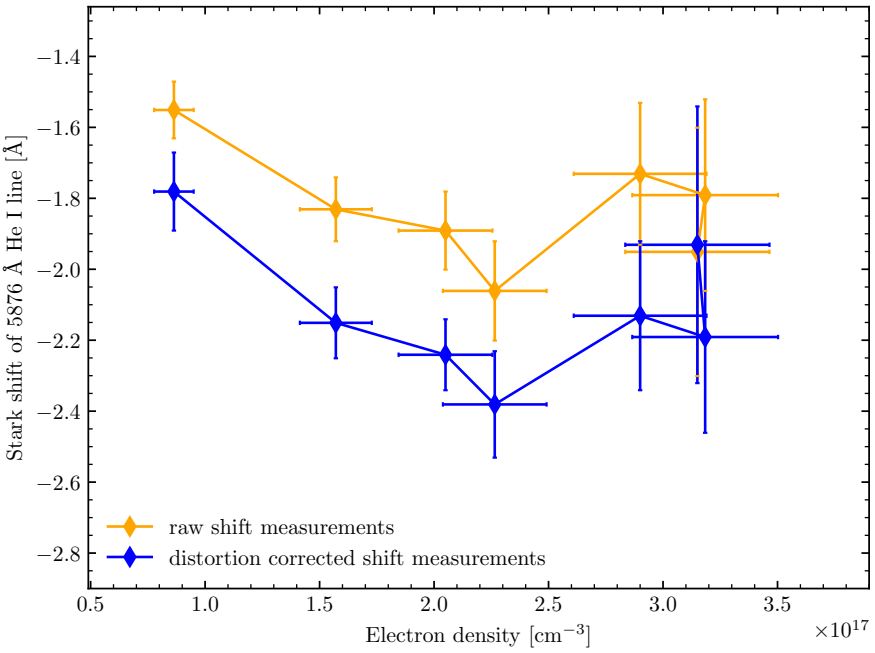

Figure 6.17: Comparison of raw (i.e. uncorrected) and distortion corrected He I 5876 Å shift measurements. The distortion correction only changes the magnitude of the derived shift. The trend is unaffected. On average, the raw and distortion corrected shift differ by ∼0.28 Å.

procedure. It is therefore not surprising that the raw and distortion corrected measurements differ only in magnitude. On average, the two shift values disagree, by ∼0.28 Å, almost matching the mean error of my wavelength shift measurements. The discrepancies in the two approaches are therefore inconsequential. For the remainder of this chapter, I adopt the distortion corrected (blue) He I 5876 Å shift values.

6.5 Comparison of my He I 5876 Å shift measurements with previous experiments and theory

Questions regarding wavelength calibration, n_e and T_e determination, as well as data distortion have been discussed in the preceding sections. I am now in a position to compare my shift measurements with those of previous experiments and theories. As mentioned above, my data collection, extraction, and analysis approach all differ heavily from other investigations. A direct comparison will therefore allow me to explore many of the potential problems that have been attributed to previous experiments. I show such a comparison in Fig 6.18. Since the current WDPE design does not allow for He shift measurements at $n_e \gtrsim 3.5\times10^{17}$, the axes in this figure do not match those of Fig. 6.2 and 6.3. In Table 6.2, I list all relevant n_e, T_e, and shift data. The errors for n_e and T_e listed in that table are estimated to be 10%.

Table 6.2: n_e, T_e, and shift data for shot z3195

$\boldsymbol{n}_e$ [$\mathbf{cm}^{-3}$]	$\boldsymbol{T}_e$ [eV]	shift [Å]
8.64×10^{16}	1.09	-1.78 ± 0.11
1.57×10^{17}	1.20	-2.15 ± 0.10
2.05×10^{17}	1.26	-2.24 ± 0.10
2.27×10^{17}	1.29 (LTE)	-2.38 ± 0.15
2.90×10^{17}	1.36 (LTE)	-2.13 ± 0.21
3.18×10^{17}	1.39 (LTE)	-2.19 ± 0.27
3.15×10^{17}	1.39 (LTE)	-1.93 ± 0.39

From Fig. 6.18, it is obvious that my data is consistent the shift values of Gauthier et al. (1981). This is expected since they are at almost the exact

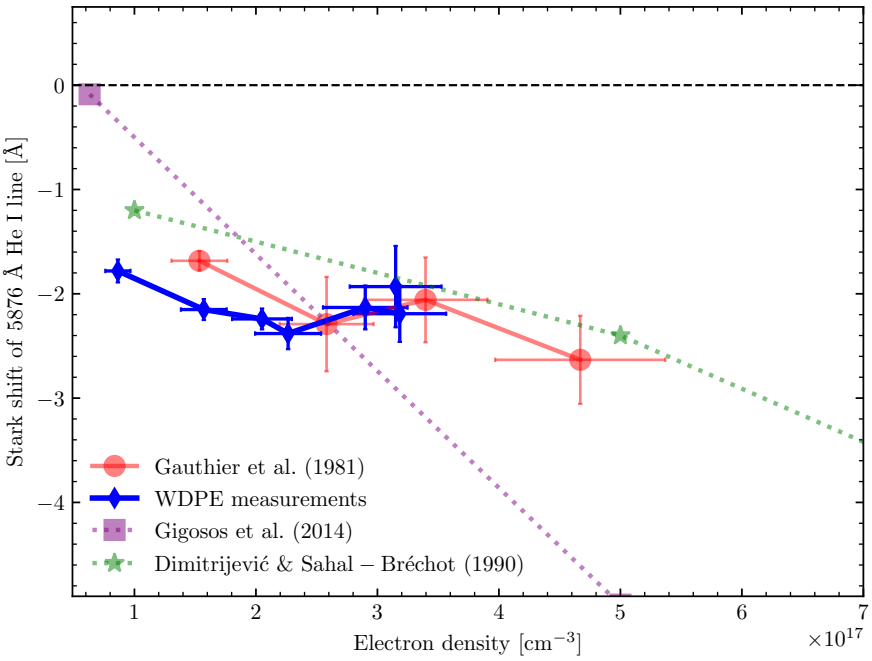

Figure 6.18: Comparison of my shift measurement to those of the Gauthier et al. (1981) (red) and the theories of Dimitrijevic & Sahal-Brechot (1990) (green) and Gigosos et al. (2014) (purple). My measurements agree very well with those of Gauthier et al. (1981) and do *not* reproduce the theories of either Dimitrijevic & Sahal-Brechot (1990) (green). Due to current limitations of the WDPE platform, I am unable to perform measurements at $n_e \gtrsim 3.5\times10^{17}$. The n_e and shift axes in this plot do therefore not match that of Figs. 6.2 and 6.3.

same n_e and T_e as my experiments. It is also clear that my measurements do *not* reproduce the Dimitrijevic & Sahal-Brechot (1990) or Gigosos et al. (2014) theories. In fact, my experiments indicate that valid data for the sign and magnitude of the He I 5876 Å Stark shift have existed since 1981. It is unclear why theoretical models have been unable to reproduce those experimental measurements. Büscher et al. (1995) discuss multiple possible reasons for these

weaknesses and appealed to the theoretical community to further develop their calculations. Gigosos et al. (2014) published their He I 5876 Å Stark shift predictions after the Büscher et al. (1995) paper, yet it appears that their models result in an even more severe blueshift than any previous theory. Their calculations do not match *any* experiment that has been published to date. From an astrophysical point of view, the results in Fig. 6.18 clearly show that no reliable theory for the He shift at the temperatures and densities of DB atmospheres exists. Hence, the WD community currently cannot perform any DB GR mass measurements. I repeat here the call of Büscher et al. (1995) - theoretical work is urgently needed to address the obvious disagreements between He I 5876 Å Stark shift theory and experiment.

6.6 Neutral broadening in the He I 5876 Å line

In addition to weaknesses in their GR mass determination method, DB WDs also suffer from shortcomings in their spectroscopic mass derivation technique. Data presented in Fig. 2.4 shows a large increase in the spectroscopically determined log g (or mass) at low ($\lesssim$ 16,000 K) $T_{\rm eff}$. This behavior has been attributed to incorrect treatment of neutral broadening in DB atmospheric models (Bergeron et al. 2011; Koester & Kepler 2015). The WD community currently uses the Deridder & van Renspergen (1976) neutral broadening model to account for this effect. These broadening predictions have unfortunately *never* been validated experimentally. Deridder & van Renspergen (1976) attempted to corroborate their calculations by comparing their neutral

shift predictions to those measured in laboratory experiments. They then reason that since their *shift* calculations agree with measurements, their neutral *width* predictions must also be correct.

The data collected for the He I 5876 Å shift experiments can also be used to test neutral broadening predictions. The physical mechanism enabling these measurements is explained in Sec. 6.4.3. As demonstrated in that section, the helium in my experiments will not get significantly ionized, while hydrogen will achieve at most, 50% ionization. The measured He I 5876 Å line will therefore be broadened by electrons, and neutral helium as well as hydrogen atoms. I can separate the neutral and electron broadening effects and hence test the Deridder & van Renspergen (1976) neutral broadening theory.

Fig. 6.19 shows the results of such a separation for a single time-step in shot z3195. The plotted red profile is the measured experimental absorption profile, which is broadened by electrons and neutrals. Using the n_e inferred from Hβ, the He I 5876 Å width can be confidently calculated using the any of the Stark broadening theories referenced in Gigosos et al. (2014), all of which have been validated by multiple experiments. The Stark profile is shown as a dotted blue Lorentzian in Fig. 6.19. Deconvolving the measured line (red in Fig. 6.19) from the predicted Stark (dashed blue in Fig. 6.19) and instrumental profile (Lorentzian with a FWHM of $\sim$3 Å, not shown in Fig. 6.19) results in the *measured* neutral broadening contribution to the total line width (green dotted line in Fig. 6.19). The estimated n_e for show shown dataset is $2.37\times10^{17}\text{cm}^{-3}$, while the neutral density is estimated to be $4.10\times10^{17}\text{cm}^{-3}$.

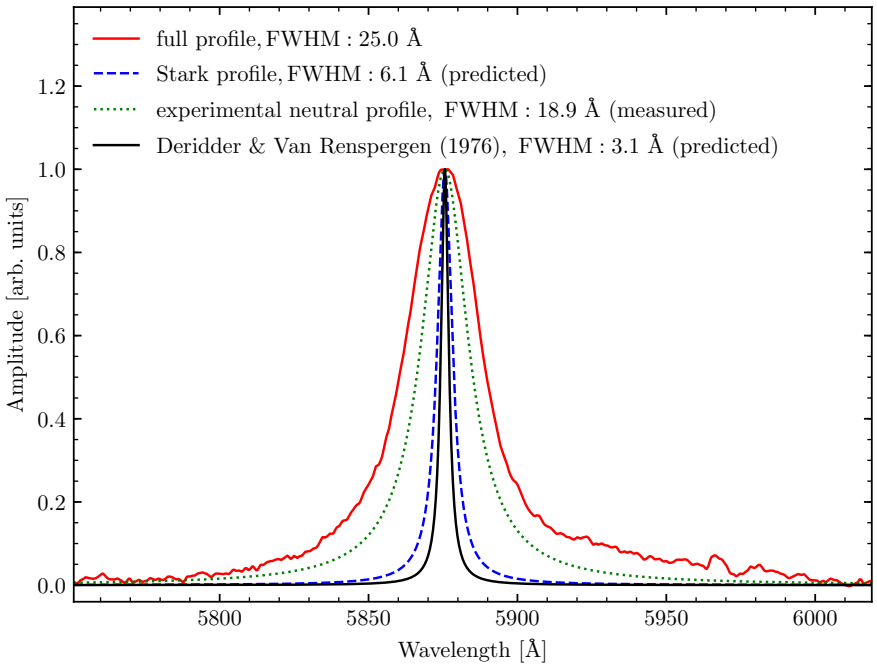

Figure 6.19: A graphical demonstration of my neutral broadening testing method. The experimental profile is shown in red, while the pure Stark (electron only) profile is shown in blue. The experimentally determined neutral broadened profile is depicted in green. The Deridder & van Renspergen (1976) prediction neutral width prediction for my plasma conditions is shown as a black line.

I can then compare my experimentally determined neutral width to that predicted by Deridder & van Renspergen (1976), which is shown as a black Lorentzian in Fig. 6.19. The predicted and measured neutral FWHM contributions differ by about a factor of six. My data thus demonstrates that the Deridder & van Renspergen (1976) calculations *underpredict* neutral broadening in plasmas. These findings also may imply that the mass trends observed in Fig. 2.4 stem from neutral broadening treatment weaknesses in helium WD

atmosphere models. The electron contribution in the lower-temperature spectroscopic DB fits is thus *overpredicted*, leading to artificially increased masses. I note here for completeness that the He I 5876 Å transition is not subject to resonance broadening since neither the lower ($1s2p\ ^3\mathrm{P^O}$) nor upper level ($1s3d\ ^3\mathrm{D}$) have an allowed electronic dipole transition to the ground level ($1s^2\ ^1\mathrm{S}$). This is still a work in progress, so I will defer any further discussion to a future publication.

Chapter 7

The Carbon Experiments

7.1 Scientific motivation for the carbon experiments

Experiments involving carbon are aimed at solving mass determination problems in hot DQ (i.e., carbon dominated) WDs. Dufour et al. (2007) first reported the discovery of these objects. The authors of that paper were unable to produce definitive atmospheric parameters for these hot DQs due to uncertain carbon atomic data. Consequently, the evolutionary origin of hot DQs remained a mystery (Dufour et al. 2008). A first real breakthrough in the study of hot DQs was achieved by Dufour et al. (2011). Instead of relying on outdated atomic data to infer the masses of those objects, Dufour et al. (2011) perform new carbon Stark broadening calculations at DQ WD atmospheric conditions (5,000 K $< T_{\rm e} <$ 100,000 K, $n_{\rm e} \sim 10^{17}$ cm^{-3}) using the semi-classical perturbation technique. These updated Stark parameters raised the mean DQ log g from $\sim$8 (Dufour et al. 2007) to $\sim$9 in cgs units. According to current theory, such an increase in surface gravity implies that hot DQs have oxygen-neon-magnesium cores, which result from carbon fusion during the asymptotic giant branch of stellar evolution (see Ch. 1). Hot DQs could therefore represent an entirely new class of WDs probing massive stars in the early Galaxy. The hot DQ spectroscopic mass determination approach is

complicated by the presence of unknown magnetic fields in tj,gvhose objects (Dufour et al. 2011). Dufour et al. (2013) present evidence that all DQs may contain some form of magnetic field. It is currently unclear whether the presence of such fields would change the inferred masses of these stars.

Possible evolutionary scenarios of hot DQs are just as uncertain as their masses. Althaus et al. (2009) and Córsico et al. (2009) suggest that these stars result from a particularly violent late thermal pulse (see Sec. 6.1), which expels both H and He from the stellar surface. There is potential corroborating evidence for such a scenario in the hydrogen and helium devoid PG 1159 star H1504+65 (Dufour et al. 2008). Once all the H and He has been ejected from the stellar atmosphere, the star begins to cool and gravitational settling sets in, turning the star into a hot DQ. Althaus et al. (2009) and Córsico et al. (2009) predict a mean mass of 0.87 $M_{\odot}$ for the hot DQ population based on this scenario.

Schwab et al. (2016) propose another potential evolutionary channel in which hot DQs could develop from the merger of two standard C/O core WDs. If the combined mass of the two WDs participating in the merger is super-Chandrasekhar (i.e. $M_{\star} \gtrsim 1.44\ M_{\odot}$), a Type Ia supernova may result. However, if the envelope of the merger product expands, cools, and loses sufficient mass to produce a sub-Chandrasekhar mass object, it may evolve into a hot DQ. As pointed out by Schwab et al. (2016), this evolutionary scenario is complicated by poorly constrained mass-loss mechanisms in stellar atmospheres.

Differentiating between the above evolutionary scenarios requires accurate DQ atmospheric parameters. Current DQ $T_{\rm e}$ and $n_{\rm e}$ measurements are performed using the Dufour et al. (2011) Stark width predictions. These calculations have not been experimentally validated. It is therefore unknown if the high log g values presented in Dufour et al. (2011) are correct. The scientific impact of these results, however, are significant. As demonstrated by Schwab et al. (2016), hot DQs could be failed Type Ia supernovae - an astrophysical phenomenon that has been unexplained for many decades (e.g., Nomoto et al. 1997, and references therein). I therefore attempted to develop an experimental platform at the Z-machine that would allow me to confirm the calculations of Dufour et al. (2011). In this chapter, I present this updated platform and analyze the resulting data.

7.2 The development of the carbon gas cell

7.2.1 Initial experiments

The standard version of the WDPE gas cell is presented in Ch. 3. This design can reach a maximum $T_{\rm e}$ of $\sim$15,000 K with hydrogen and helium gas fills at 10 mm from the gold wall (see Chs. 5 and 6). Hot DQs are only found at temperatures between 18,000 K and 24,000 K, slightly higher than the maximum $T_{\rm e}$ of the standard WDPE design. However, the photoionization cross section of carbon differs significantly from that of hydrogen and helium. Simulation data shown in Fig. 7.1, which was calculated using VisRad (see Sec. 3.2), suggests that the Mylar filtered Z-flux entering the gas cell will

directly interact with carbon. The black dashed line in Fig. 7.1, derived again using the Henke filter website (which gives the transmission for *cold* Mylar, see Sec. 3.2), gives the photon energy distribution for the Mylar filtered X-ray flux, while the purple data represents the absorption of a carbon plasma at a T_e of 1.5 eV and an assumed n_e of $3\times10^{17}\text{cm}^{-3}$. The overlap of these two curves indicates that a carbon gas fill could potentially reach much higher temperatures than an experiment performed with hydrogen or helium due to the predicted direct interaction between the high energy Z-flux and the C atoms. This direct heating of the carbon, which is *not* predicted for either hydrogen or helium plasmas (compare Fig. 3.8), could therefore result in the temperature increase needed to probe hot DQ atmospheric conditions.

The results of a shot containing 10 Torr of ethane (C_2H_6) using the standard WDPE setup is shown in Fig. 7.2. These experiments were performed in November of 2014 by Ross Falcon, before my official involvement in the Sandia project. I'm merely using these data for demonstration purposes. The main feature of hot DQ spectra is the presence of *atomic* carbon lines (see, for example, Fig. 1 in Dufour et al. 2011). In Fig. 7.2, only molecular carbon (C_2) or CH features can be observed (aside from Hβ and Hγ lines). These data are interesting in their own right, but do not address the scientific goals of the carbon experiments. The direct interaction of the Z-pinch with the C atoms clearly did not raise the temperature to the required level needed to produce atomic carbon lines. A different experimental approach is required.

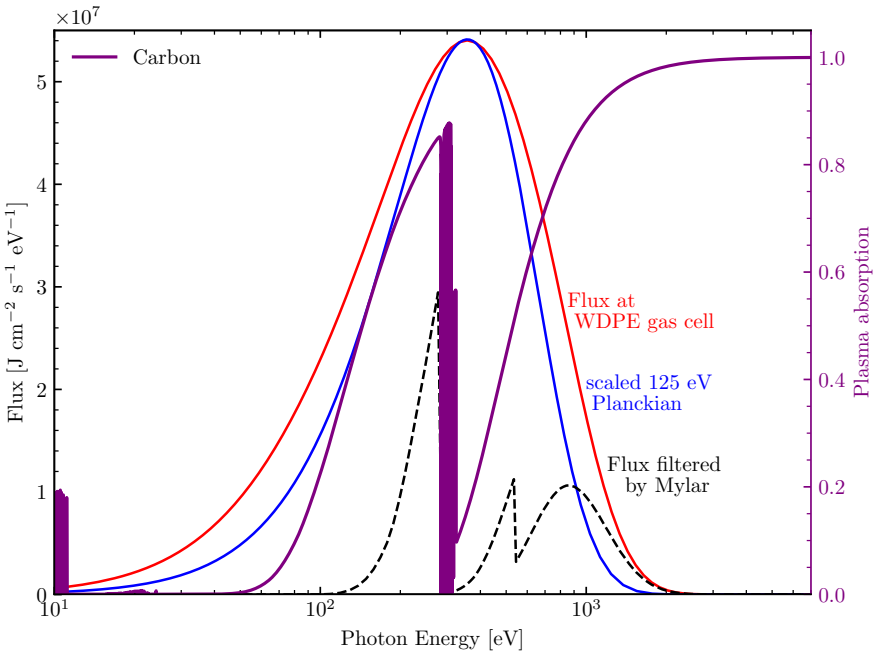

Figure 7.1: Time-averaged flux arriving at the Mylar window as a function of photon energy. I plot a 125 eV Planckian for comparison purposes. The Mylar transmitted flux is shown as a black dotted line. I also show the mean absorption of a pure carbon plasma (purple).

7.2.2 Increasing the temperature in the WDPE

The data presented in Fig. 7.2 highlight the need for an increased experimental T_e. Raising the temperature in the gas cell can be achieved in two ways: (i) decrease the Mylar thickness (to reduce x-ray filtering) or (ii) move WDPE hardware closer to the Z-pinch. However, reducing the Mylar thickness was found to be difficult because this thinner filter was unable to contain the gas fill.

The main challenge in moving closer to the Z-pinch is the lack of avail-

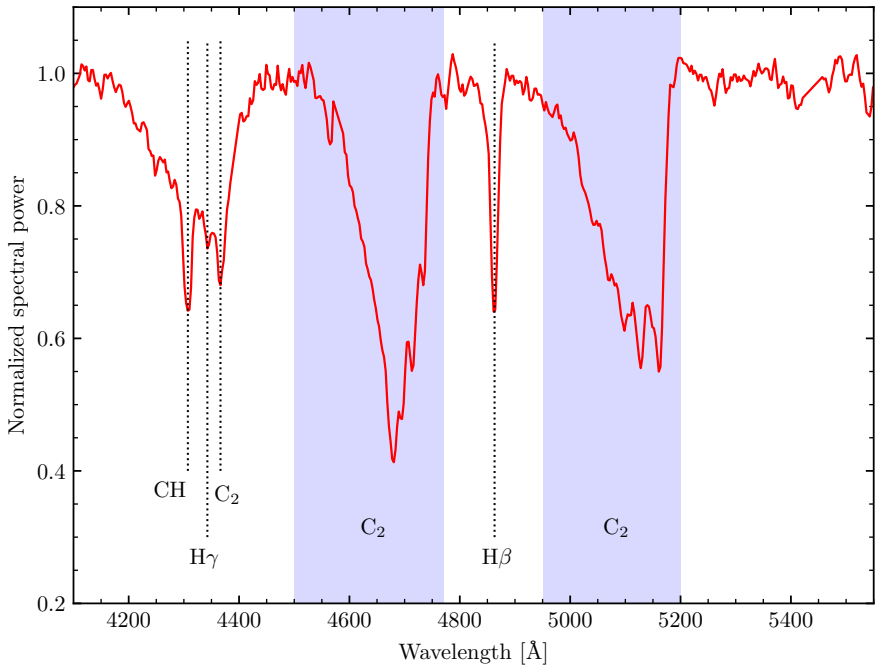

Figure 7.2: Spectra resulting from carbon experiments obtained by using the standard WDPE gas cell. The experiment clearly did not reach the temperature required to produce atomic carbon lines.

able space around the X-ray source (Rochau et al. 2014). Experiments performed concurrently with WDPE probe much higher T_e-n_e combinations and therefore occur within millimeters of the Z-pinch. Fig. 7.3 shows the final carbon experiment gas cell design as mounted in the Z-machine. This figure also highlights the challenges of moving the experiment closer to the X-ray source. I note the locations of two apertures in Fig. 7.3, both of which are crucial to two integral experiments performed alongside the WDPE. The final carbon gas cell design maximizes the length of the gas cell while preserving the size of

the buffers. The distance between the Z-pinch, (center of the current return can, highlighted orange in Fig. 7.3), has been reduced to 149 mm. According to simulations, the flux into the cell should increase by a factor of 5.3 with respect to the cell design described in Ch. 3. I do not show a detailed view of the WBS cell design, since it is very similar to that shown in Fig. 3.6 and 3.9, except that the gas cell length is now 80 mm.

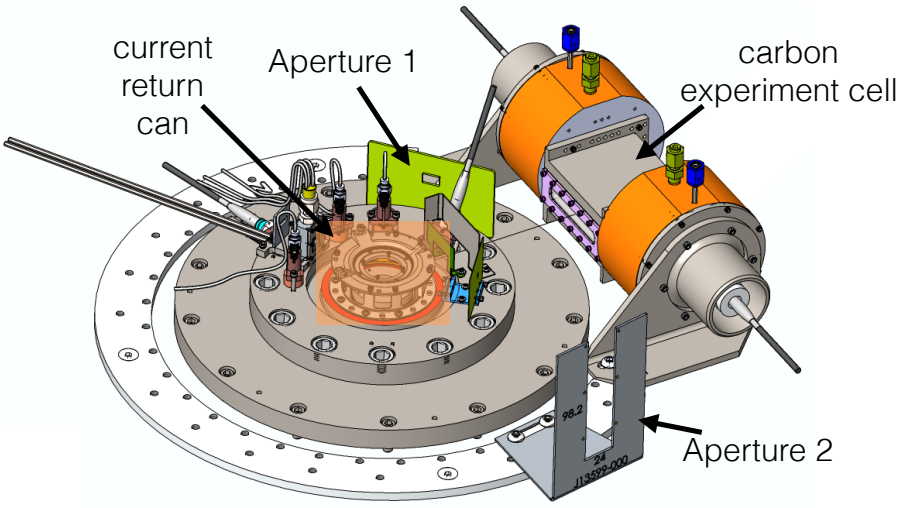

Figure 7.3: Design of the carbon experiment cell. This design minimized the distance of the cell from the Z-pinch and maximizes the length of the gas cell. This new design is now located about 149 mm away from the Z-pinch. The length of the gas cell has been reduced to ∼8 cm.

7.2.3 Results of the carbon gas cell experiments

Results of experiment z2972 (5 T CH_4 observed at the 5 mm LOS) collected with the carbon gas cell (Fig. 7.3) are shown as black squares in Fig. 7.4. I also plot PrismSPECT (MacFarlane et al. 2003) fits to the atomic carbon data

(C II and C III, red synthetic spectrum) and Hβ (blue synthetic spectrum). The C II and C III lines indicate a T_e of $\sim$4.2 eV and an n_e of $\sim 9\times10^{17}$ cm^{-3}. Fitting Hβ results in a T_e of $\sim$1.2 eV and an n_e of $\sim 1\times10^{17}$ cm^{-3}. The difference in the derived parameters points could be interpreted as evidence for the existence of at least two plasmas within the carbon gas cell. Under this assumption, the dominant and hotter component produces the C II and C III lines. Since its temperature is $\sim$4.2 eV, Hβ cannot emanate from this plasma. Hydrogen is fully ionized at such temperatures. The C II and C III features cannot originate from the Hβ plasma since the temperature inferred by that line is not high enough to produce atomic carbon lines. This interpretation of the data presented in Fig. 7.4 assumes that the PrismSPECT calculations used to provide the fits for that figure are correct.

If Hβ emanates from a colder boundary layer plasma, its origin must be understood so that it can be removed from the data. Since the plasma temperature is now much higher than in the standard cell design, is the buffer gas heated to higher T_e values and thereby creating this Hβ line? Or is this two component plasma a result of a gradient along the gold back wall (see Ch. 5)? I attempted to answer the first question by designing a no- and half-buffer carbon cell (see Fig. 7.5) Only the no-buffer design has been used in experiments, none of which resulted in usable data. The influence of these no- and half-buffer designs on emergent spectra will be further investigated after the completion of this PhD.

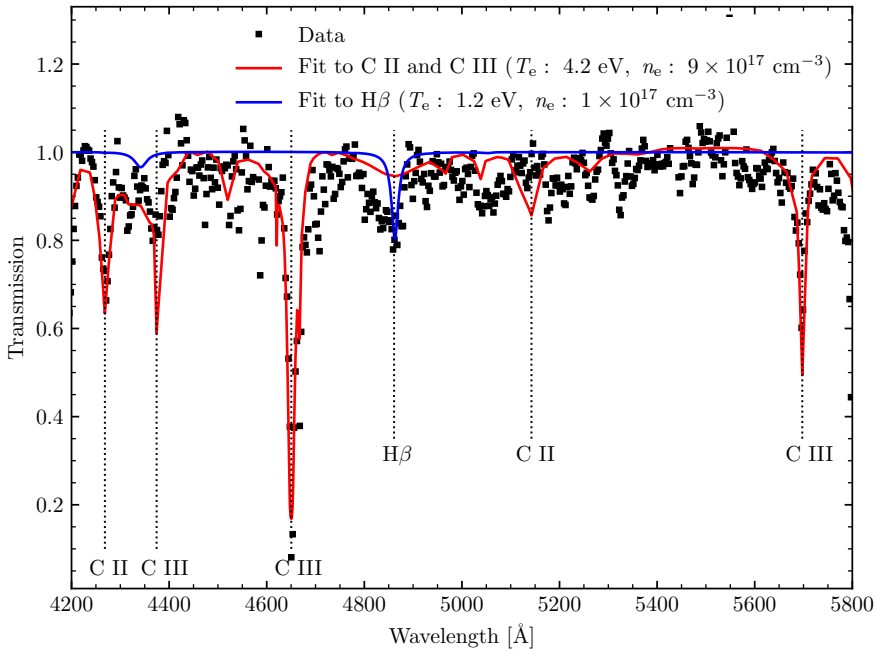

Figure 7.4: Representative spectra of methane experiment z2972 performed using the carbon cell design shown in Fig.7.3. The red spectrum shows a fit to the C II and C III data (black squares), while the blue spectrum gives a fit to the Hβ. The temperatures and densities for these fits are given on the plot. They're very different, indicating that the plasma in this new cell design consists of at least two components.

7.2.4 The influence of Mylar thickness on plasma temperature in the carbon gas cell

In addition to the two-component plasma, the carbon cell design shown in Fig. 7.3 also led to an experimental T_e of ∼4.2 eV instead of the desired 2 eV. An *increase* in the Mylar thickness should filter more of the incoming X-rays and thereby decrease the plasma temperature. Tests have shown that the carbon gas cell does not leak when thicker Mylar is used. A combination

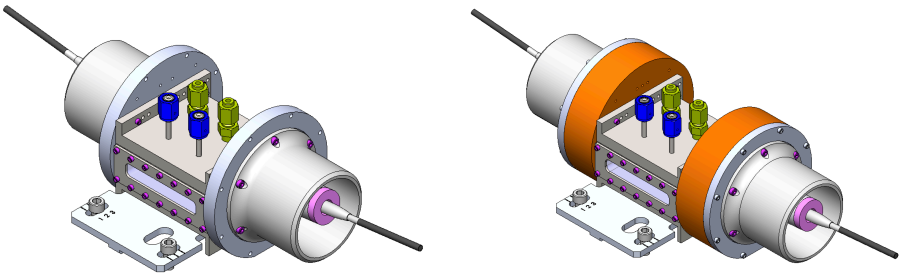

No buffer cell design Half buffer cell design

Figure 7.5: Designs of no-buffer (left) and half-buffer (right) carbon cells. These design alterations attempt to address the boundary layer plasma problem observed in Fig. 7.4. To date, no successful experiments using these cells have been performed.

of Helios (MacFarlane et al. 2006) and VisRad (MacFarlane 2003) simulations are employed to determine the Mylar thickness needed to decrease the plasma temperature from ∼4 eV to ∼2 eV.

Fig. 7.6 shows the simulation steps needed to derive the target Mylar thickness. The first step of the simulation (labeled 1), which results in the flux arriving at the carbon gas cell, was performed by Guillaume Loisel. These flux values remain constant throughout all Mylar thickness simulations. Step 2 models the interaction of the Z-pinch flux with the Mylar window. I simulated six Mylar thicknesses: 1.5 μm (the standard thickness), 2.0 μm, 3.0 μm, 3.5 μm, 4.0 μm, and 6.0 μm. This step also includes the initial interaction of the Mylar-filtered Z-pinch X-rays with the gas fill, which I assumed to be 10 T CH_4. Simulation step 3 calculates the interaction of the Mylar-filtered X-rays with the gold back wall, while step 4 then produces an estimate of the

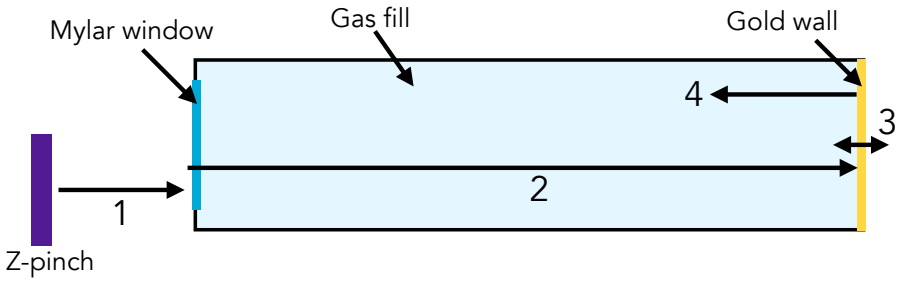

Figure 7.6: Succession of Helios simulations performed to determine the effects of Mylar thickness on final plasma temperature. The simulation labeled 1 was performed by Guillaume Loisel. These values remained constant throughout all simulations. Simulation 2 , which included the Mylar window, was updated for each calculation. This simulation step also included the initial interaction of Mylar-filtered Z-pinch with the CH_4 gas fill. Step 3 models the incident and re-radiated Mylar-filtered Z-pinch radiation on the gold wall, while simulation 4 then gives the final plasma T_e and n_e.

final plasma T_e and n_e. Figs. 7.7 and 7.8 show those final plasma T_e and n_e parameters for the 2.0 μm (red), 3.0 μm (blue), 3.5 μm (green), and 4.0 μm (orange) Mylar simulations. All other values are omitted from those figures as they did not produce temperatures and densities applicable to the scientific goals of the carbon experiments.

The target T_e of the carbon experiments is $\sim$2 eV, while the target n_e is a few 10^{17} cm^{-3}. Careful inspection of Figs. 7.7 and 7.8 reveals that two possible combinations of LOS distance and Mylar thickness fulfill this requirement: 3.0 μm Mylar at 5 mm (blue lines in those figures) or 2.0 μm Mylar at 10 mm (red lines in those figures). As pointed out in Ch. 6, performing measurements at the 5 mm LOS is undesirable for many reasons, leaving only the 2.0 μm Mylar option. The predicted plasma parameters for that Mylar

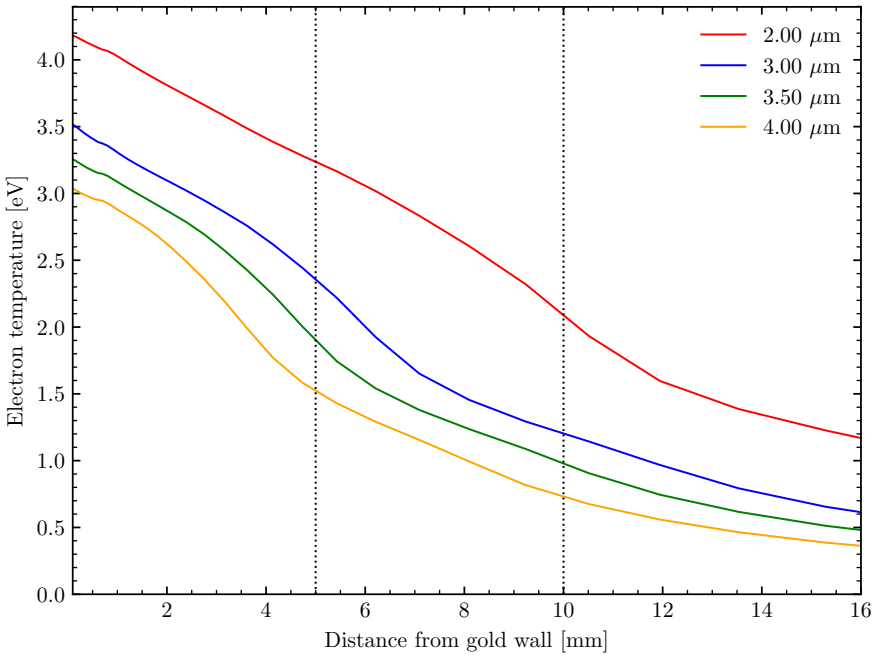

Figure 7.7: Resulting plasma T_e as a function of distance from gold wall for various Mylar thicknesses. The red curve gives the results for the 2.0 μm, blue represent the 3.0 μm T_e values, 3.5 μm results are given in green, and the 4.0 μm T_e predictions are plotted in orange. I also indicate the locations of the 5 mm and 10 mm LOS as vertical black dotted lines.

thickness are a T_e of $\sim$2.0 eV and and n_e of $\sim 8\times10^{17}$ cm^{-3}.

The predicted spectrum of a 10 Torr CH_4 gas fill with at the above plasma parameters is depicted in Fig. 7.9. One C I line (blue dashed), eight C II lines (green dashed), and three C III (orange dashed) lines are predicted , making the assumed plasma parameters ideal for an investigation into carbon Stark widths at the photospheric conditions of DQ WDs. Perhaps even more importantly, the Hβ n_e diagnostic is also still present, although it may not be

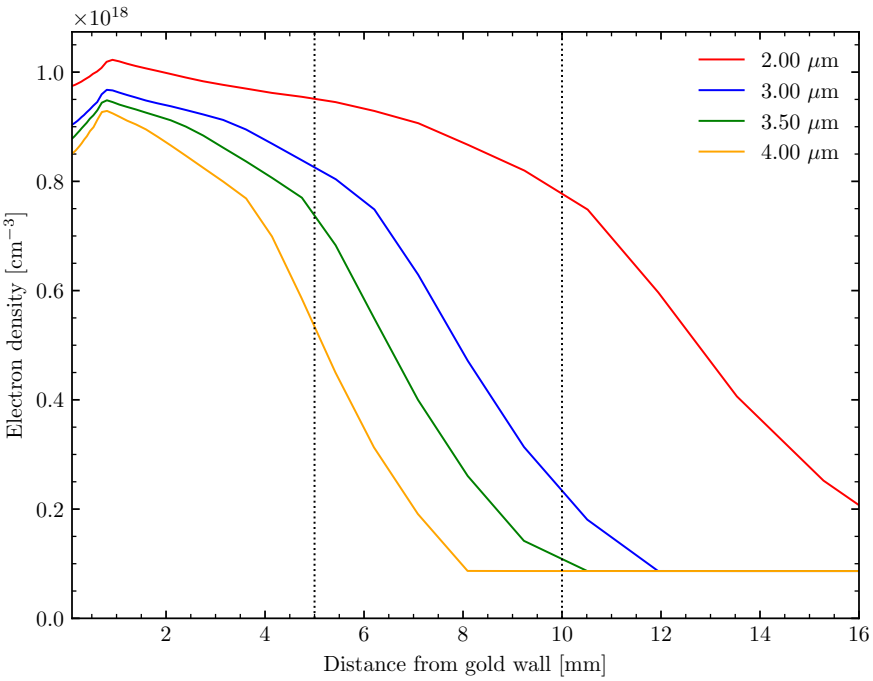

Figure 7.8: Resulting plasma n_e as a function of distance from gold wall for various Mylar thicknesses. The red curve gives the results for the 2.0 μm, blue represent the 3.0 μm n_e values, 3.5 μm results are given in green, and the 4.0 μm n_e predictions are plotted in orange. I also indicate the locations of the 5 mm and 10 mm LOS as vertical black dotted lines.

as reliable at these higher densities (see Falcon et al. 2017 for more details). As a final point in this chapter, I note that Helios over-predicts n_e by factors of three as compared to real WDPE data. It is thus possible that once this 2.0 μm Mylar experiment at a 10 mm LOS is performed, the resulting n_e values are in the exact range needed to validate the Dufour et al. (2011) Stark width calculations.

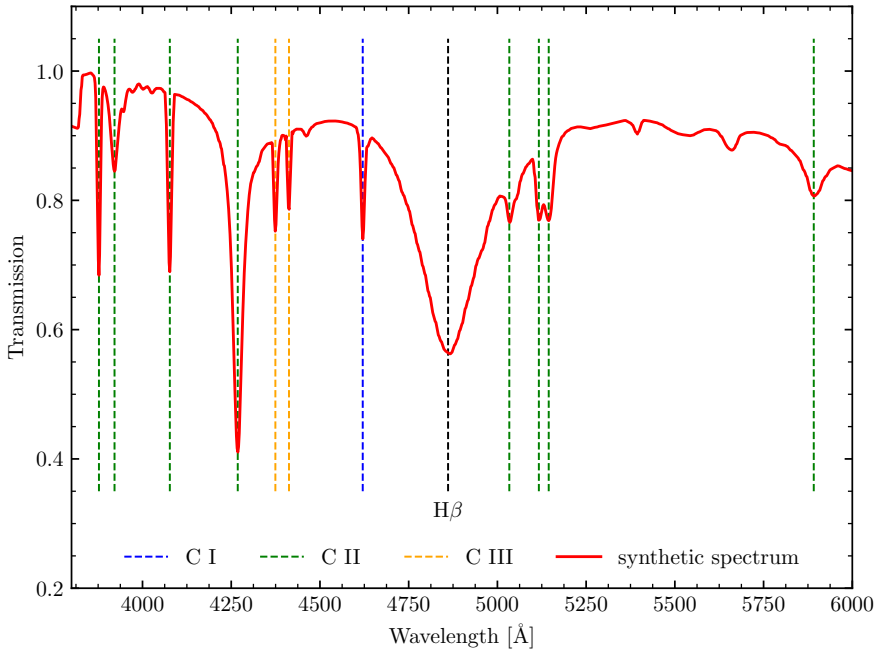

Figure 7.9: A representative spectrum obtained from a simulation assuming a 10 Torr CH_4 fill pressure and the plasma conditions obtained from the simulation of the 2.0 μm Mylar case at a distance of 10 mm from the gold wall. A multitude of atomic carbon lines can be seen in the resulting spectrum.

Chapter 8

Conclusions and Future Directions

In the preceding chapters, I've presented, almost the entire body of the work I have performed during the course of my nearly four years at Sandia National Laboratories in Albuquerque, NM. In this chapter, I will review results from my hydrogen, helium, and carbon experiments. I also discuss potential future directions for the WDPE.

8.1 Hydrogen

The defining advantage of the WDPE is its ability to collect absorption and emission data of the same plasma at the same time. This allows for the extraction of data that can be used to explore several effects:

1. Why do fits to hydrogen absorption lines in DA spectra, which are also in transmission, result in decreasing atmospheric $T_{\rm e}$ and $n_{\rm e}$ as higher order Balmer lines are included in the analysis (see Fig. 2 of Tremblay & Bergeron 2009)?

2. Is the assumption of complete redistribution, which leads to the equivalence of absorption and emission line profiles, valid in the case of a WD atmosphere?

The WDPE transmission data is extracted using both absorption and emission spectra, with the main contribution coming from the former (Falcon 2014; Falcon et al. 2015a). As discussed in Ch. 5, the WDPE Hβ and Hγ *transmission* data reproduces the plasma parameter trends mentioned in question one above. Such trends are not observed in the WDPE *emission* data (Montgomery et al. 2015). Taken at face value, do these results already imply a genuine difference between absorption and emission line profiles and therefore answer question two above? Maybe.

Before I jump to such conclusions, a thorough exploration of my experimental methods as well as the WDPE platform is needed. Ch. 5 details my investigations into possible plasma gradients present in my gas cell. I then use this result to simulate the effects of such a gradient on emergent absorption and emission line profiles, with a particular focus on Hβ and Hγ. An analysis of this simulation data shows that I can explain, *at most*, half of the experimentally determined differences in n_{e} between those two lines using gradient arguments.

What conclusions can I draw from this? It appears that even after a thorough investigation that includes gradient effects and WDPE data analysis methods, I cannot account for the difference between the inferred n_{e} from Hβ and Hγ. This result therefore points towards a genuine difference between absorption and emission in the WDPE. Other questions that have to be answered before I can come to a definitive conclusion about this are: Could this effect arise because complete redistribution does not apply to my plasma? Is some

major source of gradient within the platform unaccounted for? If both of these effects can be ruled out as sources for the absorption-emission disagreement, a series of astrophysical questions then follow: if the difference between absorption and emission is real, what does this mean for the inferred masses of WDs and their potential as galactic chronometers (see Ch. 3)? What are the consequences for all other astrophysical plasma models making this assumption? The answers to these questions are currently unknown.

It is clear from the above discussion that one obvious way forward is to further investigate the plasma gradients in the WDPE. This might be accomplished by placing the continuum LOS at various parts in the gas cell to obtain a n_e profile along the gold back wall. Since the differences in n_e derived from Hβ and Hγ are not a function of particle density, these experiments should be performed at a variety of fill-pressures and plasma conditions. The implications of this research are enormous and could potentially impact a wide range of plasma- and astrophysical topics.

8.2 Helium

Weaknesses in both mass determination methods for the DB WDs motivated my helium experiments. The GR mass determination approach suffers from incorrect $3d \rightarrow 2p$ He I 5876 Å Stark shift predictions. For over 6 decades, neither theory nor experiment have been able to agree on the sign and magnitude of the shift of that feature. This line is of extreme importance for DB GR measurements since it is the strongest line in the optical spectra of these stars

and can be used to determine the stellar mass using this method (Falcon et al. 2012). Since the WDPE addresses many of the issues encountered in previous shift measurements, my data can provide valuable insight into these theory-experiment disagreements. The analysis I present in Ch. 6 shows that many concerns raised about previous Stark shift measurements do not explain the difference between theory and experiment. This is evidenced by the excellent agreement between my measurements and those obtained by Gauthier et al. (1981) to within uncertainties. The agreement between these experiments and the notably smaller uncertainties reported here support the assertion that my results provide an accurate test for theory.

My helium data also allows me to investigate neutral broadening in plasmas, a potential weakness of the spectroscopic DB mass determination method. In Sec. 6.6, I show the neutral broadening model currently used by the WD community (Deridder & van Renspergen 1976) is inaccurate for the conditions found in DB atmospheres. This may have far-reaching consequences for DB WDs, as was demonstrated in Fig. 2.4. In combination with the Stark shift problems explained above, uncertainties in the Deridder & van Renspergen (1976) makes it difficult for observers to derive DB masses and thereby investigate the evolutionary origins of these stars. New theoretical models for both these atomic effects are needed.

Future helium shift experiments need to be expanded to lower and higher n_e so that the entire plasma parameter range found in a DB atmosphere can be probed and experimentally constrained. The neutral broadening

measurements are easily expandable to plasmas with varying concentrations of neutrals. This will then produce further constraints on any future theory attempting to account for neutral broadening in plasmas. Another question that future experiments may be able to answer is the influence of invisible hydrogen or helium on observed line profiles. The current experiments are too high in temperature to make either hydrogen or helium invisible, but small changes to the platform can remedy this problem and allow me to empirically constrain these important questions.

8.3 Carbon

The carbon experiments presented in Ch. 7 are aimed at validating the Stark width calculations of Dufour et al. (2011). Such calculations are needed to extract accurate masses of DQ WDs, which could hold the long lost key to the puzzle of Type Ia supernovae. The data and discussion I present in Ch. 7 proves that the WDPE, in a modified form, has the capability of reaching the temperatures and densities needed to perform these kinds of experiments.

Several hardware design flaws need to be solved in order for these experiments to function correctly. The boundary layer plasma needs to be removed and the temperature needs to be reduced. I've made initial forays into this subject by developing new platform designs and performing simulations to address the temperature issue. Once these problems are solved, the scientific significance of hot DQs can finally be realized.

Appendices

Appendix A

Fitting WD spectra to extract atmospheric parameters

Extracting WD parameters using the spectroscopic method requires many input parameters. The main body of this thesis deals with the atomic physics aspects of the spectroscopic approach. In this appendix, I describe my efforts at investigating another crucial ingredient in this process: fitting observed WD spectra with atmospheric models. The initial motivation for this investigation was to derive the effect of Xenomorph line profiles on inferred WD masses. I was thus required to develop a WD fitting algorithm. This is much easier said than done.

Members of the WD community currently adopt one of two fundamental spectroscopic atmospheric parameter extraction methods: fitting the entire, absolutely calibrated stellar spectrum (e.g. Koester et al. 2014) or performing the more traditional method of fitting individual lines (e.g. Bergeron et al. 1992; Liebert et al. 2005). Many different approaches to the individual line fitting method exist. Unfortunately, a detailed description of line fitting approaches are unpublished, to the best of my knowledge. This makes comparing results from different investigations extremely difficult. In this appendix, I

present an automated line normalization and extraction approach that could potentially serve as the basis against which to compare other parameter determination methods.

A.0.1 Extracting line individual line profiles

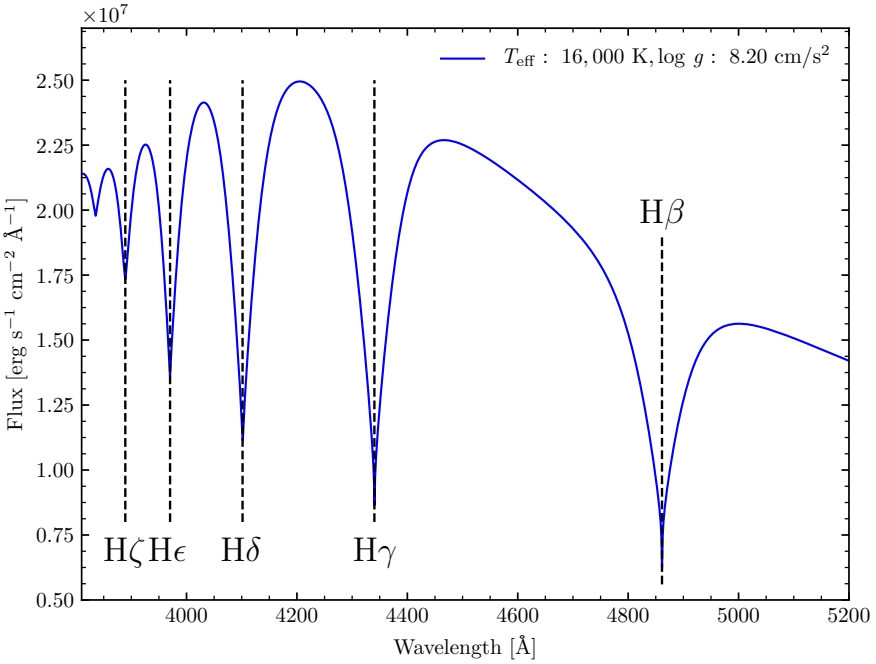

Figure A.1: A model atmosphere calculation performed at a $T_{\rm eff}$ of 16,000 K and a log g of 8.20 cm/s^2. This atmosphere was calculated with TLUSTY (Hubeny & Lanz 1995) with Vidal et al. (1973) hydrogen line profiles. No instrument broadening was applied to these spectra. I indicate the locations of major spectral features that I will use in the remainder of this appendix to demonstrate my line extraction method.

Extracting individual line profiles involves many more steps than fitting an entire absolutely calibrated WD observation. This is apparent from

Fig. A.1, where I show a model atmosphere calculation performed at a $T_{\rm eff}$ of 16,000 K and a log g of 8.20 cm/s^2. To convert this absolutely calibrated spectrum to individual line profiles, each feature (Hβ, Hγ, Hδ, etc.) in that figure has to be extracted and normalized. Throughout my graduate career, I've learned to appreciate the value of completely automated and uniform data analysis methods. Such an approach has several distinct advantages. First, it makes comparisons of individual studies possible. Second, fully automated approaches are generally more reproducible and reliable than those that allow for the influence of observer bias. I therefore attempted to develop an automated line extraction and normalization method. Throughout my investigations, it became obvious that Hβ and all other lines in the atmosphere (see Fig. A.1) need to be treated separately. The reason for this simple: Hβ usually has a well-defined continuum region on either side of the spectral feature. The same cannot be said about other lines in the spectrum (Hγ, Hδ, Hϵ, Hζ). They are clearly merged with their neighboring features and therefore cannot be normalized in the same way. I will begin with my treatment of Hβ.

A.0.2 Normalizing the Hβ profile

Instead of adopting the standard 280 Å line width for Hβ (Tremblay & Bergeron 2009), I developed a method that interactively determines the normalization bounds for this line. In my opinion, it is unreasonable to adopt static line widths in a spectral analysis that can cover 30,000 K in $T_{\rm eff}$ and 1.5 orders of magnitude in log g. My approach utilizes the slope of the continuum

regions around Hβ to determine the line width. I show a sample Hβ slope plot in Fig. A.2. The edges of the line are determined by finding the locations on either side of the Hβ center where the slope varies by less than 1.5% point to point. This limit was derived semi-empirically by performing tests using synthetic WD such as the ones shown in Fig. A.1 as input data. The derived line edges are plotted as red pentagons in Fig. A.2, while the standard line width (280 Å) is shown with green dots. Clearly, my method produces wider lines than the standard approach. This disagreement is expected to grow as $T_{\rm eff}$ decreases and log g increases. Hence, adopting a static width for *all* lines at all $T_{\rm eff}$ and log g combinations may lead to inaccurate results, since the far wings of the Hβ are removed. These wings, however, hold a lot of physical information that should not be discarded so readily. My method increases the total Hβ FWHM by $\sim$7%.

Now that the line edges have been determined, how is the line profile to be properly normalized? Some of the difficulties associated with that procedure are discussed in Ch. 5. I show two possible normalization schemes (linear: orange and quadratic: purple) in Fig. A.3. From this figure, it is clear that the quadratic spline continuum fitting method (purple) is fraught with problems, leading me to adopt the linear continuum fitting method (orange) for the rest of this appendix. The influence of the line normalization width on the final derived profile will be discussed in Sec. A.0.4.

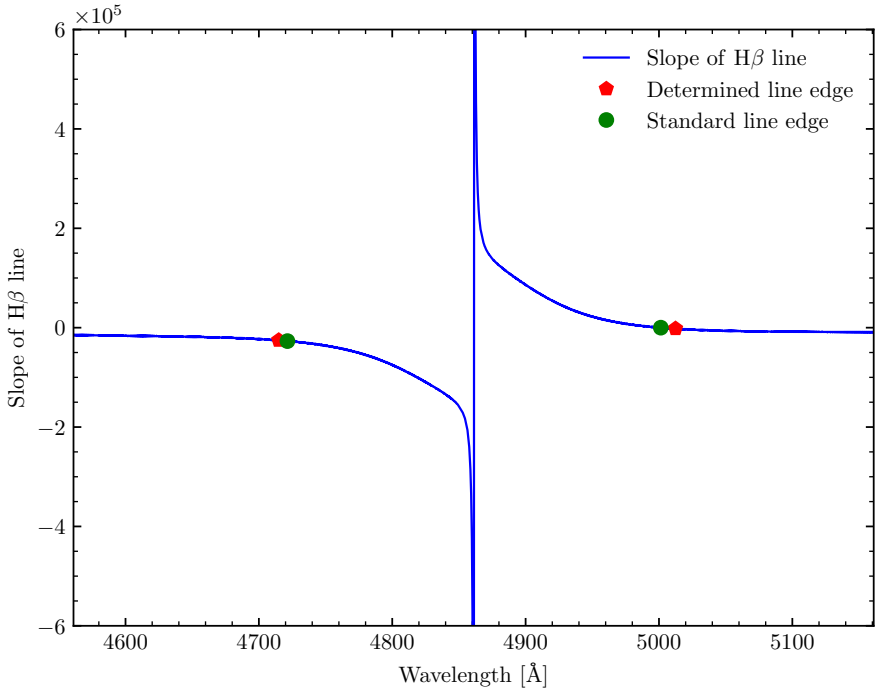

Figure A.2: Calculated slopes of the Hβ line at a $T_{\rm eff}$ of 16,000 K and a log g of 8.20 cm/s^2. The standard line width is plotted using green dots, while the width inferred from my method is given as red pentagons. These two edge determinations clearly differ. No instrument broadening was applied to these spectra.

A.0.3 Normalizing all other lines

The method for normalizing Hβ discussed in Sec. A.3 clearly is not applicable to any other lines since there are no available continuum regions to define line edges. Instead, one can find the peaks between the lines, fit a linear continuum to those points and then extract the normalized line profile. However, this problem is again a bit more complicated than it seems. The higher order lines are themselves on a sloped background caused by the

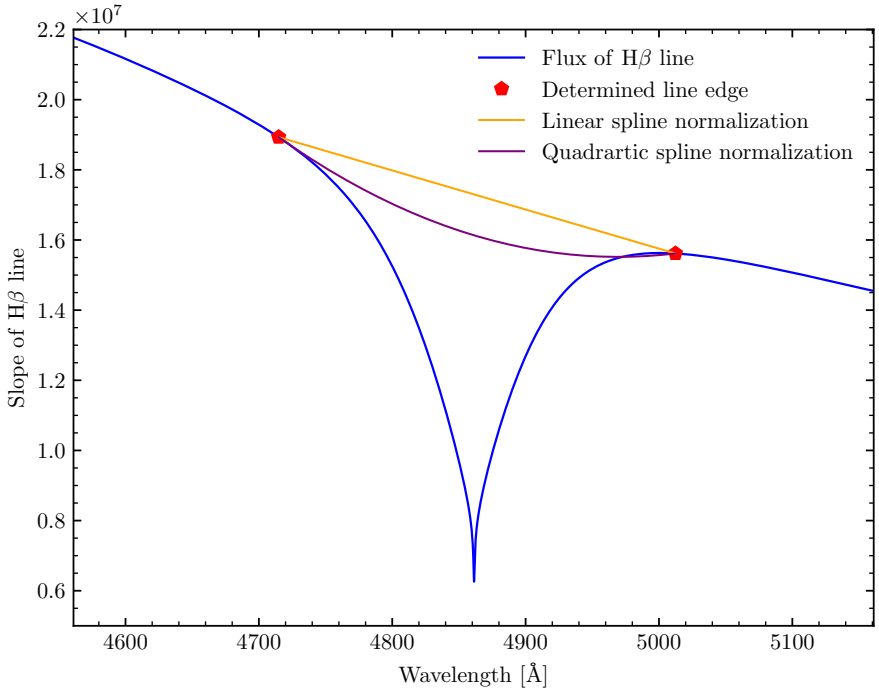

Figure A.3: Sample normalization for Hβ. The line end-points are determined using the method described above. I fit a linear (orange) spline function to the data outside the line to obtain a continuum and also a quadratic spline (purple). The linear fit is much less prone to odd behavior, leading me to adopt this fit for the automated method.

underlying blackbody distribution of the stellar temperature. Thus, simply fitting the peaks in-between lines may lead to fits that exclude the far wings of the lines. Adopting a fixed width for these features may lead to inclusions of neighboring lines in the normalized profile. This is undesirable and should be addressed by using an automated approach. My method first locates the maximum flux on either side of a spectral feature and fits a line to those two points. The automated routine then checks to see if any portion of the linear

fit is *below* the model atmosphere flux. If it is, appropriate corrections are made until the linear fit covers the line only. The results of such an approach are plotted in Fig. A.4. Initial line widths are shown using green dots, while the red connected squares show the final line edges and associated normalization continua in that figure. The line widths using this automated method are generally wider than the standard method by ∼5-7%.

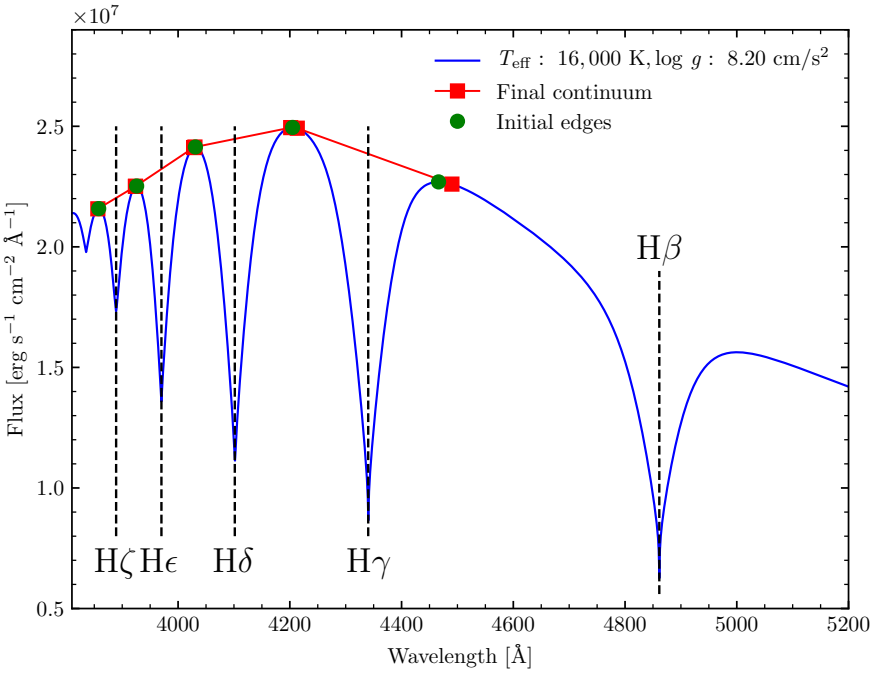

Figure A.4: Sample normalization of the higher-order Balmer lines in a WD atmosphere. The initial line edges are shown as green dots, while the final line edges and continua are given in red. Line widths resulting from this method are about 10% wider than those of the standard method.

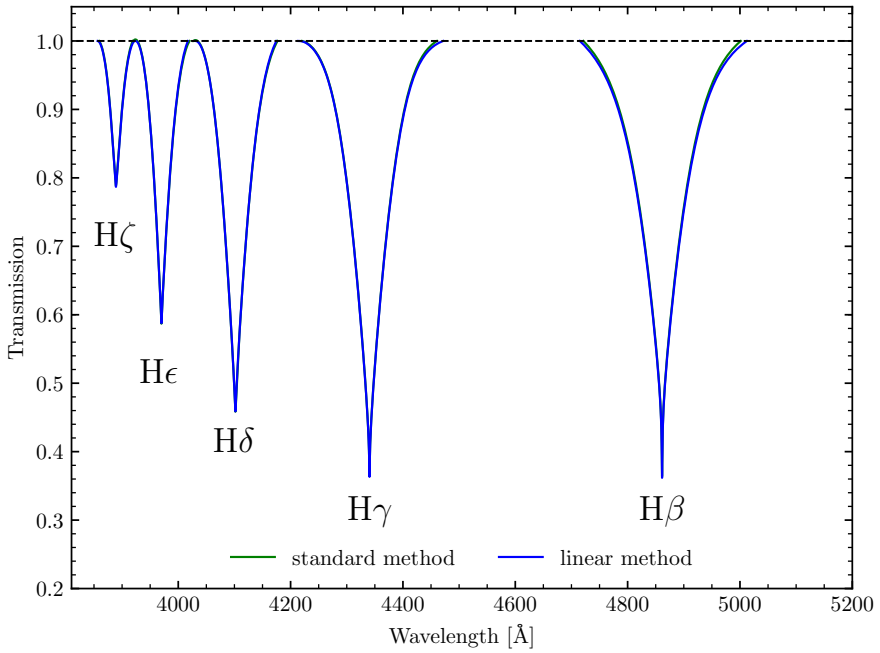

Figure A.5: Comparison of line profiles derived using the 'standard' method and my automated routines. The standard results are given in blue, while the linearly normalized lines resulting from my automated routines are given in green. The widths of my normalized lines are about 10% larger than those resulting from the standard method. No instrument broadening was applied to these spectra.

A.0.4 Comparing results from the standard method and my automated routines

The hallmark of any automated routines is to reproduce results that were achieved under the guidance of humans. Fig. A.5 shows the comparison between line-shapes stemming from the standard approach to those derived using my approach. Clearly, my derived lines match those of the standard methods quite nicely. However, upon closer inspection, it becomes obvious

that the lines I derive are broader than those of the standard approach. A full and complete analysis of the effects of such an automated line normalization approach on derived WD atmospheric parameters has yet to be completed. The machinery to perform such a comparison is already in place. Furthermore, my proposed method is fully automated and could therefore serve as an anchor point for any future studies extracting WD parameters with the spectroscopic method.

Appendix B

Precise laser wavelengths

The WDPE data reduction routines rely on accurate knowledge of laser wavelengths. This is especially true of the helium work presented in Ch. 6. I therefore discuss all WDPE lasers in this appendix.

Each laser transition has two wavelengths associated with it: those measured in vacuum and those measured in air. Both wavelengths are presented here. The transformation from vacuum to air wavelength was performed using the approach presented in Morton (2000) and Birch & Downs (1994). I adopt the recommended constants presented in Eq. 8 of Morton (2000). Based on the uncertainty in the index of refraction of air and the lasing energy levels, I estimate the total laser wavelength error in air to be $\sim$0.002 Å.

B.1 Film data lasers

The WDPE film data is reduced and calibrated using the lasers listed in Table B.1. The blue laser in that table employs the Ar II 4p $\rightarrow$ 4s transition with an upper level energy of 19.972 eV and a lower level energy of 17.266 eV (Whaling et al. 1995) to produce its emission. The laser line of the green He-Ne system given in Table B.1 results from the Ne I 5s $\rightarrow$ 3p transition with an

upper level energy of 20.662 eV and a lower level energy of 18.382 eV (Burns et al. 1950).

Table B.1: Laser models and wavelengths used on the film WDPE data

Model	**Color**	λ_{air} [**Å**]	λ_{vac} [**Å**]	**Source**
Modu Laser Stellar Pro 457/10	blue	4579.349	4580.633	1
Melles Griot 25 LGR 193	green	5433.651	5435.161	2

1: Whaling et al. (1995)
2: Burns et al. (1950)

B.2 CCD data lasers

I use a Research Electro Optics 30602 tunable laser to perform the wavelength calibration of the CCD data. This laser is a He-Ne system with colors, wavelengths, and energies listed in Table B.2. Each entry given in that table is produced by a Ne 5s $\rightarrow$ 3p transition.

Table B.2: Laser models and wavelengths used on the CCD WDPE data

Color	λ_{air} [**Å**]	λ_{vac} [**Å**]	**UL energy [eV]**	**LL energy**	**Source**
green	5433.651	5435.161	20.662	18.382	2
yellow	5944.834	5946.481	20.662	18.576	2
orange	6046.135	6047.807	20.662	18.613	2
orange-red	6118.019	6119.708	20.662	18.637	3
red	6328.165	6329.914	20.662	18.704	2

2: Burns et al. (1950)
3: NIST website: `https://physics.nist.gov/PhysRefData/ASD/lines_form.html`

Appendix C

Slow sweep vs. fast sweep CCD data

The Sydor ROSS5100 CCD coupled streak cameras are used to collected WDPE He shift data. These systems are claimed to be more sensitive than their film counterparts and therefore allow for the collection of the higher-resolution spectra needed for the He shift measurements. As mentioned in Ch. 4, the Sydor cameras can collect data at several different sweep speeds. WDPE data is collected using a 500 ns data collection window.

The He shift measurements require a highly accurate wavelength calibration. I therefore attempted to incorporate the spectrum of an Oriel Mercury Argon (model 6035) calibration pen lamp into my wavelength calibration procedure. Due to the weak signal produced by that lamp, its spectrum has to be collected at a sweep speed of 8 seconds. The resulting wavelength calibration did not match that of laser lines collected at 500 ns. To investigate this effect, I also collected laser lines with the 8 second data collection window. The differences in the two spectra are shown in Fig. C.1.

The wavelength calibration relationship between the 500 ns and 8 second window is not linear, as is clearly seen in Fig. C.1. I invested significant amounts of time and energy trying to rectify this situation but was unable to

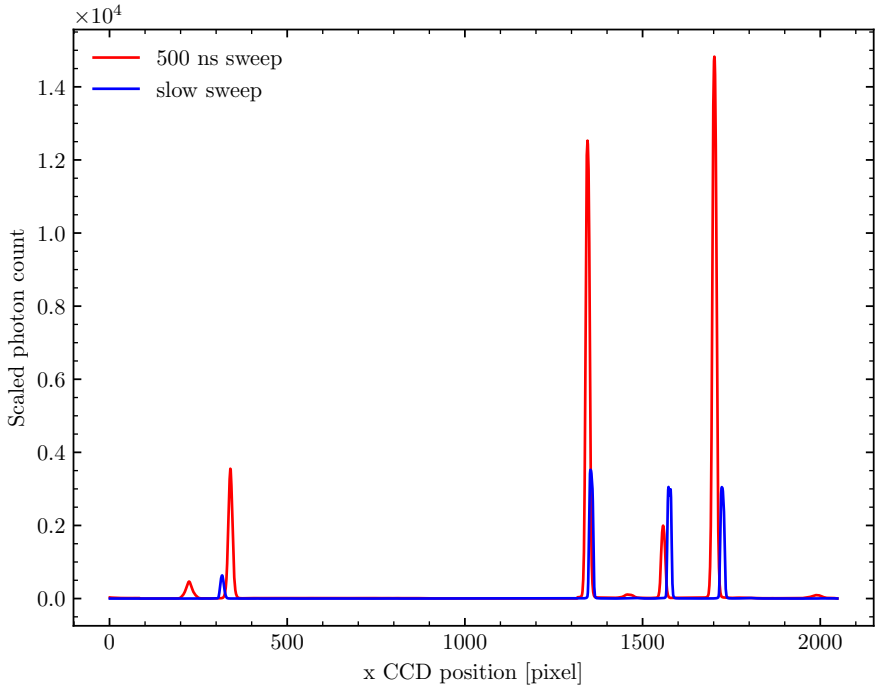

Figure C.1: A comparison of laser locations captured using a 500 ns sweep window (blue) and a 8 sec sweep window (red). Differences in the peak locations of the lasers are obvious.

do so. Therefore, the mercury argon spectra collected at the 8 second sweep speed are not ideal to derive a wavelength calibration of the He shift data.

Appendix D

Determining the true shape of the LDLS

In this appendix, I outline a procedure to determine the spectral power distribution of the LDLS in a reproducible manner. For the WDPE, this distribution serves as a fiducial to determine the shape of my data after it has passed through an SVS system. By dividing the shape of the data on the SVS film and the spectral power distribution of the LDLS, I obtain an instrumental response, which is of crucial importance in determining the absolute response and relative intensity of my data. A reliable procedure that results in a reproducible and smooth LDLS shape is discussed in Sec. D.1.

D.1 Measuring the LDLS spectral power distribution

The most straightforward procedure to measure the spectral power distribution of the LDLS requires the following equipment:

1. LDLS (I used LDLS # 2, make & model: Energetiq EQ-99FC[1], DOE property number: B166913, power supply S/N: 708, remote S/N: 616 with appropriate core-diameter SMA–ST optical fiber (all data presented in this report were obtained using a 100-μm diameter fiber))

[1] http://www.energetiq.com/DataSheets/EQ99FC_Data_Sheet.pdf

2. Newport bandpass filters ranging from minimum to maximum wavelength of shape determination. The nominal wavelength coverage is 380 nm to 700 nm (Newport model #: 10BPF10-380 - 10BPF10-700)

3. StellarNet spectrometer with integrating sphere attached (StellarNet model: BlackComet CXR-25, S/N: 12091132 BW16)

4. Thorlabs power meter (I used model PM200 (S/N: P3001207) with bandwidth set to 10 Hz and attenuation set to 0 dB.)

5. Thorlabs power sensor/head

6. Optical setup similar to that shown in Fig. D.1. All screws on this construction need to be securely fastened. The power sensor will need to be removed and re-attached to this setup for each bandpass filter. If the screws on this construction are not tightened, angular variations in the measurements could result.

Using the above items, one simply has to measure the transmission spectra of each bandpass filter and their associated total output power. These two datasets then allow easy calculation of the LDLS spectral power distribution. During my many attempts at measuring the LDLS shape, I noticed an azimuthal dependence of the Newport bandpass filters (see above) on the total transmitted power, as well as some disagreements in the central wavelengths of the filters. Further testing showed that the stated central wavelength of a filter agrees to within 2 Å of the measured wavelength. The dependence of

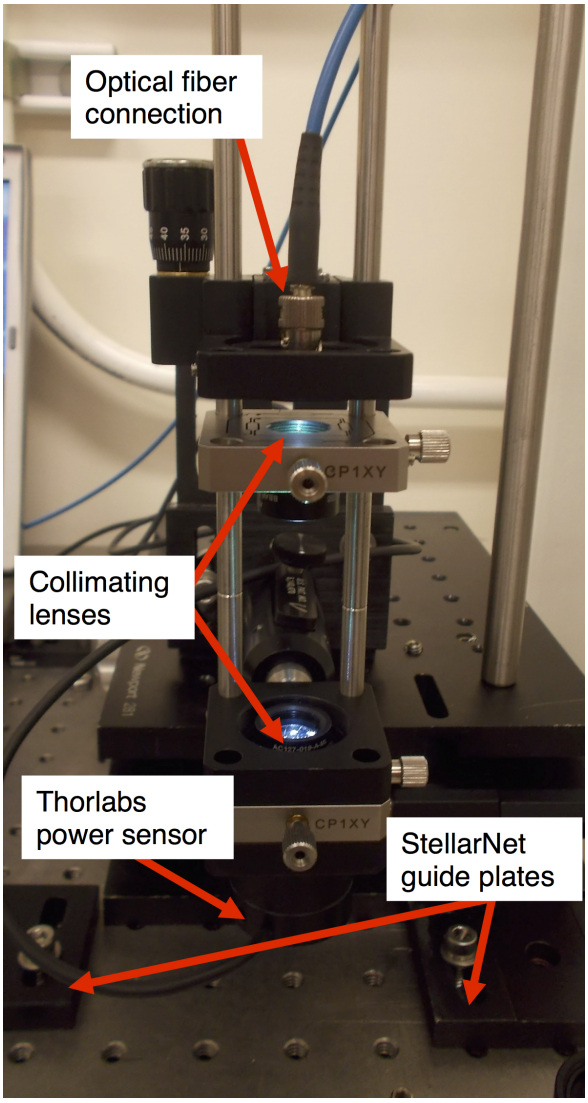

Figure D.1: Optical setup used to measure LDLS spectral power distribution

the azimuthal positioning of each filter in the optical setup shown in Fig. D.1 is summarized in Table D.1

Based on the above considerations, my recommended procedure is as

Table D.1: Azimuthal dependences of bandpass filter transmission in percent

Bandpass wavelength	**Azimuthal dependence (%)**	**Bandpass wavelength**	**Azimuthal dependence (%)**
380	0.5	550	1.1
390	–	560	2.8
400	–	570	1.6
410	0.5	580	0.4
420	0.7	590	–
430	0.4	600	1.5
440	0.4	610	1.4
450	1.5	620	1.2
460	0.3	630	1.2
470	1.0	640	1.1
480	1.1	650	1.2
490	1.1	660	1.2
500	0.9	670	0.8
510	0.3	680	0.7
520	–	690	1.6
530	1.2	700	0.6
540	0.7		

follows:

1. Allow LDLS to warm up for $\sim$ 1h. This will eliminate any short-term power variations.

2. Connect the LDLS to an optical setup comparable to that shown in Fig. D.1. Position the StellarNet spectrometer under this setup and adjust the StellarNet guide plates so that the maximum amount of light enters the integrating sphere located at the entrance of the spectrometer. The

use of these guide plates will become apparent later.

3. Before acquiring any data, try to eliminate any stray light that could possibly influence the measurements. For my final measurements, I turned off all lights in the SVS lab. Additionally, please ensure that all covers of the integrating sphere are tightly screwed on. To cover the ST connection of the integrating sphere, I connected an optical fiber to that port and covered its opposite end with a black rubber cap.

4. For each bandpass filter:

   (a) Attach Thorlabs power sensor to bottom of optical setup and measure the unfiltered power for the current wavelength. While not used explicitly in later processing, these 'no-filter' power measurements provide invaluable data in case the measurement should be flawed.

   (b) Place bandpass filter for current wavelength between the upper and lower collimating lens holder with the shiny metallic side pointing towards the optical fiber. Turn filter azimuthally until maximum transmitted power has been achieved. Record this maximum transmitted power.

   (c) Remove power sensor and perform a dark correction on the StellarNet spectrometer. It is crucial that this correction be performed before every spectrum is acquired as residual light may still be in

the integrating sphere (i.e., you will notice an afterglow in the integrating sphere from previous data collection. This extra light needs to be properly accounted for).

(d) Using the guide plates, slide StellarNet into position and obtain bandpass filter spectrum. I found that the optimal integration time for our particular setup is 165 ms, and an average of 20 iterations.

(e) Remove bandpass filter and obtain the unfiltered spectrum. The purposes of this unfiltered spectrum is to account for any small LDLS variations on the scale of a few minutes.

(f) Repeat above steps for each bandpass filter.

If the steps above are closely followed, an LDLS spectrum as shown in Fig. 4.6 is easily calculated by dividing the bandpass filter power collected in step 5(b) by the integrated bandpass filter spectrum obtained in step 5(d)/(e).

Appendix E

The Full-Width-at-Half-Area n_e extraction method

E.1 n_e determination methodology

Deriving the n_e at various locations in my gas cell is crucial for constraining plasma inhomogeneities in the WDPE. The absorption optical path can be used to extract the integrated n_e along the gold wall, while the continuum LOS allows for an n_e measurement at the very edge of the gas cell (see Fig. 3.9). These two data points serve as an important constraint for the T_e and n_e trends along the absorption and emission LOS. In my previous work, I employed an n_e extraction approach that relied on absolutely calibrated emission-corrected absorption spectra to which I fit detailed line-shape calculations (Falcon et al. 2015b,a). While this method produces highly accurate results, it also relies on many complicated calibration measurements. Furthermore, an absorption and emission dataset of the same plasma are required to extract the desired n_e values.

The design of the WDPE does not allow for the observation of an emission spectrum along the continuum LOS path. The above described method of extracting n_e values is therefore not applicable. An obvious alternative is

the full-width-at-half-max (FWHM) metric for Hβ (e.g., Vidal et al. 1973; Gigosos & Cardeñoso 1996; Lemke 1997). However, the experimental spectral features are optically thick in their cores and also suffer from the influence of plasma inhomogeneities in the line centers. The combination of these effects make the FWHM measurement a suboptimal $n_{\rm e}$ derivation method. A more appropriate $n_{\rm e}$ extraction approach for my data is the full-width-at-half-area (FWHA) technique discussed in, amongst other papers, Gigosos et al. (2003). The FWHA method relies on the integration of the entire line profile and subsequent determination of limits that reduce the integral to 50% of its initial value. The FWHA method has several advantages over the FWHM approach. From a theoretical standpoint, the FWHA method is much less susceptible to inaccuracies in the ion-dynamics and electron-broadening approximations of the line-shape calculation. Ion-dynamics are especially important for the Hβ line that is being used as an electron density diagnostic in this paper. From an experimental point of view, the FWHA method is less sensitive to optical depth and plasma gradient effects compared to a FWHM approach.

To demonstrate that the FWHA method produces $n_{\rm e}$ results comparable to my detailed line-shape fits, I compared the results of the two techniques using shot z2553 (Falcon et al. 2015b). To extract the FWHA $n_{\rm e}$ values from z2553, I first normalized the experimental Hβ absorption line. This converts the spectral feature to transmission and in my final step I convert to optical depth units. Fig. E.1 shows representative experimental Hβ profiles at different times. I also display the FWHA limits of the observed line-profile (black

dashed lines) as well as Voigt line-profile fits. Several claims made in the previous paragraph are now evident: early in time (0 ns, left panel of Fig. E.1), the Hβ profile does not appear to be afflicted by any self-emission or gradient effects. This is evidenced by the good agreement between the Voigt fit and experimental data for 0 ns. At 80 ns (right panel of Fig. E.1), gradients and self-emission effects decrease the agreement between the Voigt fit and the experimental data.

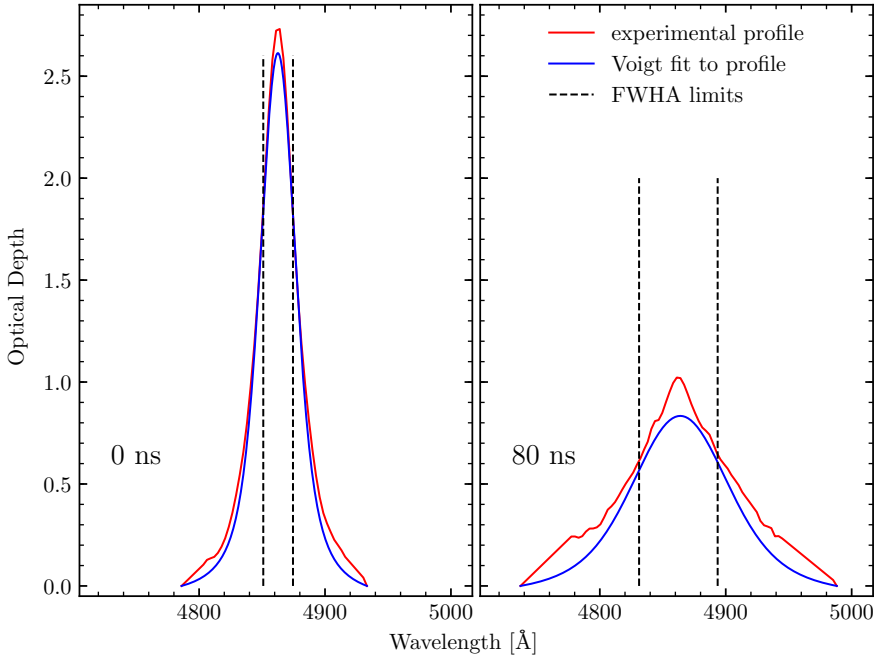

Figure E.1: Absorption line transmission profiles for two different time steps in my experiment. These profiles are from shot z2553. I also show fits of a Voigt profile to my data, as well as FWHA limits for the experimental profile.

An analysis of theoretical line-profiles is required to translate the FWHA values determined from the experimental features into n_e values. Accounting

for instrumental effects in my data is now required. I use the Xenomorph line-profiles (Gomez et al. 2016) to derive the FWHA-n_e relation. As is the standard in the theory community, these line-shapes are area-normalized. To extract transmission spectra from these calculations, I multiply the area-normalized theoretical line-profile by the integral value of the experimental feature and take the exponential of that product. I then convolve the synthetic spectrum with a 12 Å Gaussian that mirrors the instrumental broadening. Since this broadening is much smaller than the nominal line width for my experimental Hβ profiles ($\sim$ 60 Å), I do not expect this step to influence my derived n_e values. The instrumentally-broadened theoretical transmission profile is then converted back to optical depth and used to extract the desired FWHA-n_e relationship. This process is repeated for all available theoretical Hβ line profiles at temperatures ranging from $\sim$0.7 eV - $\sim$1.9 eV that were calculated under the assumption of a pure hydrogen plasma. Fig. E.2 shows the final FWHA-n_e relationship I derive from the approach. The n_e region applicable to the WDPE is highlighted in green. Since the FWHA is almost exclusively a function of plasma n_e, temperature effects can be ignored (see e.g., Table 25 of Gigosos & Cardeñoso 1996).

Now that I have fully described my method of extracting a FWHA-n_e relationship from the Gigosos et al. (2003) line profile calculations, I will apply it to shot z2553. The results of this analysis are shown in Fig. 5.9.

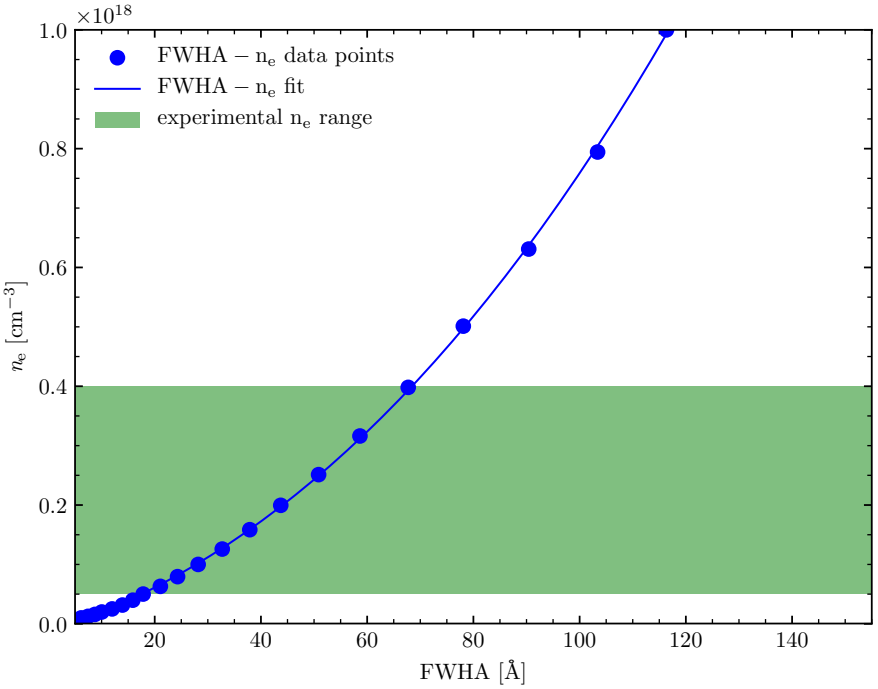

Figure E.2: The nominal FWHA-n_e relationship resulting from my analysis of the Xenomorph data. I show the data points extracted from the Gomez et al. (2016) profiles, as well as the 2nd order polynomial fit to those points. Clearly, the 2nd order fit nicely reproduces the data points. The n_e region covered by the experiment is highlighted in green.

Appendix F

Experiment Log

This appendix contains all shots that were performed as part of this thesis. An overview of all shots is given in Sec. F.1, while comments on select shots are given in Sec. F.2.

F.1 Overview of all shots

Table F.1: Log of all experiments performed for this thesis

Shot #	gas pressure/fill	LOS distance	cell type	collected data
		July 2015 series		
z2832	10 T H_2	5 mm	12 cm OBS	Abs; Em
z2833	20 T H_2	5 mm	12 cm OBS	Abs; Con
z2834	20 T H_2	5 mm	12 cm OBS	Abs; Em
z2835	50 T H_2	5 mm	12 cm OBS	Abs; Em
		October 2015 series		
z2870	10 T He	10 mm	12 cm OBS	Abs; Em
z2871	30 T H_2	5 mm	9 cm OBS	Abs; Em
z2872	10 T H_2	10 mm	9 cm OBS	Abs; Con
z2873	30 T H_2	5 mm	9 cm OBS	Abs; Em
		March 2016 series		
z2924	20 T H/He	5 mm	12 cm OBS	Abs; Em
z2926	20 T H/He	5 mm	12 cm OBS	Abs; Em
		May 2016 series		
z2950	40 T H/He	5 mm	12 cm OBS	Abs; Em
z2951	20 T H/He	5 mm	8 cm WBS	Abs

Continued on next page

Table F.1 – *Continued from previous page*

Shot #	gas pressure/fill	LOS distance	cell type	collected data
z2952	10 T H/He	10 mm	8 cm WBS	Abs; Em
z2954	20 T H/He	10 mm	12 cm OBS	Abs; Con
		June 2016 series		
z2971	5 T CH_4	5 mm	8 cm WBS	Abs; Em
z2972	5 T CH_4	5 mm	8 cm WBS	Abs; Em
z2973	10 T He	10 mm	12 cm OBS	Abs; Con
		Feburary 2017 series		
z3053	5 T CH_4	10 mm	8 cm WBS	Abs; Em
z3054	20 T H/He	5 mm	12 cm OBS	Abs; Em
z3055	5 T CH_4	10 mm	8 cm WBS	Abs; Em
		May 2017 series		
z3091	20 T H/He	5 mm	12 cm OBS	Abs; Em
z3093	10 T He	10 mm	12 cm OBS	Abs; Em
z3094	20 T H/He	10 mm	12 cm OBS	Abs; Con
z3095	20 T H/He	5 mm	12 cm OBS	Abs; Em
		September 2017 series		
z3139	20 T H/He	10 mm	12 cm OBS	Abs; Con
z3140	17.5 T H/He	5 mm	12 cm OBS	Abs; Em
z3141	20 T H/He	10 mm	12 cm OBS	Abs; Em
		January 2018 series		
z3193	10 T H_2	10 mm	12 cm OBS	Abs; Em
z3194	20 T H/He	10 mm	12 cm OBS	Abs; Em
z3195	20 T H/He	10 mm	12 cm OBS	Abs; Em
z3196	10 T H_2	10 mm	12 cm OBS	Abs; Em
z3197	10 T He	10 mm	12 cm OBS	Abs; Em

F.2 Detailed comments all shots performed for this thesis

Detailed comments for all shots in Table F.1 are given below. I discuss each shot series separately.

F.2.1 July 2015

z2832

Data quality: Good data, some contaminants.

Data status: Fully analyzed and published in Falcon et al. (2017).

z2833

Data quality: Good data, no contaminants.

Data status: Reduced and analyzed. Used in calibration of z2832.

z2834

Data quality: Saturated data, no contaminants.

Data status: Not reduced or analyzed due to saturation issue.

z2835

Data quality: Very saturated data, no contaminants.

Data status: Not reduced or analyzed due to saturation issue.'

F.2.2 October 2015

z2870

Data quality: No emission data due to faulty fiber; absorption data shows no He lines.

Data status: Not reduced or analyzed due to above issues.

z2871

Data quality: No data due to burst Mylar window during gas fill procedure.

Data status: Not reduced or analyzed due to above issues.

z2872

Data quality: Good data, no contaminants.

Data status: Data reduced.

z2873

Data quality: Good data, no contaminants.

Data status: Data not reduced due to compromised absorption step wedge.

F.2.3 March 2016

z2924

Data quality: Good data, but timing issues prevented full analysis of data.

Data status: Dara reduced and analyzed as fully as possible.

z2926

Data quality: No data due to leaking gas cell.

Data status: Not reduced or analyzed due to above issues.

F.2.4 May 2016

z2950

Data quality: No emission data due to optics misalignment.

Data status: Not reduced or analyzed due to above issues.

z2951

Data quality: Good absorption data. I elected not to collect emission data.

Data status: Reduced and analyzed. Used to inform decisions about future within blast shield shots.

z2952

Data quality: Good data, no contaminants.

Data status: Reduced and analyzed. Used to inform decisions about future within blast shield shots.

z2954

Data quality: Good data, no contaminants.

Data status: Reduced and analyzed. Used in calibration of z2952.

F.2.5 June 2016

z2971

Data quality: Good data, but unusable due to timing issue.

Data status: Reduced. Used for line identification purposes.

z2972

Data quality: Good data, no contaminants.

Data status: Reduced and analyzed. See Ch. 7 for results.

z2973

Data quality: Good data, no contaminants.

Data status: Reduced and analyzed. Used in calibration of z2972.

F.2.6 February 2017

z3053

Data quality: Good emission data, but unusable due to timing issues. Absorption camera did not collect any data.

Data status: Reduced. Used for line identification purposes.

z3054

Data quality: Weak data.

Data status: Reduced and analyzed. Used to inform future direction of He shift shots.

z3055

Data quality: No data since SVS cameras were not armed.

Data status: Not reduced or analyzed due to above issues.

F.2.7 May 2017

z3091

Data quality: Good data, but no He lines.

Data status: Not reduced or analyzed due to above issues.

z3092

Data quality: No data due to heavily leaking cell.

Data status: Not reduced or analyzed due to above issues.

z3093

Data quality: Good data, but no He lines.

Data status: Not reduced or analyzed due to above issues.

z3094

Data quality: Good data, no contaminants.

Data status: Reduced and analyzed. Used in calibration of z3095.

z3095

Data quality: Good data, no contaminants.

Data status: Reduced and analyzed. Used to inform future direction of He shift shots.

F.2.8 September 2017

z3139

Data quality: Good data, no contaminants.

Data status: Reduced and analyzed. Not used in any calibration.

z3140

Data quality: Good data, but absorption turns into emission.

Data status: Reduced and analyzed. Used to inform future direction of He shift shots. See Ch. 6 for more details.

z3141

Data quality: Good data, but absorption turns into emission.

Data status: Reduced and analyzed. Used to inform future direction of He shift shots. See Ch. 6 for more details.

F.2.9 January 2018

z3193

Data quality: Good data, no contaminants.

Data status: Reduced and analyzed. Used to investigate plasma inhomogeneities in the WDPE.

z3194

Data quality: Good data, no contaminants.

Data status: Reduced and analyzed. No reliable n_e diagnostic.

z3195

Data quality: Good data, no contaminants.

Data status: Reduced and analyzed. See Ch. 6 for full results.

z3196

Data quality: Good data, no contaminants.

Data status: Reduced and analyzed. Used to investigate plasma inhomogeneities in the WDPE.

z3197

Data quality: Good data, no contaminants.

Data status: Reduced and analyzed.

Bibliography

Adams, W. S. 1925, Proc. Natl. Acad. Sci. U.S.A., 11, 382

Ahmed, M. W., Choi, S., Lyakhov, K., et al. 2017, Plasma Phys. Rep., 43, 381

Alcock, C., Fristrom, C. C., & Siegelman, R. 1986, Astrophys. J., 302, 462

Althaus, L. G., García-Berro, E., Córsico, A. H., Miller Bertolami, M. M., & Romero, A. D. 2009, Astrophys. J. Lett., 693, L23

Auer, L. H. & Woolf, N. J. 1965, Astrophys. J., 142, 182

Bailey, J. E., Chandler, G. A., Mancini, R. C., et al. 2006, Phys. Plasmas, 13, 056301

Barstow, M. A., Barstow, J. K., Casewell, S. L., Holberg, J. B., & Hubeny, I. 2014, Mon. Not. R. Astron. Soc., 440, 1607

Barstow, M. A., Bond, H. E., Holberg, J. B., et al. 2005, Mon. Not. R. Astron. Soc., 362, 1134

Barstow, M. A., Joyce, S., Casewell, S. L., et al. 2017, in 20th European Workshop on White Dwarfs, Vol. 509, Warwick, UK, 383

Beauchamp, A. 1995, PhD thesis, Universite de Montreal, Montreal, CA

Beauchamp, A., Wesemael, F., & Bergeron, P. 1997, Astrophys. J., Suppl. Ser., 108, 559

Bennett, C. L., Halpern, M., Hinshaw, G., et al. 2003, Astrophys. J., Suppl. Ser., 148, 1

Berg, H. F., Ali, A. W., Lincke, R., & Griem, H. R. 1962, Phys. Rev., 125, 199

Bergeron, P. 1993, in White Dwarfs: Advances in Observation and Theory, Vol. 403 (Leicester, UK: Kluwer Academic Publishers), 267

Bergeron, P., Saffer, R. A., & Liebert, J. 1992, Astrophys. J., 394, 228

Bergeron, P., Wesemael, F., Dufour, P., et al. 2011, Astrophys. J., 737, 28

Beswick, J. A. & Glass-Maujean, M. 1987, Phys. Rev. A, 35, 3339

Bethe, H. A. 1939, Phys. Rev., 55, 434

Birch, K. P. & Downs, M. J. 1994, Metrologia, 31, 315

Bond, H. E., Schaefer, G. H., Gilliland, R. L., et al. 2017, Astrophys. J., 840, 70

Bradley, P. A. 1998, in Bulletin of the American Astronomical Society, Vol. 193, 37.07

Bragaglia, A., Renzini, A., & Bergeron, P. 1995, Astrophys. J., 443, 735

Brown, W. R., Gianninas, A., Kilic, M., Kenyon, S. J., & Allende Prieto, C. 2016, Astrophys. J., 818, 155

Burleigh, M. R., Jordan, S., & Schweizer, W. 1999, Astrophys. J. Lett., 510, L37

Burns, K., Adams, K. B., & Longwell, J. 1950, J. Opt. Soc. Am., 40, 339

Büscher, S., Glenzer, S., Wrubel, T., & Kunze, H.-J. 1995, J. Quant. Spectrosc. Radiat. Transf., 54, 73

Camisassa, M. E., Althaus, L. G., Rohrmann, R. D., García–Berro, E., & Córsico, A. H. 2017, in 20th European Workshop on White Dwarfs, Vol. 509 (Warwick, UK: ASPC), 429

Clemens, J. C. 1995, in Proceedings of the 9th European Workshop on White Dwarfs Held at Kiel, Germany, 29 August - 1 September 1994, Vol. 443, 294

Cooper, J. & Oertel, G. K. 1969, Phys. Rev., 180, 286

Córsico, A. H., Romero, A. D., Althaus, L. G., & García-Berro, E. 2009, Astron. Astrophys., 506, 835

Cummings, J. D., Kalirai, J. S., Tremblay, P.-E., & Ramirez-Ruiz, E. 2015, Astrophys. J., 807, 90

Cummings, J. D., Kalirai, J. S., Tremblay, P.-E., & Ramirez-Ruiz, E. 2016, Astrophys. J., 818, 84

De Loore, C. W. H. & Doom, C. 1992, Structure and evolution of single and binary stars, Vol. 179 (Boston, MA: Kluwer Academic Publishers)

Debes, J. H. & Sigurdsson, S. 2002, Astrophys. J., 572, 556

Deridder, G. & van Renspergen, W. 1976, Astron. Astrophys. Suppl. Ser., 23, 147

Dimitrijevic, M. S. & Sahal-Brechot, S. 1990, Astron. Astrophys. Suppl. Ser., 82, 519

Dolan, D. H., Ao, T., & Grant, S. C. 2016, Sandia Matlab AnalysiS Hierarchy toolbox v. 1.0, Tech. Rep. SAND2016-6848, Sandia National Laboratories

Draine, B. T. 2011, Physics of the Interstellar and Intergalactic Medium (Princeton, NJ: Princeton University Press)

Dufour, P., Ben Nessib, N., Sahal-Bréchot, S., & Dimitrijević, M. S. 2011, Balt. Astron., 20, 511

Dufour, P., Fontaine, G., Liebert, J., Schmidt, G. D., & Behara, N. 2008, Astrophys. J., 683, 978

Dufour, P., Liebert, J., Fontaine, G., & Behara, N. 2007, Nature, 450, 522

Dufour, P., Vornanen, T., Bergeron, P., & Fontaine, A., B. 2013, in 18th European White Dwarf Workshop. Proceedings of a conference held 13-17 August, 2012, at the Pedagogical University of Cracow, Poland, Vol. 469, Crakow, Poland, 167

Eisenstein, D. J., Liebert, J., Koester, D., et al. 2006, Astron. J., 132, 676

Falcon, R. E. 2014, PhD, University of Texas at Austin

Falcon, R. E., Bailey, J. E., Gomez, T. A., et al. 2017, in Proceedings of a conference held at University of Warwick, Coventry, West Midlands, United Kingdom, 25-29 July 2016, Vol. 509, eprint: arXiv:1609.09101, 149

Falcon, R. E., Bliss, D. E., Carlson, A. L., et al. 2015a, Calibration of Streaked Visible Spectroscopy at the Z Facility for a Plasma Experiment Creating White Dwarf Photospheres, Tech. Rep. SAND2015-3955, Sandia National Laboratories

Falcon, R. E., Rochau, G. A., Bailey, J. E., et al. 2013, High Energ. Dens. Phys., 9, 82

Falcon, R. E., Rochau, G. A., Bailey, J. E., et al. 2015b, Astrophys. J., 806, 214

Falcon, R. E., Winget, D. E., Montgomery, M. H., & Williams, K. A. 2010, Astrophys. J., 712, 585

Falcon, R. E., Winget, D. E., Montgomery, M. H., & Williams, K. A. 2012, Astrophys. J., 757, 116

Farihi, J., Wyatt, M. C., Greaves, J. S., et al. 2014, Mon. Not. R. Astron. Soc., 444, 1821

Ferri, S., Calisti, A., Mossé, C., et al. 2014, Atoms, 2, 299

Finken, K. H. & Ackermann, U. 1981, Phys. Lett. A, 85, 278

Finken, K. H. & Ackermann, U. 1982, J. Phys. D: Appl. Phys., 15, 615

Fontaine, G., Brassard, P., & Bergeron, P. 2001, Pub. Astron. Soc. Pac., 113, 409

Fontaine, G. & Wesemael, F. 1987, in Proceedings from IAU Colloq. No. 95 (Schenectady, NY: David Press), 319–326

Foord, M. E., Heeter, R. F., van Hoof, P. A., et al. 2004, Phys. Rev. Lett., 93, 055002

Fuchs, J. T. 2017, PhD thesis, University of North Carolina at Chapel Hill

Gatewood, G. D. & Gatewood, C. V. 1978, Astrophys. J., 225, 191

Gauthier, J.-C., Geindre, G.-P., Goldbach, C., Grandjouan, N., & Mazure, A. 1981, J. Phys. B: At. Mol. Phys., 14, 2099

Gianninas, A., Bergeron, P., & Ruiz, M. T. 2011, Astrophys. J., 743, 138

Gianninas, A., Curd, B., Thorstensen, J. R., et al. 2015, Mon. Not. R. Astron. Soc., 449, 3966

Gigosos, M. A. & Cardeñoso, V. 1996, J. Phys. B: At. Mol. Opt. Phys., 29, 4795

Gigosos, M. A., Djurović, S., Savić, I., et al. 2014, Astron. Astrophys., 561, A135

Gigosos, M. A., González, M. Á., & Cardeñoso, V. 2003, Spectrochim. Acta, 58, 1489

Glenzer, S., Uzelac, N. I., & Kunze, H.-J. 1992, Phys. Rev. A, 45, 8795

Gomez, T. A., Montgomery, M. H., Nagayama, T., Kilcrease, D. P., & Winget, D. E. 2017, in 20th European Workshop on White Dwarfs, Vol. 509, eprint: arXiv:1610.02342, 143

Gomez, T. A., Nagayama, T., Kilcrease, D. P., Montgomery, M. H., & Winget, D. E. 2016, Phys. Rev. A, 94, 022501

Green, M. J., Hermes, J. J., Marsh, T. R., et al. 2018, Mon. Not. R. Astron. Soc., 477, 5646

Green, R. F., Schmidt, M., & Liebert, J. 1986, Astrophys. J., Suppl. Ser., 61, 305

Greenstein, J. L. & Trimble, V. L. 1967, Astrophys. J., 149, 283

Griem, H. R. 1974, Spectral line broadening by plasmas (New York, NY: Academic Press, Inc.)

Griem, H. R., Baranger, M., Kolb, A. C., & Oertel, G. 1962, Phys. Rev., 125, 177

Habing, H. 1996, The Astron. Astrophys. Rev., 7, 97

Halenka, J., Olchawa, W., Madej, J., & Grabowski, B. 2015, Astrophys. J., 808, 131

Hansen, B. M. S. & Liebert, J. 2003, Annu. Rev. Astron. Astr., 41, 465

Harris, H. C., Munn, J. A., Kilic, M., et al. 2006, Astron. J., 131, 571

Heading, D. J., Marangos, J. P., & Burgess, D. D. 1992, J. Phys. B: At. Mol. Phys., 25, 4745

Heintz, W. D. 1974, Astron. J., 79, 819

Herwig, F. 2005, Annual Review of Astronomy and Astrophysics, 43, 435

Herwig, F., Blöcker, T., Langer, N., & Driebe, T. 1999, Astron. Astrophys., 349, L5

Holberg, J. B. 2009, in Journal of Physics: Conference Series, Vol. 172 (Barcelona, Spain: IOPscience), 012022

Hoyle, F. 1954, Astrophys. J., Suppl. Ser., 1, 121

Hu, Q., Wu, C., & Wu, X.-B. 2007, Astron. Astrophys., 466, 627

Hubeny, I. & Lanz, T. 1995, Astrophys. J., 439, 875

Hubeny, I. & Mihalas, D. 2014, Theory of Stellar Atmospheres (Princeton University Press)

Hügelmeyer, S. D., Dreizler, S., Homeier, D., et al. 2006, Astron. Astrophys., 454, 617

Iben, Jr., I. 1967, Annu. Rev. Astron. Astr., 5, 571

Iben, Jr., I., Kaler, J. B., Truran, J. W., & Renzini, A. 1983, Astrophys. J., 264, 605

Iben, Jr., I. & Renzini, A. 1983, Annu. Rev. Astron. Astr., 21, 271

Jones, M. C., Ampleford, D. J., Cuneo, M. E., et al. 2014, Rev. Sci. Instrum., 85, 083501

Kaplan, D. L., Boyles, J., Dunlap, B. H., et al. 2014, Astrophys. J., 789, 119

Kawaler, S. D. & Bradley, P. A. 1994, Astrophys. J., 427, 415

Kepler, S. O., Kleinman, S. J., Nitta, A., et al. 2007, in 15th European Workshop on White Dwarfs, Vol. 372, 35

Kepler, S. O., Pelisoli, I., Koester, D., et al. 2015, Mon. Not. R. Astron. Soc., 446, 4078

Kepler, S. O., Pelisoli, I., Koester, D., et al. 2016, Mon. Not. Roy. Astr. Soc., 455, 3413

Kerr, F. J. & Lynden-Bell, D. 1986, Mon. Not. R. Astron. Soc., 221, 1023

Kilic, M., Munn, J. A., Harris, H. C., et al. 2017, Astrophys. J., 837, 162, arXiv: 1702.06984

Kleinman, S. J., Kepler, S. O., Koester, D., et al. 2013, Astrophys. J., Suppl. Ser., 204, 5

Kobilarov, R., Konjević, N., & Popović, M. V. 1989, Phys. Rev. A, 40, 3871

Koester, D. 1987, Astrophys. J., 322, 852

Koester, D. 2010, Mem. Soc. Astron. It., 81, 921

Koester, D. & Kepler, S. O. 2015, Astron. Astrophys., 583, A86

Koester, D., Napiwotzki, R., Christlieb, N., et al. 2001, Astron. Astrophys., 378, 556

Koester, D., Provencal, J., & Gänsicke, B. T. 2014, Astron. Astrophys., 568, A118

Koester, D., Schulz, H., & Wegner, G. 1981, Astron. Astrophys., 102, 331

Kunze, H.-J. 2009, Introduction to Plasma Spectroscopy, Springer Series on Atomic, Optical, and Plasma Physics (Berlin Heidelberg: Springer-Verlag)

Lemke, M. 1997, Astron. Astrophys. Suppl. Ser., 122, 285

Liebert, J. 1980, Annu. Rev. Astron. Astr., 18, 363

Liebert, J., Bergeron, P., & Holberg, J. B. 2005, Astron. Astrophys. Suppl. Ser., 156, 47

Liebert, J., Fontaine, G., & Wesemael, F. 1987, Mem. Soc. Astron. It., 58, 17

Limoges, M.-M. & Bergeron, P. 2010, Astrophys. J., 714, 1037

Lin, C. Y. & Ho, Y. K. 2010, Phys. Plasmas, 17, 093302

Lodders, K. 2003, Astrophys. J., 591, 1220

Lyons, P. B. & Looney, L. D. 1993, in Optical Materials Reliability and Testing: Benign and Adverse Environments, Vol. 1791 (International Society for Optics and Photonics), 286–297

MacFarlane, J., Golovkin, I., Woodruff, P., & Wang, P. 2003, in APS Division of Atomic, Molecular and Optical Physics Meeting Abstracts, Boulder, Colorado, J1.181

MacFarlane, J. J. 2003, J. Quant. Spectrosc. Radiat. Transf., 81, 287

MacFarlane, J. J., Golovkin, I. E., Wang, P., Woodruff, P. R., & Pereyra, N. A. 2007, High Energ. Dens. Phys., 3, 181

MacFarlane, J. J., Golovkin, I. E., & Woodruff, P. R. 2006, J. Quant. Spectrosc. Radiat. Transf., 99, 381

Madej, J., Należyty, M., & Althaus, L. G. 2004, Astron. Astrophys., 419, L5

McDaniel, D. H., Mazarakis, M. G., Bliss, D. E., et al. 2002, in Dense Z-Pinches: 5th International Conference on Dense Z-Pinches, Proceedings of a Conference held 23-28 June, 2002 in Albuquerque, New Mexico, Vol. 651 (New York, NY: AIP), 23–28

Mestel, L. 1952, Mon. Not. Roy. Astr. Soc., 112, 583

Mix, L. P. 2007, PFIDL Version 2.0, Tech. Rep. PFIDLV2.0; 001403MLTPL01, Sandia National Laboratories

Montgomery, M. H., Falcon, R. E., Rochau, G. A., et al. 2015, High Energ. Dens. Phys., 17, 168

Morton, D. C. 2000, Astrophys. J., Suppl. Ser., 130, 403

Napiwotzki, R., Christlieb, N., Drechsel, H., et al. 2001, Astron. Nachr., 322, 411

Nash, T. J., Rochau, G. A., & Bailey, J. E. 2010, Rev. Sci. Instrum., 81, 10E518

Nather, R. E., Robinson, E. L., & Stover, R. J. 1981, Astrophys. J., 244, 269

Nomoto, K., Iwamoto, K., & Kishimoto, N. 1997, Science, 276, 1378

Onofrio, R. & Wegner, G. A. 2014, Astrophys. J., 791, 125

Payne, C. H. 1925, PhD thesis, Radcliff College

Popper, D. M. 1954, Astrophys. J., 120, 316

Provencal, J. L., Shipman, H. L., Høg, E., & Thejll, P. 1998, Astrophys. J., 494, 759

Reindl, N., Rauch, T., Werner, K., et al. 2015, in 19th European Workshop on White Dwarfs, Vol. 493, Warwick, UK, 21

Richer, H. B., Fahlman, G. G., Ibata, R. A., et al. 1997, Astrophys. J., 484, 741

Rocca-Volmerange, B. & Schaeffer, R. 1990, Astron. Astrophys., 233, 427

Rochau, G. A., Bailey, J. E., Chandler, G. A., et al. 2007, Plasma Phys. Contr. F., 49, B591

Rochau, G. A., Bailey, J. E., Falcon, R. E., et al. 2014, Phy. of Plasmas, 21, 056308

Rose, D. V., Welch, D. R., Madrid, E. A., et al. 2010, Phys. Rev. Spec. Top - AC, 13, 010402

Rybicki, G. B. & Lightman, A. P. 1986, Radiative Processes in Astrophysics (Hoboken, New Jersey: Wiley)

Sahu, K. C., Anderson, J., Casertano, S., et al. 2017, Science, eaal2879

Salpeter, E. E. 1952, Astrophys. J., 115, 326

Salpeter, E. E. 1961, Astrophys. J., 134, 669

Sanford, T. W. L., Peterson, D. L., Lemke, R. W., et al. 2002, in 5th International Conference on Dense Z-Pinches, Proceedings of a Conference, Vol. 651, 269–274

Schaeuble, M., Preston, G., Sneden, C., et al. 2015, Astron. J., 149, 204

Schröder, K.-P. & Connon Smith, R. 2008, Mon. Not. R. Astron. Soc., 386, 155

Schwab, J., Quataert, E., & Kasen, D. 2016, Mon. Not. R. Astron. Soc., 463, 3461

Schwarzschild, M. 1958, Structure and Evolution of the Stars (Princeton, NJ: Princeton University Press)

Shipman, H. L., Provencal, J. L., Høg, E., & Thejll, P. 1997, Astrophys. J. Lett., 488, L43

Shu, F. H., Adams, F. C., & Lizano, S. 1987, Annu. Rev. Astron. Astr., 25, 23

Sion, E. M., Greenstein, J. L., Landstreet, J. D., et al. 1983, Astrophys. J., 269, 253

Sweeney, M. A. 1974, PhD thesis, Columbia University

Tremblay, P.-E. & Bergeron, P. 2009, Astrophys. J., 696, 1755

Tremblay, P.-E., Bergeron, P., & Gianninas, A. 2011, Astrophys. J., 730, 128

Tremblay, P.-E., Cummings, J., Kalirai, J. S., et al. 2016, Mon. Not. R. Astron. Soc., 461, 2100

Tremblay, P.-E., Kalirai, J. S., Soderblom, D. R., Cignoni, M., & Cummings, J. 2014, Astrophys. J., 791, 92

van den Bergh, S. 1991, Phys. Rep., 204, 385

van Horn, H. M. 1968, Astrophys. J., 151, 227

van Horn, H. M. 1971, in Proceedings from IAU Symposium No. 42, Vol. 42 (Dordrecht: Springer Verlag), 97

Vidal, C. R., Cooper, J., & Smith, E. W. 1970, J. Quant. Spectrosc. Radiat. Transf., 10, 1011

Vidal, C. R., Cooper, J., & Smith, E. W. 1973, Astrophys. J., Suppl. Ser., 25, 37

Voss, B., Koester, D., Napiwotzki, R., Christlieb, N., & Reimers, D. 2007, Astron. Astrophys., 470, 1079

Weidemann, V. 2000, Astron. Astrophys., 363, 647

Werner, K., Dreizler, S., Heber, U., & Rauch, T. 1996, in Proceedings of a colloquium held in Bamberg, Germany, 28 August - 1 September 1995, Vol. 96, 267

Werner, K., Heber, U., & Hunger, K. 1991, Astron. Astrophys., 244, 437

Werner, K. & Herwig, F. 2006, Pub. Astron. Soc. Pac., 118, 183

Werner, K. & Rauch, T. 2015, Astron. Astrophys., 584, A19

Whaling, W., Anderson, W. H. C., Carle, M. T., Brault, J. W., & Zarem, H. A. 1995, J. Quant. Spectrosc. Radiat. Transf., 53, 1

Wiese, W. L., Kelleher, D. E., & Paquette, D. R. 1972, Phys. Rev. A, 6, 1132

Winget, D. E., Hansen, C. J., Liebert, J., et al. 1987, Astrophys. J. Lett., 315, L77

Winget, D. E. & Kepler, S. O. 2008, Annu. Rev. Astron. Astr., 46, 157

Winget, D. E., Kepler, S. O., Campos, F., et al. 2009, Astrophys. J. Lett., 693, L6

Winget, D. E., Sullivan, D. J., Metcalfe, T. S., Kawaler, S. D., & Montgomery, M. H. 2004, Astrophys. J., 602, L109

Wood, P. R., Olivier, E. A., & Kawaler, S. D. 2004, Astrophys. J., 604, 800

Zuckerman, B. & Becklin, E. E. 1987, Nature, 330, 138

Zuckerman, B., Koester, D., Melis, C., Hansen, B. M., & Jura, M. 2007, ApJ, 671, 872